UCL Université catholique de Louvain

École polytechnique de Louvain (EPL)

epl

Magnetotransport properties of interconnected magnetic nanowires and multilayers

Dissertation presented by
Simen O. SOPP

for obtaining the Master's degree in
Chemical and Materials Engineering

Supervisor(s)
Prof. Luc PIRAUX

Reader(s)
Prof. Benoit HACKENS, Tristan DA CÂMARA GOMES

Academic year 2016-2017

Abstract

This Master's thesis investigates the magnetic and magnetotransport properties of novel three-dimensional interconnected multilayered nanowire networks of NiCoCu/Cu. Very high giant magnetoresistance (GMR) of 40% at room temperature and 80% at 20 K, has been measured, in the current-perpendicular-to-plane (CPP) geometry.

Track-etched polycarbonate membranes with interconnected pore network, were used for "bottom-up" template-assisted electrodeposition of samples from single electrolyte baths. The synthesis parameters have been systematically optimised in order to yield samples with high CPP-GMR. Extensive investigations of changing parameters, such as the Cu^{2+} electrolyte concentration, and nanowire packing density, have been carried out.

Results show that electrodeposited interconnected multilayered nanowire networks of NiCoCu/Cu are good candidates for studying CPP-GMR properties. The GMR effect seems to be somewhat affected by the Cu^{2+} electrolyte concentration, and significantly enhanced upon reduction of the nanowire packing density. The reduced amount of crossing zones in the nanowire network might be the cause of this enhancement. However, the samples with low nanowire packing density suffers from mechanical instability, which creates several experimental challenges and poor reproducibility. If these challenges become sorted out, these interconnected multilayered nanowire networks with low packing density will emerge as excellent candidates for CPP-GMR research.

Keywords: Giant magnetoresistance, ferromagnetism, multilayers, nanowires, three-dimensional nanostructures.

Acknowledgements

I would like to thank my supervisor Prof. Luc Piraux of the EPL/BSMA at Université catholique de Louvain, for guidance and support during this Master's thesis. Prof. Piraux's office was always open in case I needed advice. He gave consistent guidelines for me to follow, but also let me contribute with my own ideas to form my work. I am also very grateful for the unconditional support he has provided me in my pursuit of my further career.

I am immensely grateful to Tristan da Câmara Gomes of the EPL/BSMA at Université catholique de Louvain, for instructions and cooperation on this project. His knowledge, thorough feedback on my work, and willingness to help me in all aspects along the way have been indispensable. The quality of this Master's thesis would not have been the same without him.

Furthermore, I would like to thank Flavio Abreu Araujo and Joaquin De La Torre Medina for assistance and valuable discussions, Valentin Matton and Pierre-Olivier Colard for being nice Master's student colleagues, and everyone else at BSMA who have assisted me, and made me feel welcome.

Thanks to the FAME Master Program and partner universities, that have given me two very exciting years of studying abroad. I am especially grateful to Universität Augsburg and Université catholique de Louvain for giving me education of very high quality.

I would direct a warm thanks to my dear little sister, Nora, for sharing her valuable time and graphical design skills. She assisted me with some magnificent figures which enhanced the quality of this Master's thesis. Finally, I express my profound gratitude to my family who have been constantly supporting and motivating during these last two years. This accomplishment would not have been possible without you. Thank you.

Contents

List of Symbols

$\uparrow$	Majority spin carrier
$\downarrow$	Minority spin carrier
$^\circ$	Degree
$\%$	Percent
$\#$	"Number of"
$\bullet$	Scalar product operator
$\times$	Multiplication operator
$\parallel$	Parallel
$\perp$	Perpendicular
$\sim$	"More or less"
$\approx$	"Approximately
$\propto$	"Proportional to"
$\pm$	Plus/minus
$<$	"Less than"
$>$	"Greater than"
$\leq$	"Less or equal to"
$\geq$	"Greater or equal to"
α	Spin asymmetry coefficient
β	Bulk spin asymmetry coefficient
γ	Interface spin asymmetry coefficient
Δ	Difference operator
ϵ_m	Magnetostatic self-energy
ϵ_q	Magnon energy
λ	Electron mean free path
λ_e	Electron wavelength
λ_s	Localised electron mean free path
ν	Constant related to crystal structure
σ	Conductivity
$\sigma_\uparrow$	Conductivity of majority spin current channel
$\sigma_\downarrow$	Conductivity of minority spin current channel
σ_s	Conductivity of spin s
σ_{so}	Spin-orbit cross section
η	Reaction efficiency
θ	Angle between nanowires and out-of-plane axis
θ	Angle between magnetisation and easy axis
τ	Average scattering time
φ	Angle between current density and magnetisation
ϕ_i, ϕ_j	Angles between neighbouring ferromagnetic layers
ρ	Resistivity
$\rho_\perp$	Resistivity when applied field perpendicular to current
$\rho_\parallel$	Resistivity when applied field parallel to current

$\rho_\uparrow$	Resistivity in majority spin current channel
$\rho_\downarrow$	Resistivity in minority spin current channel
ρ_{avg}	Average resistivity
ρ_F	Normal resistivity in ferromagnetic layer
ρ_N	Normal resistivity in nonmagnetic layer
μ	Mobility of electron
μ	Electric potential
μ_0	Vacuum permeability
μ_B	Bohr magneton
μ_s	Electrochemical potential for spin s
χ_P	Pauli susceptibility
ω_q	Magnon angular frequency
Ω	Ohm
a	Horisontal axis of ellipsoid of revolution
a	Activity
A	Available cathode surface area
$\mathbf{B}$	Magnetic flux density vector
B	Magnetic flux density
c	Vertical axis of ellipsoid of revolution
c	Material-dependent constant
C	Dipole-dipole interaction constant
d	Diameter
$\mathcal{D}(E)$	Density of states
$\mathcal{D}_{\uparrow,\downarrow}(E)$	Spin-split density of states
D_{sw}	Spin-wave stiffness parameter
e	Elementary charge
e^-	Electron
E	Energy of an electron
E^0	Normal electrode potential
E_a	Anisotropy energy
E^{dep}	Deposition potential
E_{dip}	Total dipole-dipole energy
E^{eq}	Equilibrium potential
E_F	Fermi energy
$E(k_s)$	Elliptical integral
F	Faraday constant
GMR_{IP}	In-plane giant magnetoresistance
GMR_{OOP}	Out-of-plane giant magnetoresistance
$\hbar$	Reduced Planck constant
$\mathbf{H}$	Magnetic field strength vector
H	Magnetic field strength
H_d	Demagnetising field
H_{eff}	Effective demagnetising field
H_{eff}^{NiCoCu}	Effective demagnetising field of NiCoCu layer
H_{eff}^{int}	Effective internal demagnetising field
H_{ext}	External magnetic field
H_{max}	Maximum applied field
H_n	Demagnetising field experienced by layer n
H_{sat}	Saturation field
$\mathbf{I}$	Current vector
I	Current

$\mathcal{I}$	Stoner exchange parameter
k	Integer
k	Wave number
k_s	Modulus
k_B	Boltzmann constant
K_1	Anisotropy constant
$K(k_s)$	Elliptical integral
K_{MC}	Magnetocrystalline anisotropy constant
$\mathbf{j}$	Current density
j	Integer
$\mathcal{J}$	Exchange constant
l	Spacer layer
l_{sf}^{F}	Spin diffusion length in the ferromagnetic layer
l_{sf}^{N}	Spin diffusion length in the nonmagnetic layer
$\mathbf{L}$	Total orbital angular momentum
L_x	Orbital angular momentum in x-direction
L_y	Orbital angular momentum in y-direction
L_z	Orbital angular momentum in z-direction
$L^{+(-)}$	Orbital angular momentum raising (lowering) operator
L	Total multilayer length
m	Integer
m	Mass
m^*	Effective mass of electron
m_ℓ	Magnetic quantum number
m	Magnetic moment
$\langle m \rangle$	Average magnetic moment
$\mathbf{M}$	Magnetisation vector
M	Number of bilayers
M	Metal atom
M_c	Critical number of bilayers
M_{sat}	Saturation magnetisation
M_M	Molarity of metal atoms
M^{n+}	Metal ion with charge $n+$
n	Spin state of electron
n	Number of ferromagnetic layers
n	Number density of electrons
n	Number of electrons
n_{bl}	Number of bilayers
$\mathcal{N}_{\uparrow,\downarrow}(E)$	Density of states per electron per spin
$\mathcal{N}_{ij}$	Demagnetising tensor
$\mathcal{N}_a$	Demagnetising factor in a-direction of ellipsoid
$\mathcal{N}_c$	Demagnetising factor in c-direction of ellipsoid
$\mathcal{N}_{\parallel}^{cyl}$	Demagnetising factor parallel to cylinder plane
$\mathcal{N}_{\perp}^{cyl}$	Demagnetising factor perpendicular to cylinder plane
p	Fraction of antiparallel layer arrangement
P	Porosity factor
q	Magnon wave vector
Q_M	Total charge of deposition of metal M
r	Aspect ratio t/d
r_0	Resistance of F layer in series with N layer
r_b	Normal interface resistance

r_F	Aspect ratio t_F/d
r_F	Deposition rate of F layer
r_N	Aspect ratio t_N/d
r_N	Deposition rate of N layer
$r_\uparrow$	Resistance of majority spins
$r_\downarrow$	Resistance of minority spins
$r_{+(-)}$	Resistance of spin-channel for electron with $+(-)$ spin value
$r^{(P,AP)}$	Resistance in parallel (antiparallel) layer arrangement
r_{SI}	Spin-coupled interface resistance
R	Ideal gas constant
$R_\parallel$	Resistance for applied field parallel to nanowire axis
$R_\perp$	Resistance for applied field perpendicular to nanowire axis
R_{AP}	Resistance in antiparallel magnetic layer arrangement
R_P	Resistance in parallel magnetic layer arrangement
R_{int}	Internal resistance of the measurement circuit
R_{max}	Maximum resistance
R_{min}	Minimum resistance
$R^{IP}_{max(min)}$	Maximum (minimum) resistance when field applied in-plane
R^{IP}	Resistance when field applied in-plane
R^{OOP}	Resistance when field applied out-of-plane
R_{sample}	Resistance of the sample
$R(H)$	Resistance as a function of applied field
$R(T)$	Resistance as a function of temperature
s	Separation layer
s	Spin state
$\mathbf{S}$	Total spin angular momentum
S_x	Spin angular momentum in x-direction
S_y	Spin angular momentum in y-direction
S_z	Spin angular momentum in z-direction
$S^{+(-)}$	Spin angular momentum raising (lowering) operator
t	Layer thickness when $t_F = t_N$
t	Time
t_{bl}	Bilayer thickness
t_F	Thickness of ferromagnetic layer
t_N	Thickness of nonmagnetic layer
t_{tot}	Total electrodeposition time
t_{NiCoCu}	Thickness of NiCoCu layer
t_{Cu}	Thickness of Cu layer
T	Temperature
T_F	Time of NiCoCu deposition pulse
T_N	Time of Cu deposition pulse
T_{of}	Time of overfilling
V	Volume
V_F	Deposition potential for NiCoCu layer
$V_{lock-in}$	Lock-in potential
V_{meas}	Measured potential
V_N	Deposition potential for Cu layer
ΔV_I	Interface potential drop
x	Composition constant
X	Atomic number
Z	Number of valence electrons

List of Acronyms

μm	Micrometer
aq	Aqueous
A	Ampere
AC	Alternating current
Ag	Silver
AGFM	Alternating gradient force magnetometer
AMR	Anisotropic magnetoresistance
AP	Antiparallel
Ar	Argon
cm	Centimeter
cos	Cosine function
C	Coulomb
CGS	The centimetre–gram–second system of units
CIP	Current-in-plane
Cl	Chlorine
Co	Cobalt
$CoSO_4 \cdot 7H_2O$	Nickel(II) sulfate heptahydrate
CPP	Current-perpendicular-to-plane
Cr	Chromium
Cu	Copper
Cu^{2+}	Copper(II) ion
$CuSO_4 \cdot 5H_2O$	Copper(II) sulfate pentahydrate
emu	Electromagnetic unit
etc.	et cetera
eV	Electron volt
exp	Exponential function
EDX	Energy-dispersive X-ray spectroscope
fcc	Face-centered cubic
F	Ferromagnetic
Fe	Iron
FE-SEM	Field emission scanning electron microscope
Gs	Gauss
GMR	Giant magnetoresistance
hcp	Hexagonal closest packing
H_2SO_4	Sulfuric acid
H_3BO_3	Boric acid
He	Helium
Hz	Hertz
IP	In-plane
k	Kilo, 1000
ln	Natural logarithm

L	Liter
m	Meter
m	Milli
mm	Millimeter
mM	Millimole per liter
ms	Millisecond
M	Mole per liter
MC	Magnetocrystalline
MR	Magnetoresistance
n	Nano
N	Nonmagnetic
NaOH	Sodium hydroxide
Ni	Nickel
Ni^{2+}	Nickel(II) ion
NiCoCu	Alloy of nickel, cobalt and copper
$NiSO_4 \cdot 6H_2O$	Nickel(II) sulfate hexahydrate
nm	Nanometer
NW	Nanowire
Oe	Oersted
OOP	Out-of-plane
pH	Potential of hydrogen
psi	Pound per square inch
P	Parallel
PC	Polycarbonate
PID	Proportional–integral–derivative
Pt	Platinum
RT	Room temperature
Ru	Ruthenium
s	Second
sscm	Standard cubic centimeter per minute
Si	Silicon
SDL	Spin diffusion length
SEM	Scanning electron microscope
SI	The International System of Units
TEM	Transmission electron microscope
TL	Trilayer
UCL	Université catholique de Louvain
V	Volt
VF	Valet-Fert (model)
W	Watt
Å	Ångström

List of Figures

List of Tables

Introduction

The work contained in this in this Master's thesis lies in the field of nanoscience; more specifically magnetism in complex three-dimensional networks of nanowires. Magnetic nanowires exhibits very interesting magnetic properties, attributed to their reduced dimensionality. Combined with relatively cheap, easy and reliable fabrication methods, this makes magnetic nanowires very interesting for future technology, especially in the field of spintronics.

Magnetic nanowires can be fabricated by electrochemical deposition into templates [1]. Commercially available high-quality track-etched polycarbonate (PC) offers a well-established method of controlled "bottom-up" synthesis of nanowires and multilayers, from metal ion containing electrolyte baths. The nanowires are shaped by the pores in the PC membrane, which have been selectively etched to give them well-defined cylindrical shapes and uniform diameters, ranging from a few tens of nanometers up to a few micrometers. This method has has been used for decades by the group lead by Prof. Luc Piraux, who is a pioneer and an authority in the field [1], at Université catholique de Louvain (UCL), where the work of this Master's thesis has been carried out, to fabricate parallel arrays of magnetic nanowires. Recently, track-etched PC membranes with networks of crossed cylindrical pores have become available, opening the possibilities for novel three-dimensional networks if interconnected magnetic nanowires [2, 3, 4]. Their unique architecture and high nanowire connectivity make these networks attractive for nanodevice components. The latter is due to the Many studies make use of porous alumina templates to fabricate arrays of parallel nanowires. However, it has still not been found possible to fabricate alumina templates with crossed pore network, and in this sense the PC templates are unique.

Since its discovery in 1988 [5, 6], giant magnetoresistance (GMR), in alternating layers of ferromagnetic (F) and nonmagnetic (N) metals, has been extensively studied and used as read-head components in hard drives since 1994 [7]. The discovery was made in multilayers of Fe/Cr thin films with antiferromagnetic coupling. It was observed a large change in the electrical resistance when the multilayers were subjected to a strong magnetic field. The current was conducted along the plane of the thin films; the so-called current-in-plane (CIP) geometry. However the GMR effect was expected to be higher when measured in the current-perpendicular-to-plane (CPP) geometry. The resistance in CPP geometry measurements of multilayered thin films is usually so low that it cannot be separated from the contact resistance. In 1991 it was, however, succeeded to measure the CPP-GMR in multilayered thin films by using advanced experimental techniques, including superconducting contacts at low temperatures, to reduce the contact resistance [8]. The CPP-GMR was shown to be higher than CIP-GMR, but further research was limited by the experimental challenges.

However, magnetic nanowires are excellent candidates for studying the CPP-GMR, because of the possibility of growing multilayers into templates, as mentioned above. By electrodeposition arrays of multilayered nanowires with several hundreds of layers can easily be fabricated, resulting in samples with resistance of the order of tens or hundreds of Ohm. With the high resistance, the contact resistance becomes negligible. Thus, multilayered nanowires are suitable for studying

CPP-GMR even at room temperatures [9].

For this thesis, original experimental studies on the novel system of interconnected multilayered nanowire networks have been performed, to study its CPP-GMR properties. An interesting feature of this nanoscale system is that the length of the multilayers are not limited to the thickness of the sample, which constitutes a significant difference compared to the system of parallel multilayered nanowire arrays. Additionally, the interconnected network simplifies the transport measurement technique. A major part of the work has been related to the synthesis process of the samples by electrodeposition in the PC templates. The multilayers were made of ferromagnetic layers of Ni, Co and Cu, based on earlier studies on parallel multilayered nanowire arrays [10]. Initially an extensive amount of work was required to decide the optimal synthesis parameters, which were used for the fabrication of all the samples studied. The other major part has been related to the measurements and characterisation of the samples. Magnetotransport measurements have been carried out to investigate the CPP-GMR at room temperature and down to 12 K. Moreover, the magnetic properties have been investigated at room temperature, along with morphology and elemental composition measurements. The multilayered samples have been compared with continuous samples prepared with similar synthesis parameters, to be able to relate the obtained results to existing studies.

This thesis is written in three major chapters. Chapter one explains the state of the art and provide the reader with the necessary theoretical knowledge, required to understand the subsequent chapters, and to establish a foundation for the discussion and interpretation of the results. The second chapter contains the detailed description of the experimental work which was performed for the thesis. The third chapter provides the discussion, interpretation and conclusion of the results from the experimental work. Finally, the outcome of this extensive investigation of CPP-GMR in interconnected multilayered nanowire networks will be summarised, and some perspectives for future studies on the subject will be outlined.

Chapter 1

State of the art

1.1 Magnetic properties of ferromagnetic nanowires

To understand the mechanisms leading to the giant magnetoresistance in nanowires, a reminder on some fundamental aspects regarding the properties of ferromagnets are necessary. Ferromagnets exhibit spontaneous magnetisation that shifts the energy bands, resulting in the possibility of *spin-dependent scattering*, which is the foundation of spintronics. The preferred direction of magnetisation in a ferromagnet is governed by the magnetic anisotropy, which is related to its shape and microstructure. Magnets constitutes dipoles which can interact with other dipoles, and these interactions are governed by *magnetostatic energy*.

1.1.1 Ferromagnetism

The discussion of ferromagnetism in metals starts from the band paramagnetism [11]. Delocalised electrons obey Fermi-Dirac statistics, and thus only a small fraction of the electrons with energy close to the Fermi energy, E_F, are able to respond to a change in magnetic field or temperature. From this the Pauli susceptibility can be derived as a small, positive quantity, which is almost independent of the temperature. In the three-dimensional free-electron model, the density of states $\mathcal{D}(E)$ is proportional to $\sqrt{E}$, where E is the energy of the free-electron. Because the electrons have spin of opposite directions, their energy changes in opposite directions in response to an external magnetic field H. This causes an energy shift in the $\uparrow$ and $\downarrow$ electron bands, corresponding to $\mp\mu_0 H\mu_B$, where μ_0 is the vacuum permeability and μ_B is the Bohr magneton which expresses the magnetic moment of one electron. This energy shift is shown in Figure 1.1a. To compensate for the energy shift, electrons from the $\downarrow$ band close to E_F can spin-flip into the $\uparrow$ band. This results in a net magnetic moment, called paramagnetism. The resulting Pauli paramagnetic susceptibility can be written

$$\chi_P = \mu_o \mu_B^2 \mathcal{D}(E_F). \tag{1.1}$$

$\mathcal{D}(E_F)$ is double the density of states for each spin $\mathcal{D}_{\uparrow,\downarrow}(E_F)$. When the density of states becomes high enough, it becomes energetically favourable for the bands to split, and the metal thus becomes spontaneously ferromagnetic [11]. It can be shown that this happens when the susceptibility diverges spontaneously. This can be described through the *Stoner criterion*:

$$\mathcal{I}\mathcal{N}_{\uparrow,\downarrow}(E_F) > 1, \tag{1.2}$$

where $\mathcal{I}$ is the Stoner exchange parameter, which is roughly 1 eV for $3d$ ferromagnets, and $\mathcal{N}_{\uparrow,\downarrow}(E) = \mathcal{D}(E)/2n$, which means the density of states per atom for each spin state.

Fe, Co and Ni are the only elements that reaches the Stoner criterion as the have narrow bands and a peak in $\mathcal{N}(E)$ near E_F [11]. For Co and Ni are considered as strong ferromagnets

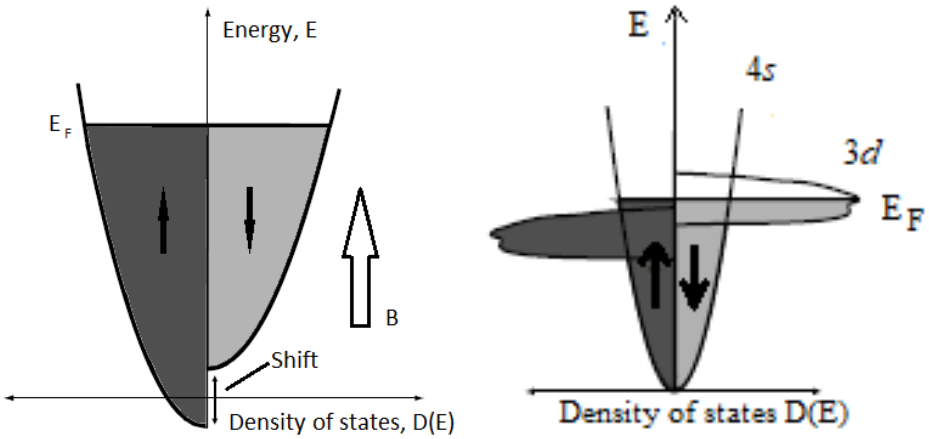

(a) (b)

Figure 1.1: Energy shift of (a) the ↑ and ↓ s bands of a metal in a magnetic field B, and (b) the $3d$ subbands in a strong ferromagnet. Adapted from [11], page 82 and 147 respectively.

because the band splitting is strong enough to shift the $3d$ ↑ subband completely below E_F, while the $3d$ ↓ band is only partly filled. This is shown in Figure 1.1b. The ↑ band is defined as the majority band, and the ↓ band the minority, and the total magnetic moment in the metal is dominated by the ↑ band. The calculated spin-split density of states, $\mathcal{N}_{\uparrow,\downarrow}(E)$, is shown in Figure 1.2. The different filling of the bands leads to different Fermi surfaces for ↑ and ↓ electrons.

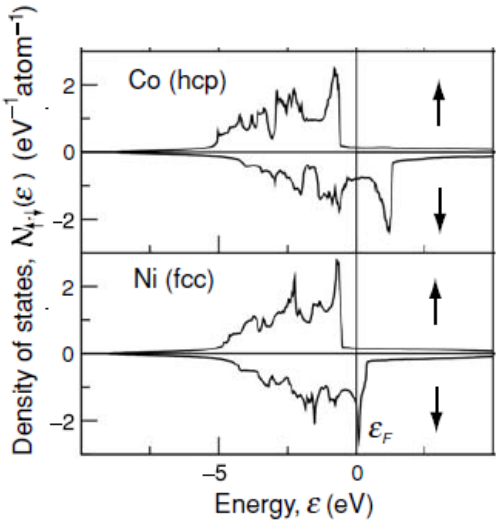

Figure 1.2: Spin-split density of states for Co and Ni, adapted from [11], page 149.

1.1.2 Demagnetising field

The following discussion requires a brief repetition of the basic magnetic quantities. The dipole moment m is the elementary magnetic quantity, and its mesoscopic volume average is the magnetisation $\mathbf{M}$. $\mathbf{B}$ is the magnetic flux density and $\mathbf{H}$ is the magnetic field strength. They are related through the vacuum permeability μ_0 by

$$\mathbf{B} = \mu_0(\mathbf{H} + \mathbf{M}), \tag{1.3}$$

Table 1.1: Conversion scheme for the magnetic quantities **H**, **B** and **M**, according to the SI and CGS systems.

Quantity	SI system	CGS system	Conversion
H	A m^{-1}	Oersted (Oe)	1 Oe = $\frac{10^3}{4\pi}$ A m^{-1}
B	Tesla	Gauss (Gs)	1 Gs = 10^{-4} Tesla
M	A m^{-1}	emu cm^{-3}	1 emu cm^{-3} = 10^3 A m^{-1}

in the SI system, and equivalently by

$$\mathbf{B} = \mathbf{H} + 4\pi\mathbf{M}, \tag{1.4}$$

in the CGS system [11]. The relationship between the basic magnetic quantities is reported in Table 1.1.

In a uniformly magnetised sample there exists a demagnetising field, $\mathbf{H}_d$, which is related to **M** through

$$H_{di} = -\mathcal{N}_{ij} M_j \qquad i,\ j = x,\ y,\ z. \tag{1.5}$$

$\mathcal{N}_{ij}$ is the demagnetising tensor, which is generally represented by a symmetric 3×3 matrix [11]. In an ellipsoid of revolution, shown in Figure 1.3, $\mathbf{H}_d$ and **M** are collinear along the principal directions, and the diagonal components of $\mathcal{N}$ ($\mathcal{N}_x$, $\mathcal{N}_y$, $\mathcal{N}_z$) are known as the demagnetising factors. They are restricted by the condition,

$$\mathcal{N}_x + \mathcal{N}_y + \mathcal{N}_z = 1, \tag{1.6}$$

which means that only two of the three components are independent.

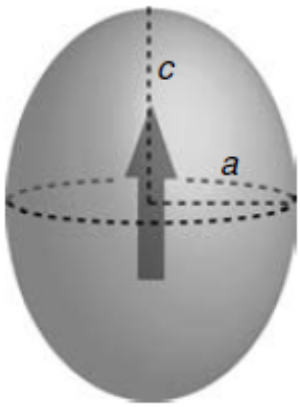

Figure 1.3: Ellipsoid of revolution with $c > a$ and magnetisation along the c easy axis. Copied from [11]

The demagnetising factor, $\mathcal{N}_c$, of an ellipsoid of revolution with major axes (a,a,c) with $r = c/a > 1$ and $r = c/a < 1$ are exactly calculated by,

$$\mathcal{N}_c = \frac{1}{(r^2-1)}\left[\frac{r}{\sqrt{r^2-1}}\cosh^{-1}(r) - 1\right], \tag{1.7}$$

$$\mathcal{N}_c = \frac{1}{(1-r^2)}\left[1 - \frac{r}{\sqrt{r^2-1}}\cos^{-1}(r)\right], \tag{1.8}$$

respectively. The relationship between $\mathcal{N}_c$ and $\mathcal{N}_a$ is shown in Table 1.2. It is common to use

Table 1.2: Some demagnetising factors for some simple shapes. Adapted from [11].

Shape	**Magnetisation direction**	$\mathcal{N}$
Long needle	Parallel to axis	0
	Perpendicular to axis	1/2
Thin film	Parallel to plane	0
	Perpendicular to plane	1
Sphere	Any direction	1/3
General ellipsoid of revolution	$\mathcal{N}_c = (1 - 2\mathcal{N}_a)$	

demagnetising factors to obtain an approximation of the internal field, even in samples of other shapes, such as cylinders, even though the demagnetising field is not completely uniform.

For an isolated magnetic cylinder with uniform magnetisation the magnetometric demagnetising factor can be written

$$\mathcal{N} = 1 - \frac{4}{3\pi r}\left[\sqrt{1+r^2}\left[r^2 K(k_s) + (1-r^2)E(k_s)\right] - 1\right], \tag{1.9}$$

where $K(k_s)$ and $E(k_s)$ are elliptical integrals with modulus $k_s = 1/\sqrt{1+r^2}$, and $r = t_F/d$ [12]. Then, the demagnetising factor parallel to the c axis of the cylinder $\mathcal{N}_{\parallel}^{cyl}$ can be defined as the ratio of the average demagnetising field and the average magnetisation of the entire sample [13]. Then the demagnetising factor in the a direction, $\mathcal{N}_{\perp}^{cyl}$, can be found through the relation

$$2\mathcal{N}_{\perp}^{cyl} + \mathcal{N}_{\parallel}^{cyl} = 1. \tag{1.10}$$

The consequences of this result will be discussed below in Section 1.1.3 and 1.1.4.

1.1.3 Magnetic anisotropy

The natural direction of magnetisation in ferromagnetic domains preferentially lie along one or more easy axes [11]. This tendency is represented by the magnetic anisotropy energy. In general, the anisotropy energy E_a can be expressed by the angle between the magnetisation direction and the easy axis θ and the anisotropy constant K_1 through

$$E_a = K_1 \sin^2\theta. \tag{1.11}$$

There are three main sources of anisotropy, which are related to sample shape, crystal structure and atomic or micro-scale structure.

For nanowire networks, the effective anisotropy energy is governed by a competition between shape and magnetocrystalline (MC) anisotropy, together with the magnetostatic dipolar interactions between different nanowires. In multilayered nanowires, additional dipolar interactions among the individual magnetic layers must be taken into account [14]. Typically, this can favour a preferential direction of magnetisation either along the nanowire longitudinal axis, or perpendicular to it [15, 16]. Anisotropy influences the magnetotransport properties of magnetic nanowires and interconnected magnetic nanowire networks [3, 2].

Shape anisotropy

Shape anisotropy derives from the demagnetising field [11]. It is effective in solids with single domains, as multiple domains create own demagnetising fields and are subject of the stray fields

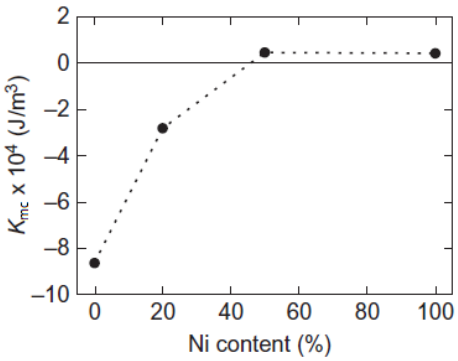

Figure 1.4: Fitted MC anisotropy constant as a function of Ni concentration. Copied from [14], p. 60.

of other domains. The magnetostatic energy of a ferromagnetic ellipsoid, like the one shown in Figure 1.3, with magnetisation M_s is,

$$\epsilon_m = \frac{1}{2}\mu_0 V \mathcal{N} M_s^2, \tag{1.12}$$

where V is the ellipsoid volume, and M_s is the saturation magnetisation. Equation 1.12 shows that the magnetostatic energy decrease with decreasing $\mathcal{N}$, thus implying that the easy axis of magnetisation lies parallel to the direction of the lowest value of $\mathcal{N}$, and the hard axis lies along the direction of the highest value of $\mathcal{N}$.

For an isolated cylinder with uniform magnetisation, the effective demagnetising field H_{eff} which can be written as a function of M_s and $\mathcal{N}_{\parallel}^{cyl}$ through Equation 1.10 as [17]:

$$H_{eff}^{cyl} = 4\pi M_s(\mathcal{N}_{\perp}^{cyl} - \mathcal{N}_{\parallel}^{cyl}) = 2\pi M_s(1 - 3\mathcal{N}_{\parallel}^{cyl}). \tag{1.13}$$

Magnetocrystalline anisotropy

MC anisotropy in Ni-Co nanowires is an interesting case, as it is greatly influenced by the alloy composition [15, 16]. It has been shown that the MC anisotropy almost vanishes in Ni-Co nanowires when the Ni concentration is higher than ∼50% [14]. This change is accompanied with the crossover from hcp (Co) to fcc (Ni) crystal structure. Figure 1.4 shows the MC anisotropy constant K_{mc} as a function of the relative Ni concentration of the Ni-Co alloy, showing how K_{mc} almost vanishes at high Ni concentrations. Furthermore, electrodeposition of cubic Ni-Co has a tendency to obtain polycrystalline layers where the remaining MC anisotropy can point in different directions. Thus the MC anisotropy in the Ni-Co systems relevant for this work can be neglected.

1.1.4 Magnetostatic interactions in nanowires

In a continuous Ni-rich Ni-Co nanowire shape anisotropy causes a single magnetic domain with magnetisation along the longitudinal wire axis. This nanowire will exhibit square-like magnetisation hysteresis loops. In multilayered nanowires, however, the layers can be considered as cylinders with a aspect ratio relating the height and diameter of the layer. The ferromagnetic layers can be considered as single magnetic domains, as long as the diameter is sufficiently low, so the anisotropy energy is dominated by shape anisotropy. In this case, each layer constitutes a magnetic dipole which can interact with the other dipoles in neighbouring layers, and in

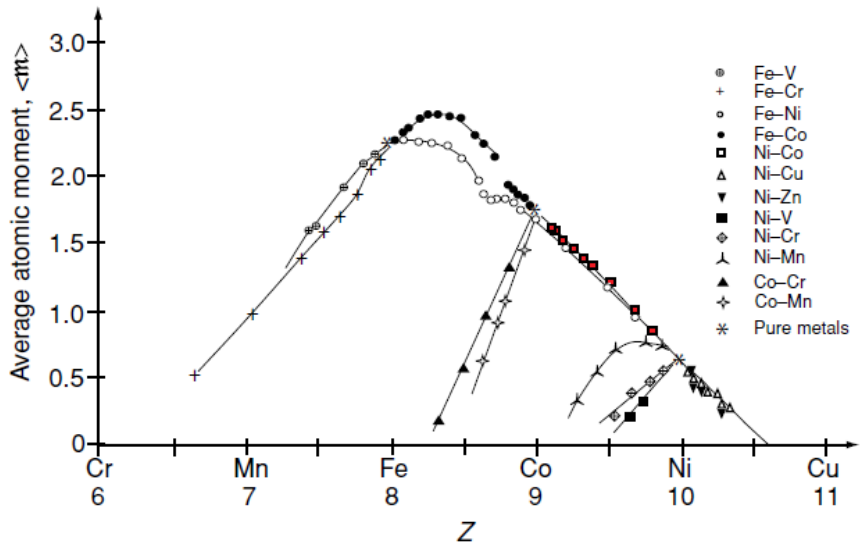

Figure 1.5: The Slater-Pauling curve. Plot of the average atomic moment $\langle m \rangle$ versus the number of valence electrons. The data points corresponding to the Ni-Co alloy is marked in red. Adapted from [11], page 151.

surrounding nanowires.

Ni and Co atoms have different magnetic moments m, 0.58 and $1.71\mu_B$ per atom, respectively. Since the saturation magnetisation M_s is proportional to m, M_s of Co is around three times the magnitude as that of Ni. The magnetostatic energy is proportional to the square of the magnetisation. It thus follows that Ni-Co nanowires with a high Ni content will have lower M_s and reduce the magnetostatic energy. This is described in the famous Slater-Pauling curve, in Figure 1.5 relating the average atomic moment $\langle m \rangle$ to the number of valence $(3d + 4s)$ electrons Z. From this curve it is evident that $\langle m \rangle$ changes linearly for alloys of various Ni-Co compositions. Moreover, the magnetostatic self-energy ϵ_m of a medium of volume V is related to the demagnetising field $\mathbf{H}_d$ and the magnetisation $\mathbf{M}$ through

$$\epsilon_m = -\frac{1}{2}\int_V \mu_0 \mathbf{H}_d \bullet \mathbf{M} d^3 r. \tag{1.14}$$

Dipolar coupling between magnetic layers

The dipolar coupling between the F layers depends on the magnetisation of the layer itself and on the distance to the neighbouring F layers. The spacing between the F layers are controlled by the N layers, which thus controls the dipolar coupling between the F layers. The dipole-dipole interaction between successive cylindrical disk-shaped F layers separated by insulating layers have been calculated theoretically [18]. The calculation was based on the Landau-Lifshitz equation [19] modified for thin-film dimensions. The dipole-dipole interaction between two magnetic layers is expressed by

$$\epsilon_{ij} = C \cos(\phi_i - \phi_j), \tag{1.15}$$

where $i = 1-n$, $j = i-1$, and n is the number of magnetic layers, and $\phi_i - \phi_j$ is the angle between two neighbouring layers. C is the dipole-dipole interaction coefficient between two neighbouring magnetic layers. The dipole-dipole interactions are assumed to be effective only between nearest-neighbour layers. The geometry of the magnetic layers, and thus the demagnetising effects, are

contained in C. The total dipole-dipole interaction energy thus becomes

$$E_{dip} = \sum_{i=1}^{n} \epsilon_{ij}. \tag{1.16}$$

The magnetic layers will naturally align their magnetisations in order to minimise E_{dip}. The dipolar coupling between two magnetic layers is thus minimised by

$$\frac{d\epsilon_{ij}(\phi_i = 0)}{d\phi_j} = \frac{d}{d\phi_j} C\cos(\phi_j) = -C\sin(\phi_j) = 0 \quad \Rightarrow \quad \phi_j = \pi m, \tag{1.17}$$

where $m = 0, 1, 2, 3, ...$ Thus

$$\epsilon(\phi_j = 0) = C$$

and

$$\epsilon(\phi_j = \pi) = -C.$$

As C is always positive, ϵ is minimised for $\phi_j = \pi$, which corresponds to an antiferromagnetic arrangement between the magnetic layers. Antiferromagnetic dipolar coupling contributes significantly to the demagnetising interactions in multilayered magnetic nanowires, and the effect persists for nonmagnetic spacer layers with thickness as large as 600 nm [20]. It can thus be expected that the remanent magnetisation will be very low in samples where the dipolar coupling causes the magnetisations of the F layers to lie antiparallel. The fact that the dipolar coupling results in an antiferromagnetic arrangement at zero field, is very interesting in terms of magnetoresistance. The system can be forced into a parallel state by applying a sufficiently strong magnetic field, but when the field is removed, the system will go back to its antiparallel state. In Section 1.2 it will be shown how the conductivity of electrons with different spin is being affected by the antiparallel and parallel F layer arrangements.

Moreover, the effects of the antiparallel alignment of the F layers have already been discussed in terms of the demagnetising factors and the shape anisotropy of isolated magnetic cylinders in Section 1.1.2 and earlier in this section. A model for the demagnetising fields in multilayered nanowires has been proposed [17]. The layers are assumed to be cylindrical with diameter d and height t_F or t_N, for the F layers and N layers respectively. Under application of a magnetic field parallel to the longitudinal wire axis, the F layers become magnetised collinear to the field, and antiparallel between the layers. This is schematically illustrated in Figure 1.6 for a multilayered system.

The resulting effective demagnetising field for the NiCoCu/Cu multilayered nanowire $H_{eff}^{NiCoCu/Cu}$ can be written

$$H_{eff}^{NiCoCu/Cu} = 1 - 3\left|\sum_{k=0}^{j}(\mathcal{N}_{2k} - \mathcal{N}_{2k+1})\right|, \tag{1.18}$$

where $j = (n-1)/2$, n is the total number of F layers, and $k = 0, 1, 2, ..., j$. $\mathcal{N}$ is in this case values of $\mathcal{N}_{\|}$ of the layer corresponding to the demagnetising field in that layer. Equation 1.18 can be related to the total dipole-dipole interaction energy in Equation 1.16 through Equation 1.14. Note that Equation 1.18, and this discussion in general, is valid for any system of F/N multilayered nanowires, not only the NiCoCu/Cu system.

Dipole-dipole interactions between nanowires

For systems of arrays of nanowires, magnetostatic dipolar interaction between the different nanowires will cause demagnetising effects in the system [14]. This affects the magnetisation reversal properties of the system which can be observed by a tilt in the magnetisation hysteresis curve, that increases with increasing magnetostatic dipolar interaction. Furthermore,

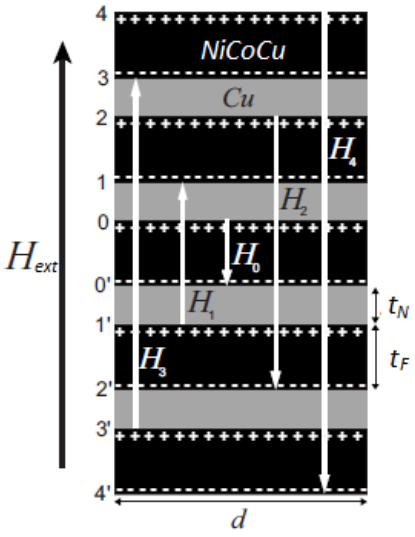

Figure 1.6: Schematic representation of a NiCoCu/Cu ML NW with thicknesses of the N and F layers, t_N and t_F, respectively, and NW diameter d. H_{eff} represents an applied field along the direction of the nanowire, creating stray fields H_n in the layers with alternating directions. Adapted from [17].

the other nanowires can have an effect on the dipoles in F layer dipoles, by adding a term to the magnetostatic dipolar energy in Equation 1.16. This can shift the minimum energy to a corresponding arrangement that is not completely antiparallel anymore. This results in a zero field arrangement which is less antiparallel, than in the case of a single multilayered nanowire.

The magnitude of the magnetostatic dipole-dipole interactions between nanowires is dependent on the distance between the involved dipoles and their magnetisation. The magnitude of the magnetisation of the dipoles are decided by the alloy composition. The distance between them is decided by the packing density and diameter of the nanowires inside the template, that is the porosity. The effective demagnetising field describing the dipolar interactions between parallel nanowires in an array is the following

$$H_{eff}^{int} = 2\pi M_s(1 - 3P), \tag{1.19}$$

where P is the porosity or filling factor of the sample, defined as the product of the pore surface and the areal pore density [21]. Note that this expression is for arrays of parallel nanowires, not for interconnected nanowires as is relevant for this work. Equation 1.19 must therefore only be viewed as an approximation to the case of the interconnected system. Samples from templates with lower porosity can therefore be expected to have a lower contribution of the magnetostatic energy from dipolar interactions between nanowires. This leaves a stronger contribution of the dipolar coupling inside each multilayered nanowire, making the antiparallel arrangement more favoured.

In the light of the model discussed earlier [17], the total effective demagnetising field, including the dipole-dipole effects inside the nanowire and between them, can now be expressed through combination of Equation 1.18 and Equation 1.19 through

$$H_{eff} = H_{eff}^{int} \cdot H_{eff}^{NiCoCu/Cu} = 2\pi M_s(1 - 3P)\left(1 - 3\left|\sum_{k=0}^{j}(\mathcal{N}_{2k} - \mathcal{N}_{2k+1})\right|\right), \tag{1.20}$$

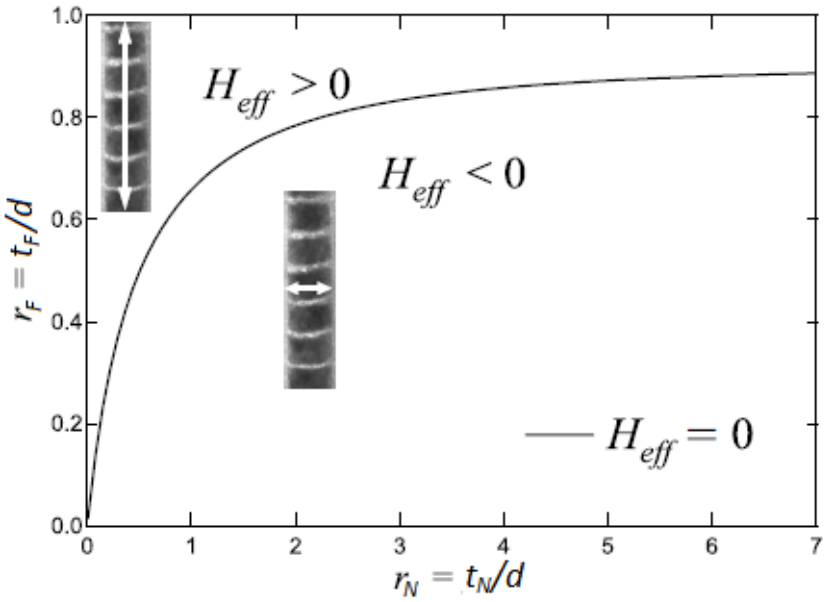

Figure 1.7: Anisotropy diagram showing H_{eff} as a function of the aspect ratios of the F and N layers of a multilayered nanowire array. The easy magnetisation axis is represented by white arrows. Adapted from [17].

which can be inserted into Equation 1.14 along with the magnetisation to obtain the total magnetostatic dipole-dipole interaction energy of the array of parallel multilayered NiCoCu/Cu nanowires. For the case of interconnected nanowires, the author has not found an equivalent models to describe the dipole-dipole interactions between the nanowires. The discussed model must therefore only be considered as an approximation to the interconnected system.

An important feature of the model [17] is its ability to estimate the anisotropy in the F layers, based on the aspect ratios $r_F = t_F/d$ and $r_N = t_N/d$, for the F layer and the N layer respectively. Figure 1.7 shows how H_{eff} is related to the two aspect ratios. There are two zones in this plot. In the zone where $H_{eff} > 0$ the easy magnetisation axis lies perpendicular to the layer plane and parallel to the wire axis. In the zone where $H_{eff} < 0$ the easy axis lies in the F layer plane. At the boundary line between the two zones $H_{eff} = 0$, represents a system with isotropic magnetic properties. In respect to this thesis, it is expected that samples with isotropic magnetic properties ($H_{eff} = 0$) will show the highest magnetoresistance (MR).

1.2 Magnetotransport in magnetic nanowires

From the density of states of a ferromagnet it can be seen that electrons with different spin have different states available at the Fermi level. This causes the electrons to experience different resistance depending on the direction of their spin, which leads to the concept of two separate current channels. The electrons can scatter through certain mechanisms that flip the spin, causing mixing of the current channels. Furthermore, the resistance can change as a consequence of the relative angle between the magnetisation of a ferromagnet that is conducting a current; an effect called *anisotropic magnetoresistance* and is an intrinsic ferromagnetic phenomenon. An extrinsic ferromagnetic phenomenon is the GMR, which is a much larges effect than AMR. GMR can occur when nanoscale ferromagnets are separated by thin nonmagnetic spacer layers in order to manipulate the coupling between them. The case where the current is applied perpendicular to the layers is called the current-perpendicular-to-plane (CPP) geometry. The theory behind CPP-GMR is thoroughly explained by the Valet-Fert model [22].

1.2.1 Intrinsic magnetotransport

The intrinsic magnetotransport effects do not depend the shape or form of a sample [11]. Magnetoresistance can be defined as

$$MR = \frac{\rho(B) - \rho(0)}{\rho(0)}, \tag{1.21}$$

where $\rho(B)$ and $\rho(0)$ are the electrical resistivities at magnetic flux density, B, and $B = 0$, respectively. MR can also be defined $[\rho(B) - \rho(0)]/\rho(B)$, and different definitions are used in the literature. For nonmagnetic metals there is a magnetoresistance effect proportional to B^2 caused by cyclotron motion of the electrons. This effect is very small, approximately 1% at 1 Tesla. In metals, the electronic transport is governed by the electron with energies close to the Fermi energy, E_F. In $3d$ ferromagnets and their alloys, the conduction electrons are in coexisting s-like or d-like states, as shown in Figure 1.1b. The mobility of the electrons in the different bands is given by

$$\mu = e\tau/m^*, \tag{1.22}$$

where e is the elementary charge, τ is the scattering relaxation time, and m^* is the effective mass of the electron which is related to the energy dispersion, $E(k)$, through,

$$m^* \propto \left(\frac{d^2E(k)}{dk^2}\right)^{-1}, \tag{1.23}$$

where $k = 2\pi/\lambda_e$ is the wavenumber, and λ_e is the wavelength of the electron. In other words, the effective mass is inversely proportional to the curvature of the energy bands, meaning that s-states have lower m^* than d states, since the s-bands have larger curvature than the d-bands. Thus, Equation 1.22 can explain the high mobility of s-electrons causing them to carry most of the current. The d-electrons have higher mobility and are relatively ineffective current carriers. In fact, $3d$ electrons are considered as localised, and the $4s$ are considered as nearly free electrons [23].

Because the d-bands are spin-split in ferromagnets, the $\uparrow$ and $\downarrow$ subbands have different density of states at the Fermi level. The s-bands are not spin-split, but the states at the Fermi level hybridise with the d states to attain $\uparrow$ or $\downarrow$ character [11]. When neglecting spin-flip processes, the $\downarrow$ s-electrons in strong ferromagnets can scatter into available $\downarrow$ d states, while the $\uparrow$ s-electrons can not, as there is no available states. This spin-dependent scattering leads to spin asymmetry in the two conduction channels with different transport properties, for electrons with different spin. In other words, the current has been spin polarised by the ferromagnet.

Neglecting spin-flip scattering leads to *Mott's two-current model* [24], where the $\uparrow$ and $\downarrow$ current channels are regarded as independent, and conducting in parallel, with a conductivity which is the sum of the spin-dependent conductivities $\sigma = \sigma_\uparrow + \sigma_\downarrow$, or in terms of the resistivity,

$$\rho = \frac{\rho_\uparrow \rho_\downarrow}{\rho_\uparrow + \rho_\downarrow}, \tag{1.24}$$

where $\rho_\uparrow$ and $\rho_\downarrow$ are the spin-dependent resistivities. The ratio of conductivity in the $\uparrow$ and $\downarrow$ conduction channels are defined by

$$\alpha \equiv \frac{\sigma_\uparrow}{\sigma_\downarrow} = \frac{\rho_\downarrow}{\rho_\uparrow}. \tag{1.25}$$

α is called the spin asymmetry coefficient. Another way of describing the spin asymmetry is through the coefficient β, also called the bulk spin asymmetry coefficient:

$$\beta = \frac{\rho_\downarrow - \rho_\uparrow}{\rho_\downarrow + \rho_\uparrow} = \frac{\alpha - 1}{\alpha + 1}. \tag{1.26}$$

Values of α are given in Table 1.3 for the metals relevant for this work.

Table 1.3: Room-temperature resistivity of metals [10^{-8} Ω m]. Adapted from [11] page 183.

Metal	**Orbitals**	**Magnetisation**	$\rho_\uparrow$	$\rho_\downarrow$	ρ	α
Ni	d-band	Strong ferromagnet	13	65	11	5
Co	d-band	Strong ferromagnet	8	120	7	15
Cu	s-band	Paramagnet	4	4	2	1

1.2.2 Spin-flip scattering

The previous discussion was performed on the assumption that spin-flip scattering could be neglected. This, however, is not true in reality. There are several spin-flip scattering mechanisms that leads to mixing of the spin current channels, and the average distance between spin-flip scattering events is called the spin diffusion length (SDL), denoted l_{sf}. The SDL is typically of the order of 10 nm in metals at room temperature [10], and of the order of 100 nm at low temperature [22]. In the low temperature limit, the residual spin-flip scattering of ferromagnetic metals is due to spin-orbit interactions [22]. The interaction can be described through the total orbital angular momentum $\mathbf{L} = L_x + L_y + L_z$ and the total spin angular momentum $\mathbf{S} = S_x + S_y + S_z$ through

$$\mathbf{L} \bullet \mathbf{S} = L_x S_x + L_y S_y + L_z S_z, \tag{1.27}$$

which can be written through the raising and lowering operators $L^{+(-)}$ and $S^{+(-)}$ as

$$\frac{1}{2}\left(L^+ S^- + L^- S^+\right) + L_z S_z. \tag{1.28}$$

It can then be shown that the spin-orbit interaction mixes the electronic wavefunctions $|\frac{1}{2}, m_\ell\rangle$ with $|-\frac{1}{2}, m_\ell + 1\rangle$, where m_ℓ is the magnetic quantum number [11, 25].

In nonmagnetic metals spin-flip exchange scattering can occur at paramagnetic impurities. In this two-step mechanism magnetisation from the conduction electron is transferred to the paramagnetic impurity by exchange scattering. Then the localised spin on the impurity can interact with the lattice through spin-orbit interaction.

At relatively high temperatures electron-magnon interactions lead to mixing of the spin current channels. Magnons are quantised spin waves (bosons) with a wave vector $\mathbf{q}$ and energy $\epsilon_q = \hbar\omega_q$ [11]. They can be thought of as oscillations in the relative orientations of spins on a lattice. Magnon excitation is responsible for the decreasing magnetisation with increasing temperature T. In 3D solids, ferromagnetic magnons have a dispersion of $\epsilon_q \approx D_{sw} q^2$, where D_{sw} is the spin-wave stiffness parameter, and a contribution to the low-temperature specific heat proportional to $T^{3/2}$. At low temperatures, the reduction in magnetisation due to magnon excitation is given by the Bloch $T^{3/2}$ power law:

$$\Delta M/M_0 = (0.0587/\nu)(k_B T/2S\mathcal{J})^{3/2}, \tag{1.29}$$

where ν equals 1, 2 or 4 for a simple cubic, bcc or fcc lattice, k_B is the Boltzmann constant, and $\mathcal{J}$ is the exchange constant. In ferromagnetic metals, conduction electrons can interact with magnons leading to an additional scattering mechanism. With the creation or annihilation of a magnon, an electron can inelastically spin-flip scatter. This scattering leads to a contribution to the resistivity varying with T^2.

1.2.3 Anisotropic magnetoresistance

Anisotropic magnetoresistance (AMR) is an effect related to intrinsic magnetotransport. It depends on the relative orientation of current and magnetisation [11]. The resistance of a

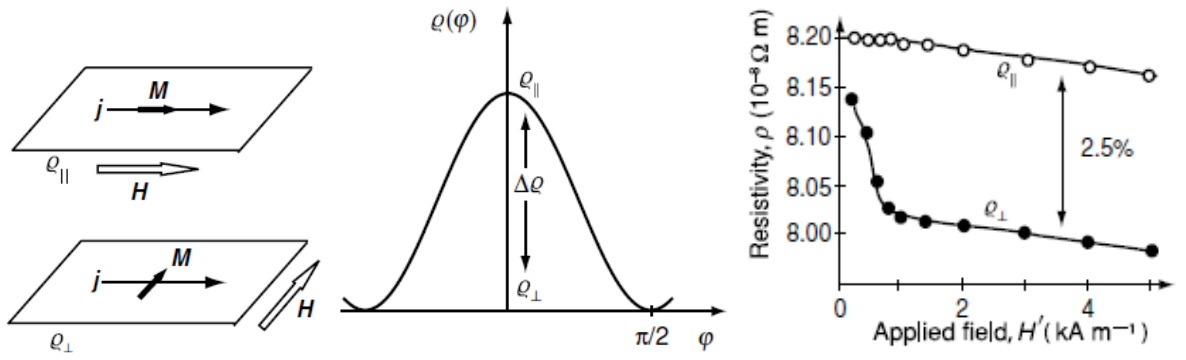

(a) (b) (c)

Figure 1.8: (a) Schematic illustration of AMR for a thin film. (b) AMR of a permalloy film. (c) The angular dependence of AMR. Copied from [11], page 184-185.

ferromagnet is in most cases higher when the current flows parallel ($\|$) to an applied magnetic field than when it flows perpendicular ($\perp$) to it. The resistivity of the ferromagnet in the two cases are denoted $\rho_\|$ and $\rho_\perp$, respectively. The angle, φ, between the current density $\mathbf{j}$ and the magnetisation $\mathbf{M}$ affects the resistivity as follows

$$\rho(\varphi) = \rho_\perp + (\rho_\| - \rho_\perp)\cos^2\varphi. \tag{1.30}$$

By applying an external magnetic field the magnetisation can be saturated in the parallel and perpendicular directions, thus allowing measurements to obtain $\rho_\|$ and $\rho_\perp$, as shown in Figure 1.8a. The angular dependence has a dependence on $\cos^2\varphi$ according to Equation 1.30. This dependence is shown in Figure 1.8b.

The reason for the angle dependent resistivity is the angle dependent probability of $4s$ conduction electron scattering into the localised $3d$ states, as described earlier. This scattering is in fact caused by spin-orbit interactions, and the scattering probability is determined by the spin-orbit scattering cross section σ_{so} [26]. σ_{so} is largest when the magnetisation lies parallel to the current direction, and lowest when the magnetisation lies perpendicular to the current. The scattering probability is thus maximum in the parallel case, and minimum in the perpendicular case, and the resistivity follows accordingly.

The maximum AMR is defined as

$$AMR = \frac{(\rho_\| - \rho_\perp)}{\rho_{avg}}, \tag{1.31}$$

where $\rho_{avg} = 1/3\rho_\| + 2/3\rho_\perp$ is the average resistance of a demagnetised medium at zero field [26]. The AMR is typically only a few percent. An example of the AMR effect of 2.5% is illustrated for a permalloy ($Ni_{80}Fe_{20}$) film in Figure 1.8c. Since $\rho_\|$ is usually larger than $\rho_\perp$, the AMR is usually positive.

Figure 1.9(a) shows how the resistivity changes in a multi-domain ferromagnet from ρ_{avg} at zero field to either of the two configurations depending on the applied field direction. Figure 1.9(b) shows this in the case of ferromagnetic single-domain nanowires, where shape anisotropy results in a single domain magnetisation along the wire axis at zero field, and thus the highest resistance state.

The Ni-Co alloy is expected to show a significant AMR effect, and the alloy composition

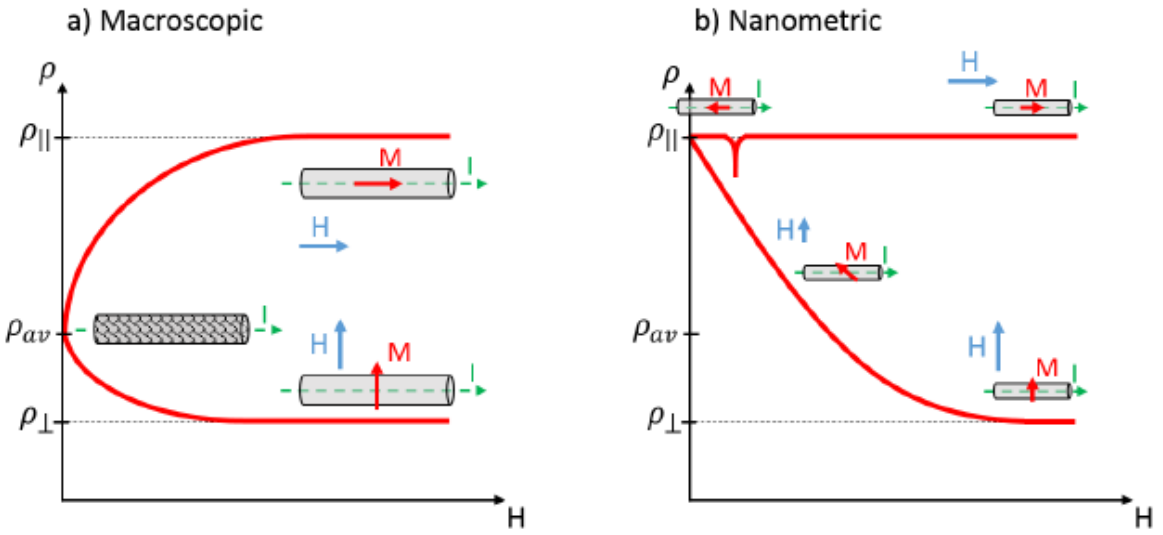

Figure 1.9: Resistivity ρ versus applied field H for (a) a macroscopic ferromagnetic medium, and (b) a ferromagnetic nanowire. The two limiting scenarios of **M** parallel and perpendicular to the current **I** are indicated by $\rho_\perp$ and $\rho_\parallel$.

will affect the AMR. The AMR as a function of Ni concentration in Co is shown in Figure 1.10, and it clearly shows that the AMR effect in the alloy is stronger than in any of the pure constituents. The maximum AMR of around 6% is expected around a composition of 75% Ni [26].

1.2.4 Giant magnetoresistance in multilayered nanowires

Giant magnetoresistance (GMR) in nanowires is the main topic of this work. The phenomenon of GMR is not an intrinsic effect like AMR, but a very large effect resulting from interplay between multilayered heterostructures of ferromagnetic and nonmagnetic materials. From a practical viewpoint, magnetoresistance is the most important property of magnetic multilayers. In 1988, the GMR effect was discovered in antiferromagnetically coupled Fe-Cr multilayers [5, 6]. Because the effect was measured to some tens of per cent, much larger than the intrinsic AMR effect, it was dubbed giant magnetoresistance. The GMR effect can be measured with two different configurations: the current in plane (CIP) and the current perpendicular to to the plane (CPP) geometries, where the plane corresponds to the plane parallel to the layers. It has been shown that the the a much larger GMR effect can be achieved with the CPP geometry than with the CIP geometry [8]. This section will present an overview of the physics related to the CPP-GMR effect in nanowires, while the theoretical explanation according to the Valet-Fert model will be covered in Section 1.2.5.

The GMR effect arises in systems of alternating layers of ferromagnetic and nonmagnetic layers. It was explained in Section 1.2.1 how the intrinsic properties of ferromagnets lead to spin-dependent scattering which is different for the two spin-current channels. The special feature of the multilayered system is that the N spacer layer allows the magnetisation of the F layers to have different directions. And as explained earlier, the spin-dependent resistance inside a F layer depends on the direction of the spin relative to the direction of the magnetisation.

A prerequisite for the exhibition of GMR is that the F layers can orient themselves antiparallel relative to each other at zero applied field (or close to zero). This scenario corresponds to the case illustrated in Figure 1.11(a). In this case the two spin current channels will experience different resistance in the first F layer, but in the second F layer the magnetisation is opposite.

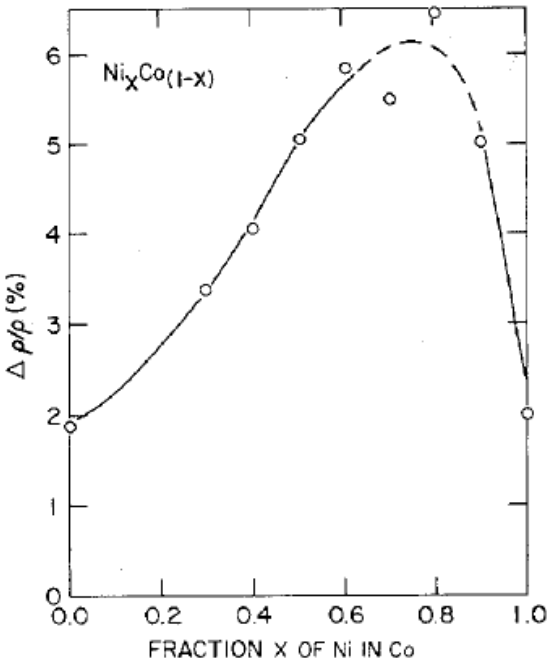

Figure 1.10: AMR at room temperature of different compositions of the Ni-Co alloy. Copied from [27].

Thus the density of states for the majority and minority spin channels are the opposite of the previous F layer, causing the resistance of the spin current channels to switch. In other words, $\rho_\uparrow$ and $\rho_\downarrow$ alternates for each F layer. The result is that over the entire multilayer system, the total resistance experienced by the two spin current channels will be equal, according to the resistor scheme in Figure 1.11(a), with a resistivity of $(\rho_\uparrow + \rho_\downarrow)/2$ for both channels.

Upon application of a sufficiently strong magnetic field, the magnetisations in all the F layers can be aligned parallel to each other, as shown in Figure 1.11(b). In this case the density of states will be similar in all the F layers, hence the resistance of the spin current channels will have the same value in all the F layers. For the majority ($\uparrow$) channel the resistivity $\rho_\uparrow$ is always less than the minority ($\downarrow$) channel resistivity $\rho_\downarrow$. To compare the two cases presented, $H = 0$ and $H > H_{sat}$, where H_{sat} is the saturation field (parallel alignment), the resistor schemes in Figure 1.11 shows two equal resistors of relatively intermediate resistivities, $(\rho_\uparrow + \rho_\downarrow)/2$, connected in parallel ($H = 0$), and in the other case ($H > H_{sat}$) two resistances in parallel where one is low, $\rho_\uparrow$, and the other is high, $\rho_\downarrow$. The resistance corresponding to the parallel R_P ($H > H_{sat}$) and the antiparallel R_{AP} ($H = 0$) scenarios can be written

$$R_P^{-1} = R_\uparrow^{-1} + R_\downarrow^{-1}, \tag{1.32}$$

and

$$R_{AP} = (R_\uparrow + R_\downarrow)/4, \tag{1.33}$$

respectively. This shows that the R_{AP} will always be larger than R_P. This phenomenon is the GMR effect. The maximum GMR is defined as

$$GMR = \frac{R_{AP} - R_P}{R_P}. \tag{1.34}$$

Typical resistance curves for multilayers of Fe/Cr thin films are shown in Figure 1.12a for

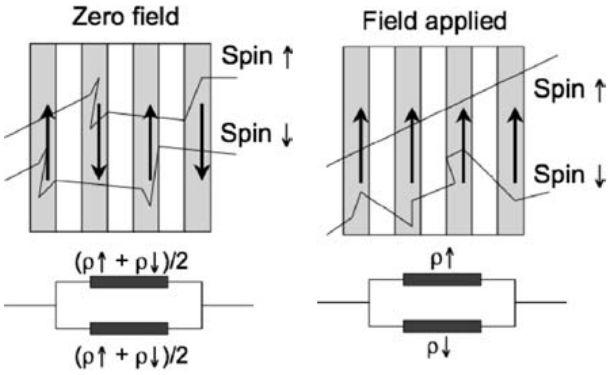

Figure 1.11: Figures of the multilayer arrangements at zero field (antiparallel) and at saturation field (parallel). The magnetisations of the gray F layers are indicated with arrows, and the two spin channels are indicated by black lines, where the straight line resembles conduction without scattering and the kinks in the other lines resembles spin-dependent scattering centres. Corresponding resistor schemes. Copied from [11], page 284.

systems with fixed Fe layer thickness and varying Cr spacer layer thickness. The GMR for the samples with 9 Å Cr layers are around 80% calculated from Equation 1.34. The highest GMR are reached in the sample with lowest spacer thickness. The nonmagnetic spacer layer thicknesses for this system is much less than the expected thicknesses of the samples used for this thesis. An important difference between multilayers with small and large spacer thickness is the type of coupling that leads to the antiparallel arrangement of the F layers. In systems where the spacer thickness is a few nm or less, the coupling between the F layers are dominated by exchange coupling. The magnitude of the exchange coupling oscillates with the spacer thickness. When the exchange coupling is positive the coupling is ferromagnetic, while it is antiferromagnetic when the exhange coupling is negative, as shown in Figure 1.12b. However the same figure shows that the exchange coupling goes to zero as the spacer thickness increases. The spacer thicknesses relevant for this thesis can be assumed to be around 10 nm and larges, meaning that the exchange coupling can be neglected. The dominating coupling for multilayers with spacer thicknesses in this regime is the dipolar coupling, which was discussed in Section 1.1.4.

The picture presented in so far in this section is somewhat simplified. It has been assumed that the resistance has only been governed by the properties of the bulk ferromagnet. The contributions to the resistance from both the bulk nonmagnetic spacer and the interface between the layers have been neglected. In fact, the interface scattering is spin-dependent and provides an important contribution to the resistances, leading to an increased difference between R_{AP} and R_P. The resistivity of the nonmagnetic spacer, Cu in this work, is very low compared to that of the F layer. Nor is the resistivity of pure Cu spin-dependent ($\alpha = 1$), so it does not affect the spin asymmetry. However, paramagnetic impurities in the Cu layer can lead to spin-dependent scattering [22]. The theory of CPP-GMR in magnetic multilayers are covered in the Valet-Fert model [22], which is discussed in the next section.

1.2.5 Valet-Fert model

As mentioned in the previous section, the interface resistance between the layers brings an important contribution to the resistance, which greatly influences the magnetotransport properties in multilayered nanowires. The electron transport through an interface between a F and N layer can be described by using the concept of "spin-coupled interface resistance" [29, 30, 31]. If the current in a ferromagnet is spin polarised, there will be spin accumulation around the interface with the N layer. This gives rise to an additional potential drop $\Delta V_I = Jr_{SI}$, where J is the

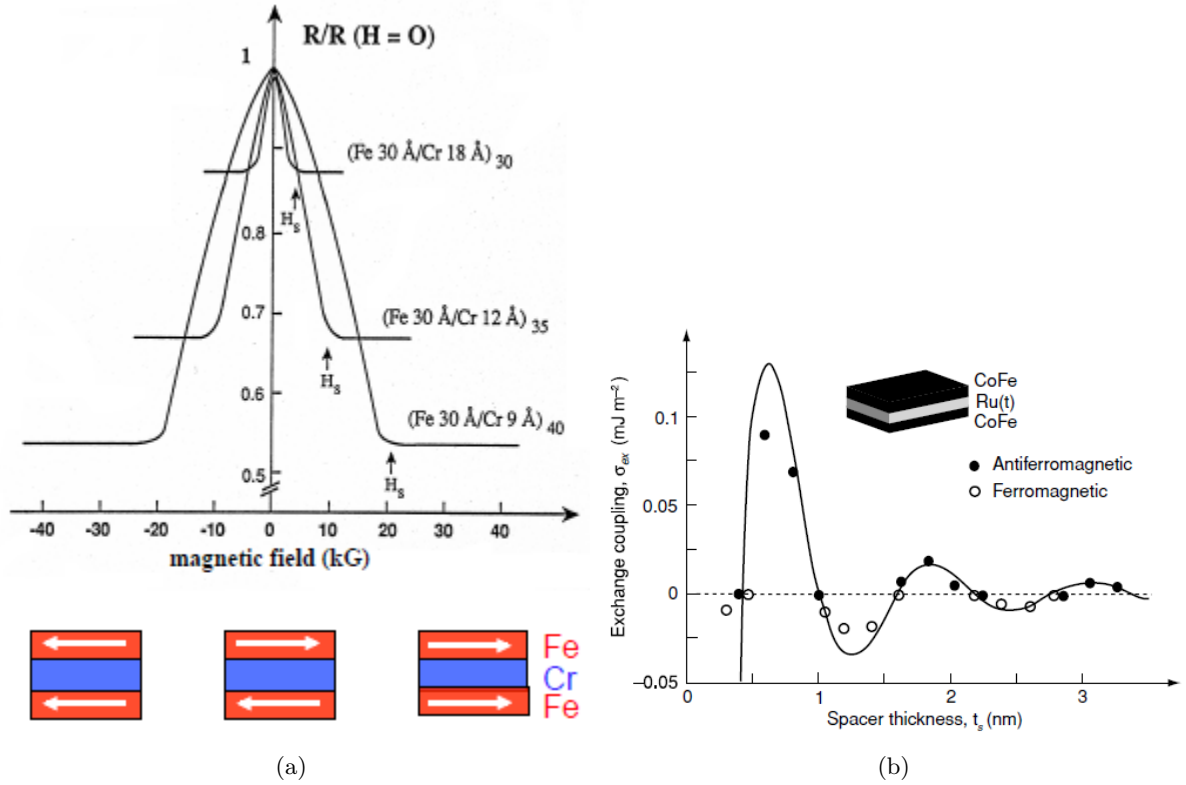

(a) (b)

Figure 1.12: (a) Resistance versus applied field for multilayered thin films of Fe and Cr, with different Cr spacer thickness. Adapted from [5]. (b) Exchange coupling as a function of spacer thickness for CoFe/Ru multilayers. Copied from [28].

current density, and r_{SI} is the "spin-coupled interface resistance".

The Valet-Fert (VF) model can be used to calculate the transport properties of multilayered magnetic nanowires in the CPP geometry [22, 1]. The model takes both volume and interface spin-dependent scattering into account. Unlike earlier models [32], the VF model also takes into account the spin accumulation occurring at the interfaces. It shows that the spin-accumulation at successive interfaces interfere and partly balances each other. Thus the r_{SI} over successive interfaces cannot be assumed to be additive. The validity of this model is within the long spin-diffusion length (SDL) limit, that is the range where the SDLs, l_{sf}^F and l_{sf}^N is much longer than the electron mean free path (MFP), λ, which is the average distance between normal momentum scattering events.

The VF model proves that within the long SDL limit, the Boltzmann equation model reduces to a macroscopic model to describe the electron transport. The model proposes an additional "Boltzmann correction" term to the macroscopic transport equations, given by Equation 9 in [22], which is too rigorous to be given here. For the following, consider the term t as both t_F and t_N, and l_{sf} as both l_{sf}^F and l_{sf}^N unless stated othwerwise. When the layer thicknesses are much smaller than the SDL, $t \ll l_{sf}$, it turns out that the "Boltzmann correction" term becomes proportional to λ_s/l_{sf}, where λ_s is the local electron mean free path λ for a spin s. Thus the "Boltzmann correction" term goes to zero when $l_{sf} \gg \lambda_s$, and the transport equations reduce to the macroscopic ones. The nanowire networks in this thesis can be expected to have layer thicknesses much less than the SDL, thus obeying the macroscopic transport equations.

In the macroscopic model the current densities are related to the electrochemical potentials, μ_s,

through the equations

$$\frac{e}{\sigma_s}\frac{\partial J_s}{\partial z} = \frac{\bar{\mu}_s - \bar{\mu}_{-s}}{l_{sf}^2}, \tag{1.35}$$

$$J_s = \frac{\sigma_s}{e}\frac{\partial \bar{\mu}_s}{\partial z}, \tag{1.36}$$

where σ_s is the conductivity, and the index s denotes the spin channel $\uparrow$ or $\downarrow$. Equation 1.35 expresses that, in steady state, the spin accumulation close to the interfaces are balanced by the spin-flip processes. Equation 1.36 is the Ohm's law. Within the long SDL limit it can be expected that the conduction electrons experience normal momentum scattering events much more frequent than spin-flip scattering events. For multilayers of alternating F and N layers, the thickness of one bilayer, that is $t_{bl} = t_F + t_N$, must be smaller than the SDL. If this is the case, the polarisation of the spin-currents, hence the spin asymmetry of the channels, will be contained within the bilayer. If the SDL $< t_{bl}$, spin-flip scattering will occur between the F spin polarisers, resulting in mixing of the spin channels and decrease in the spin asymmetry. As described in Section 1.2.1, spin dependent scattering is mainly contributed to temperature-dependent electron-magnon scattering, temperature independent spin-orbit scattering and scattering on paramagnetic impurities in the N layers. Therefore, a prerequisite for high spin asymmetry is low temperature, to reduce the magnon scattering, and materials with low spin-orbit coupling, to reduce spin-orbit scattering. Spin-orbit coupling increases with X^4, where X is the atomic number, hence $3d$ elements like Co and Ni should exhibit low spin-orbit coupling. The VF model predicts $l_{sf} \approx 10\lambda$ for multilayered systems composed of $3d$ elements coupled with Cu, in the low temperature limit. This result justifies the assumption of long SDL limit, that reduces the transport equations to the macroscopic equations.

In the macroscopic model, the transport in the bulk material and across the interface can be treated separately. The spin-dependent bulk resistivity in the F layers can be expressed through

$$\rho_{\uparrow(\downarrow)} = \frac{1}{\sigma_{\uparrow(\downarrow)}} = 2\rho_F[1 - (+)\beta], \tag{1.37}$$

where ρ_F is the normal resistivity of the F material obtained from the Drude model [33], and β is the *bulk spin asymmetry coefficient*:

$$\rho_F = \frac{m^*}{ne^2\tau}, \tag{1.38}$$

where m^* is the effective mass of the electron, n is the number density of electrons and $\tau = \lambda/\nu_F$ is the time between normal momentum scattering events. ν_F is the Fermi velocity. In the NM layers the resistivity is defined as

$$\rho_{\uparrow(\downarrow)} = 2\rho_N, \tag{1.39}$$

where ρ_N is the normal resistivity of the NM material, and γ is the *interface spin asymmetry coefficient*. In NiCoCu/Cu multilayered nanowire arrays β has been estimated to be below 0.37, giving $\alpha \leq 2.17$ from Equation 1.26, and $\gamma >$0.76 [10].

The interface is defined as an interfacial zone supposed to be infinitesimally thin, and interface scattering occurs in this zone. The interface resistance can be defined as

$$r_{\uparrow(\downarrow)} = 2r_b[1 - (+)\gamma], \tag{1.40}$$

where r_b is the normal interface resistance.

For multilayered nanowires of either parallel (P) or antiparallel (AP) arrangement of the magnetisations of the F layers, and when the layer thicknesses are much smaller than the SDL, that is

$(t_F, t_N) \ll l_{sf}$, and only bulk spin-dependent scattering is assumed, the resistance of one bilayer can be expressed through

$$r^{(P,AP)} = \frac{1}{1/r_+^{(P,AP)} + 1/r_-^{(P,AP)}}, \tag{1.41}$$

with

$$r_{+(-)}^{(AP)} = \frac{r_+^{(P)} + r_-^{(P)}}{2}, \tag{1.42}$$

and

$$r_{+(-)}^{(P)} = 2\rho_F[1 + (-)\beta]t_F + 2\rho_N t_N. \tag{1.43}$$

Here, the $+(-)$ indices respectively indicate the current channels of positive and negative spin values. From this the absolute resistance change from P to AP configuration is given by

$$r^{(AP)} - r^{(P)} = \beta^2 \frac{(\rho_F t_F)^2}{\rho_N t_N + \rho_F t_F}. \tag{1.44}$$

In the case of multilayered nanowires with both bulk and interface spin-dependent scattering, the total resistance, $R^{(P,AP)}$ for a multilayer composed of M bilayers can be written as

$$R^{(P,AP)} = M(r_0 + 2r_{SI}^{(P,AP)}), \tag{1.45}$$

with

$$r_0 = (1 - \beta^2)\rho_F t_F + \rho_N t_N + 2(1 - \gamma^2)r_b, \tag{1.46}$$

where r_0 simply is the resistance of a F layer in electrical series with a N layer. The spin-coupled interface parts are given in the parallel case by

$$r_{SI}^{(P)} = \frac{\frac{(\beta-\gamma)^2}{\rho_N l_{sf}^{(N)}} \coth\left[\frac{t_N}{2l_{sf}^{(N)}}\right] + \frac{\gamma^2}{\rho_F l_{sf}^{(F)}} \coth\left[\frac{t_F}{2l_{sf}^{(F)}}\right] + \frac{\beta^2}{r_b}}{\frac{1}{\rho_N l_{sf}^{(N)}} \coth\left[\frac{t_N}{2l_{sf}^{(N)}}\right] \frac{1}{\rho_F l_{sf}^{(F)}} \coth\left[\frac{t_F}{2l_{sf}^{(F)}}\right] + \frac{1}{r_b}\left[\frac{1}{\rho_N l_{sf}^{(N)}} \coth\left[\frac{t_N}{2l_{sf}^{(N)}}\right] + \frac{1}{\rho_F l_{sf}^{(F)}} \coth\left[\frac{t_F}{2l_{sf}^{(F)}}\right]\right]}, \tag{1.47}$$

and in the antiparallel case by

$$r_{SI}^{(AP)} = \frac{\frac{(\beta-\gamma)^2}{\rho_N l_{sf}^{(N)}} \tanh\left[\frac{t_N}{2l_{sf}^{(N)}}\right] + \frac{\gamma^2}{\rho_F l_{sf}^{(F)}} \coth\left[\frac{t_F}{2l_{sf}^{(F)}}\right] + \frac{\beta^2}{r_b}}{\frac{1}{\rho_N l_{sf}^{(N)}} \tanh\left[\frac{t_N}{2l_{sf}^{(N)}}\right] \frac{1}{\rho_F l_{sf}^{(F)}} \coth\left[\frac{t_F}{2l_{sf}^{(F)}}\right] + \frac{1}{r_b}\left[\frac{1}{\rho_N l_{sf}^{(N)}} \tanh\left[\frac{t_N}{2l_{sf}^{(N)}}\right] + \frac{1}{\rho_F l_{sf}^{(F)}} \coth\left[\frac{t_F}{2l_{sf}^{(F)}}\right]\right]}. \tag{1.48}$$

In the limit where the individual layer thicknesses are much smaller than their respective SDL, Equation 1.42 remains unchanged, while the spin-dependent interface resistance adds up in Equation 1.43 to give

$$r_{+(-)}^{(P)} = 2\rho_F[1 + (-)\beta]t_F + 2\rho_N t_N + 4r_b[1 + (-)\gamma]. \tag{1.49}$$

This corresponds to the resistor schemes shown in Figure 1.13 for both P and AP configuration.

In the case of randomly distributed up and down magnetisations with with a total magnetisation equalling zero, the results above can be used to show that this will lead to the same resistance as in the AP configuration [34]. However, this only applies if the magnetisation averages to zero within l_{sf}.

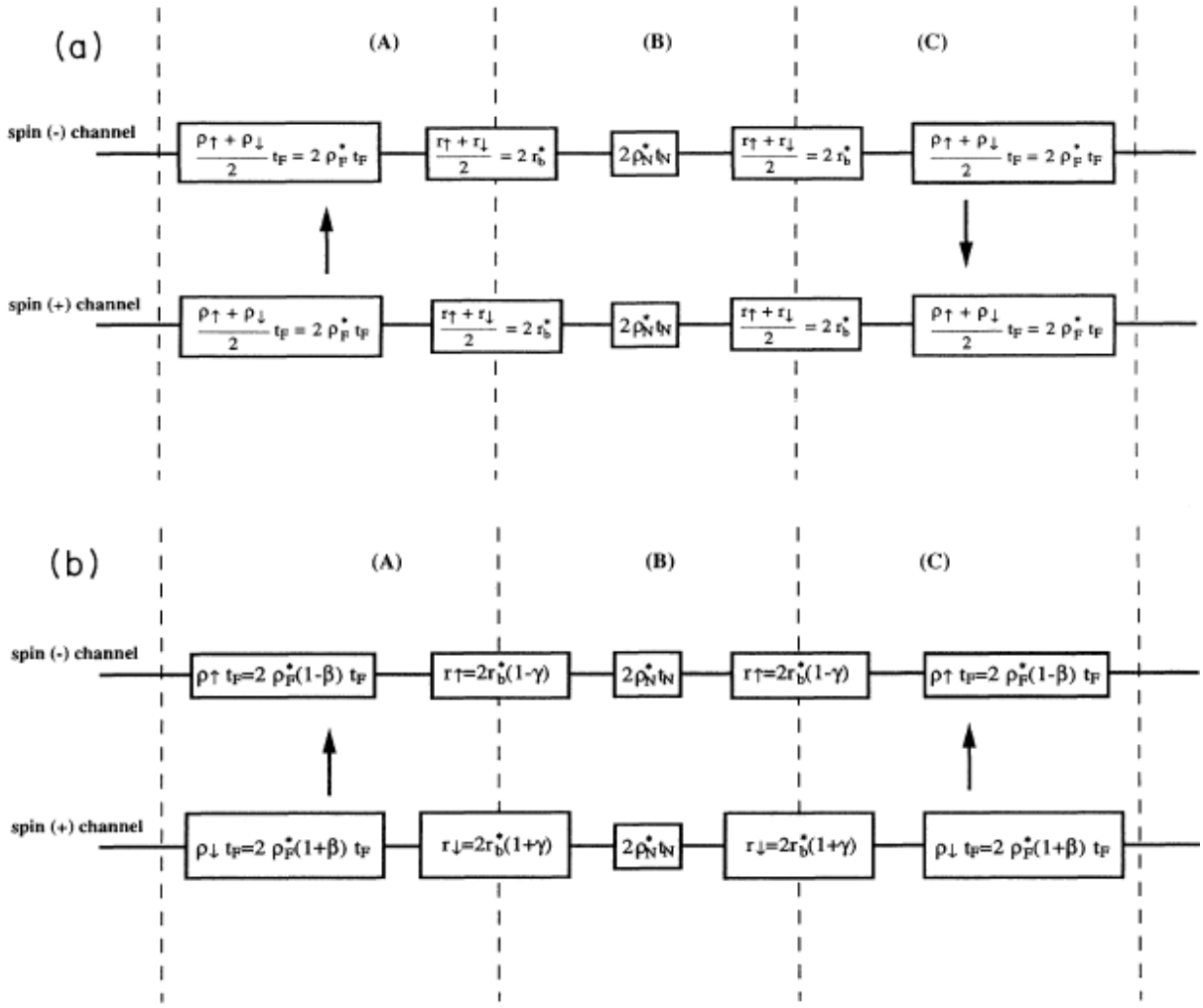

Figure 1.13: Equivalent resistance scheme of the array of multilayers in the limit $(t_N, t_F) \ll l_{sf}$, for both bulk and interface spin-dependent scattering. The regions (A) and (C) indicate the F layers, while (B) indicates the N layer. The vertical dashed lines indicate the interfaces between the regions. The arrows in (A) and (C) resembles the direction of magnetisation in the layer. (a) is for an AP arrangement and (b) is for a P arrangement. $\rho_\uparrow$ and $\rho_\downarrow$ are the resistivities corresponding to the spin-dependent bulk scattering. $r_\uparrow$ and $r_\downarrow$ are the resistances induced by spin-dependent interface scattering. Copied from [22].

Equation 1.42 and 1.49 can be used to give expressions suitable for interpretations of experimental results on multilayers with M bilayers:

$$R^{(AP)} = M(\rho_F t_F + \rho_N t_N + 2r_b), \tag{1.50}$$

$$\frac{1}{R^{(P)}} = \frac{1}{M}\left[\frac{1}{2\rho_F(1-\beta)t_F + 2\rho_N t_N + 4r_b(1-\gamma)} + \frac{1}{2\rho_F(1+\beta)t_F + 2\rho_N t_N + 4r_b(1+\gamma)}\right]. \tag{1.51}$$

This leads to

$$R^{(P)} = R^{(AP)} - \frac{(\beta\rho_F\left[\frac{t_F}{t_F+t_N}\right]L + 2\gamma r_b M)^2}{R^{(AP)}}. \tag{1.52}$$

Here, L is defined as $L \equiv M(t_F + t_N)$, and is thus the total thickness of the multilayer. The expression generally used for the interpretation of multilayered nanowires can be written [35, 36]:

$$\left(\frac{R^{(AP)} - R^{(P)}}{R^{(AP)}}\right)^{-1/2} = \frac{\rho_F t_F + 2r_b}{\beta\rho_F t_F + 2\gamma r_b} + \frac{\rho_N t_N}{\beta\rho_F t_F + 2\gamma r_b}, \tag{1.53}$$

which is closely related to the definition of GMR given in Equation 1.34. Equation 1.53 shows that $[(R^{(AP)} - R^{(P)})/R^{(AP)}]^{-1/2}$ varies linearly with t_N when t_F is kept constant.

Derived from Equation 1.50-1.52, $R^{(AP)}$ and $R^{(P)}$ as a function of number of bilayers M and with a constant total thickness L are plotted in Figure 1.14. The plots are for the limiting cases where only spin-dependent interface scattering occurs, that is $\beta = 0$ (1.14a), and for the opposite case where only spin-dependent bulk scattering occurs, that is $\gamma = 0$ (1.14b). The figures are valid in the same range of validity as the equations they are derived from: when $t \ll l_{sf}$, or in other terms: $M \gg L/l_{sf}$. Figure 1.14a shows that for interface spin-dependent scattering $(R^{(AP)} - R^{(P)})$ is an increasing function of M. $R^{(P)}$ starts nonlinear, but for a certain critical number of bilayers M_c

$$M \geq M_c = \frac{L(\rho_F + \rho_N)}{2r_b}, \tag{1.54}$$

$R^{(P)}$ becomes linear with a smaller slope than that of $R^{(AP)}$. As shown in Figure 1.14b $(R^{(AP)} - R^{(P)})$ is a decreasing function of M for bulk spin-dependent scattering.

Note that the relative magnitude of the bulk and interface contributions in Equation 1.52 depends on M and thus the layer thicknesses. For thicknesses more than a few hundred Ångströms, the interface contribution can be expected to be exceeded by the bulk contribution. As the layer thicknesses relevant for this thesis is of the order of 10 nm, or 100 Å, both contributions must be expected to be of importance.

Until now, only the limiting case of $t \ll l_{sf}$ has been discussed. However, in the limiting cases where either $t_N \gg l_{sf}^N$ or $t_F \gg l_{sf}^F$, the VF model predicts different results for the GMR. When $t_N \gg l_{sf}^N$ the GMR change is predicted to decrease with increasing t_N in the form of $exp(-t_N/l_{sf}^N)$. In the opposite case, when $t_N \ll l_{sf}^N$ and $t_F \gg l_{sf}^F$, the GMR is inversely proportional to t_F through:

$$\frac{R^{(AP)} - R^{(P)}}{R^{(P)}} = \frac{2p\beta^2 l_{sf}^F}{(1-\beta^2)t_F}, \tag{1.55}$$

where p is the fraction of consecutive magnetic layers having magnetisations aligned antiparallel. $p = 1$ for perfectly antiparallel alignment, $p = 0$ for parallel alignment, and $p = 0.5$ for a random alignment.

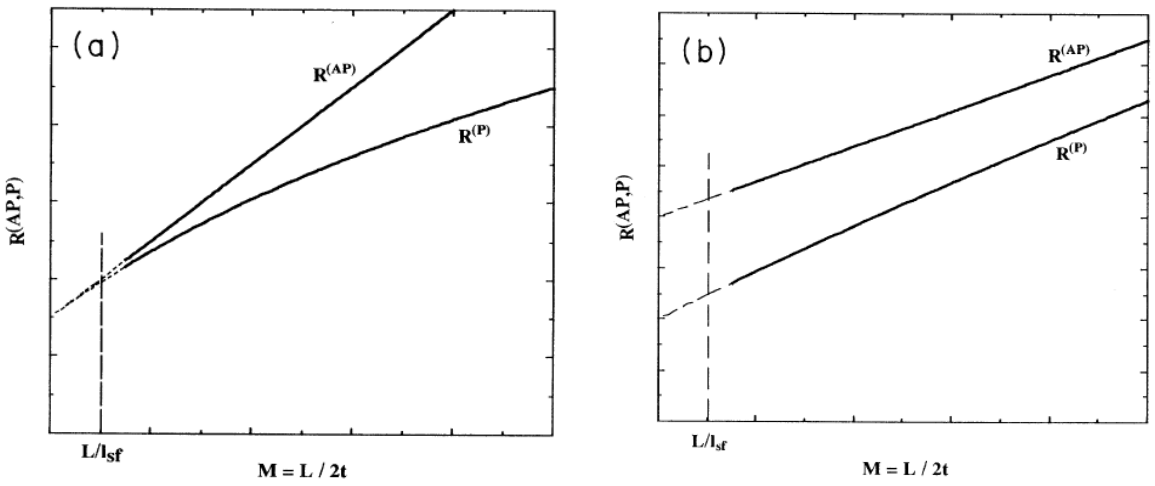

(a) (b)

Figure 1.14: Variation of CPP resistance of a multilayered system as a function of number of bilayers M for a fixed total thickness L, and $t_F = t_N = t$. For the limiting cases where (a) only interface spin-dependent scattering takes place ($\beta = 0$), and (b) only bulk spin-dependent scattering takes place ($\gamma = 0$). Derived from Equation 1.50-1.52. Copied from [22].

To summarise the VF model for CPP-GMR, there exist spin accumulation effects and the SDL is the unique damping length. In multilayers of alternating $3d$ and noble metals the SDL is expected to be very long in the low-temperature limit; above 10^3 Å. Here the spin-orbit and exchange scattering contributes to the SDL. In the usual cases: the long SDL limit, where the mean free path is much shorter than the SDL, the Boltzmann equation approach reduce to the macroscopic approach. In the limit where t_F and t_N are much smaller than their respective SDLs, the resistance of the two different magnetic configurations, $R^{(AP)}$ and $R^{(P)}$, can be described by the series-resistor schemes shown in Figure 1.13. The total resistances depend on t_F, t_N and the number of bilayers M, as well as the normal, spin-independent, resistivities in the F and N layers, ρ_F and ρ_N and the interface resistance r_b, along with the spin asymmetry coefficients β and γ, corresponding to bulk and interface, respectively. β and γ accounts for the spin-dependent parts of the resistivity. β is also defined earlier in Equation 1.26. Finally, the expression suitable for interpreting results on multilayered nanowires were deduced in Equation 1.53, which is $1/\sqrt{(MR)}$, showing how the MR is related to the mentioned parameters, especially the linear dependence related to t_N. Additionally, in the limit where $t_N \ll l_{sf}^N$ and $t_F \gg l_{sf}^F$, the GMR is inversely proportional to t_F.

1.3 Electrochemical deposition in track-etched polymer membranes

Arrays of nanowires be prepared in track-etched polycarbonate (PC) membrane templates [37, 38]. The membranes are prepared from polycarbonate (PC) thin films, bombarded with heavy ions to create traces of broken polymer chains in the thin film. By subsequent etching of the traces with aqueous sodium hydroxide (NaOH(aq)), well-defined cylinder shaped pores with diameters down to 15 nm and up to a few μm can be realised. This process is illustrated in Figure 1.15 The process is well-controlled and produces template membranes with very sharp pore size distributions. More recently templates with crossed pores have been prepared by irradiating the polymer film from different angles [40]. These are suitable for preparing samples of interconnected nanowire networks with controlled packing density, angle dispersion, and nanowire diameter, such as the those illustrated in Figure 1.16 and 1.17. One surface of the templates can be covered with a thin

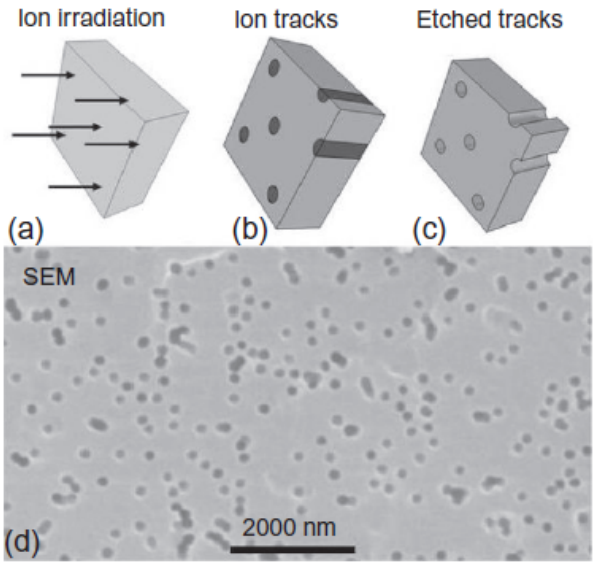

Figure 1.15: Fabrication scheme of a track-etched membrane showing (a) ion bombardment, (b) tracks formed in the polymer, (c) etched pores, and (d) a SEM image of the surface of a finished membrane. Copied from [39].

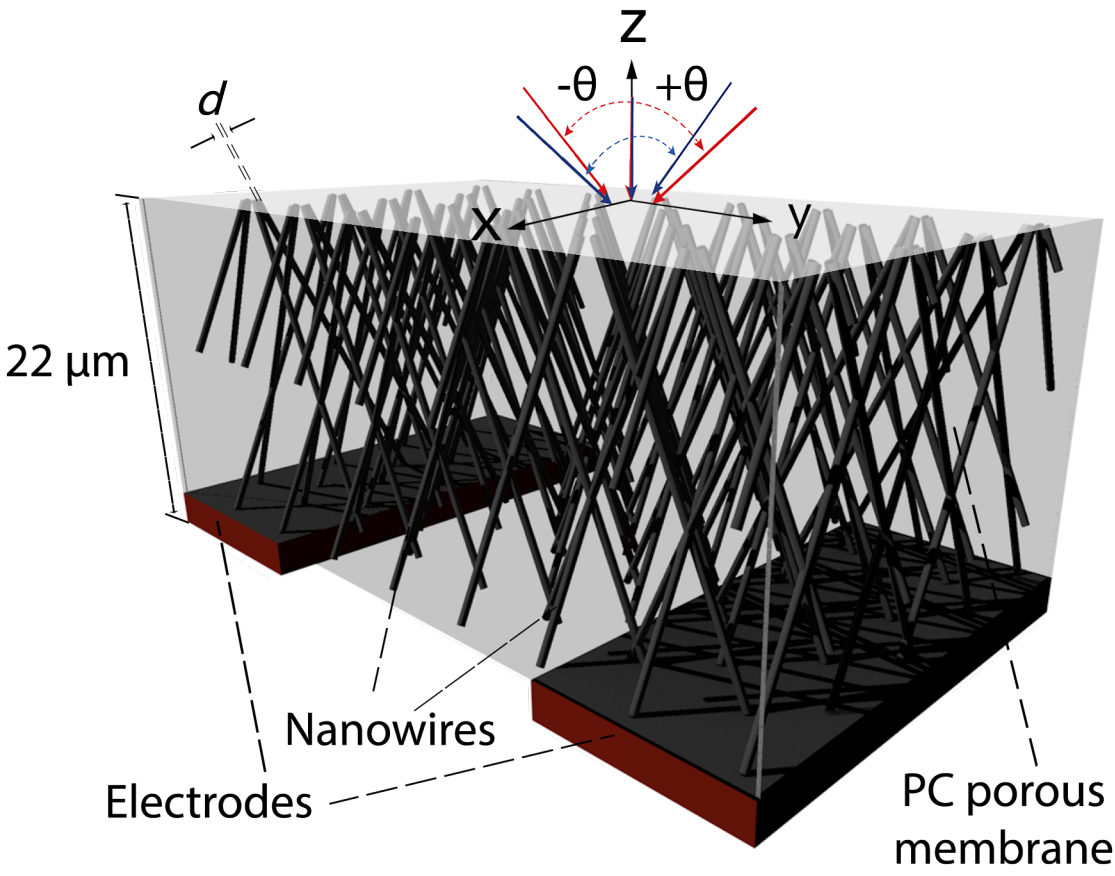

Figure 1.16: Schematic illustration of sample of an interconnected nanowire network prepared in the cylindrical pores of a track-etched PC membrane with thickness of 22 μm. The angle $\pm\theta$ with corresponding arrows indicates the four different pore directions in the template. d indicates the diameter of the nanowires. The electrodes illustrated are the remaining Cu/Cr film after selective removal of the middle part to prepare for transport measurements.

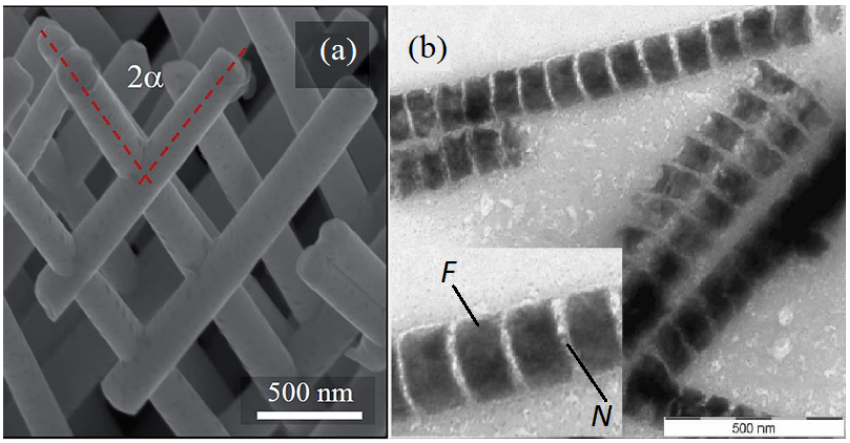

Figure 1.17: (a) SEM image of an interconnected nanowire network. 2α here represents the angle between the nanowires (b) TEM image of multilayered nanowires, where F and N indicate the ferromagnetic and nonmagnetic layers, respectively. Adapted from (a) [41], (b) [17].

noble metal cathode layer. From an electrolytic solution containing metal ions, various metals can be grown as nanowires in the track-etched pores of the template by electrochemical deposition.

Electrodeposition of metals is a process where metallic cations from an electrolyte is reduced to form a solid in the cathode (working electrode) of a cell, according to [42]:

$$M^{n+} + ne^- \rightleftharpoons M, \tag{1.56}$$

where n is the number of electrons. This reaction is characterised by the equilibrium potential E^{eq} given by the Nernst equation:

$$E^{eq} = E^0 + \frac{RT}{nF} \ln \frac{a_{M^{n+}}}{a_M}, \tag{1.57}$$

where E^0 is the normal electrode potential, R is the ideal gas constant, T is the absolute temperature, F is the Faraday constant, and a_M^{n+} and a_M is the activities of the metallic ions and atoms. E^0 for the metals and ions relevant for this work is presented in Table 1.4. To effectively electrodeposit the metals, an overpotential μ must be applied. This modifies Equation 1.57 by

$$E^{dep} = E^{eq} + \mu. \tag{1.58}$$

The deposited mass m that is deposited is given by Faraday's law:

$$m = \frac{M_M}{nF} \int_0^{t_{tot}} I(t)dt, \tag{1.59}$$

where M_M is the molar mass of the metal deposited, $I(t)$ is the cathode current flowing through the electrochemical cell, and t_{tot} is the total time of the process. Equation 1.59 represents a

Table 1.4: The normal electrode potentials E^0 of the metal/ion couples of Cu, Ni and Co. Adapted from [14], page 22.

Metal/ion couple	E^0**(V)**
Copper/Cu^{2+}	0.34
Nickel/Ni^{2+}	-0.26
Cobalt/Co^{2+}	-0.28

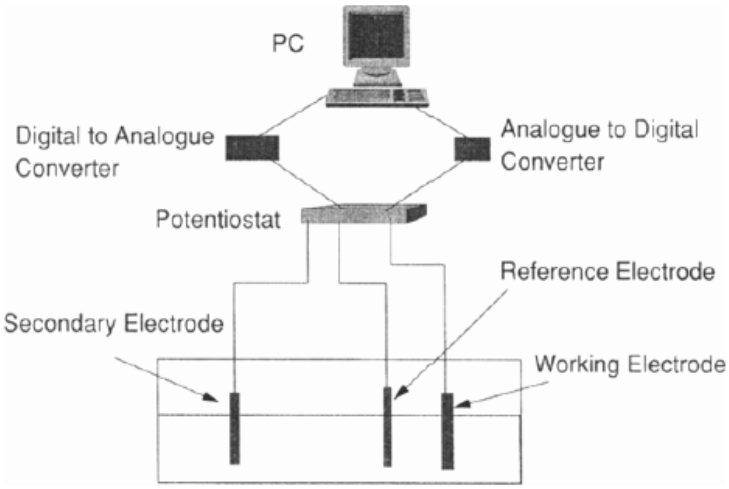

Figure 1.18: Schematic diagram of apparatus used for electrodeposition. Copied from [20].

deposition process where all the current goes to deposit the desired metal. In reality there will be undesired reactions, such as hydrogen evolution, which decrease the reaction efficiency η_M [14].

In potentiostatic electrodeposition the potential of the working electrode is measured against a reference electrode. The potential can be controlled by a potentiostat, and the cathode current is continuously measured. A schematic illustration of an electrodeposition setup is provided in Figure 1.18. Via the crystal structure and density of the deposited metal, and the total pore area, the thickness, t in nm, of the nanowire segment can be calculated through [43]:

$$t = c\frac{\eta_M Q_M}{A}, \tag{1.60}$$

where c is a constant related to the deposited metal, Q_M is the total charge in mC, and A is the available cathode surface area, in mm^2.

Several studies on multilayered nanowire arrays have earlier been produced through electrodeposition from single electrolyte baths, such as NiCoCu/Cu [10, 20] and Co/Cu systems [9]. By keeping the potential constant, arrays of continuous nanowires can be deposited, and by alternating the potential in pulses between two suitable values, multilayers can be produced. As mentioned earlier, an overpotential ensures effective deposition, but it also influence the kinetics of the deposition. It can an impact on the microstructure, alloy composition and grain size of the deposited metal. Electrodeposition of multilayers from a single electrolyte bath possible and practical, but a problem related to the process is the pollution by the nobler metal in the less noble metal. This arises because the nobler metal requires a less negative deposition potential than the other metal. The potential of the pulse for deposition of the other metal will then also deposit the nobler metal. This causes multilayered systems, deposited from an electrolytic bath containing Ni, Co and Cu ions, to contain Cu impurities in the ferromagnetic NiCo layer. Thus the layer composition will be written NiCoCu, although the Cu concentration in the layer will be low. In general, this is a reason for keeping the Cu^{2+} concentration low in the electrolyte, when depositing multilayers with Cu as the N layer. Another issue with pulsed electrodeposition of multilayers, is the tendency of dissolution of the less noble metal when the potential switches to the less negative potential. This is especially an issue for electrodeposition of CoCu/Cu multilayers.

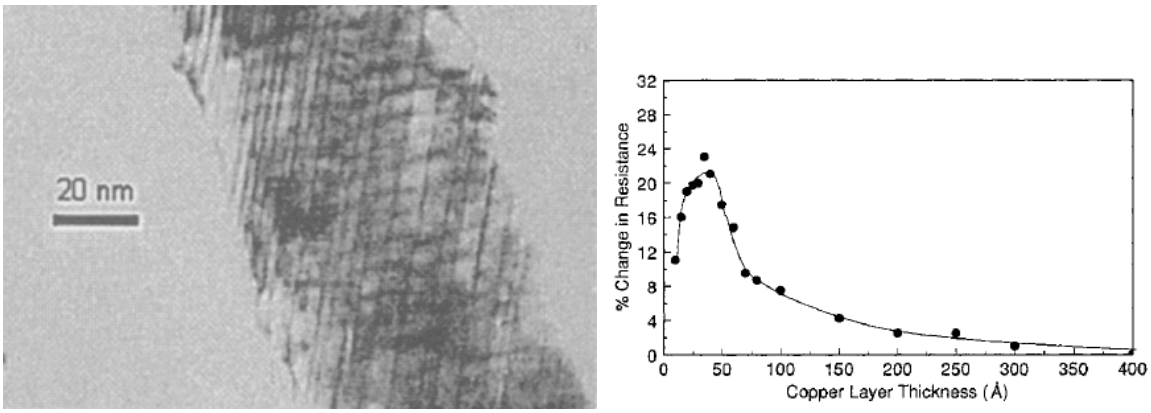

(a) (b)

Figure 1.19: (a) TEM image of a NiCoCu/Cu multilayered nanowire of 80 nm. (b) GMR (change of resistance) [%] for samples of different t_{Cu}. Adapted from [20].

Electrodeposited multilayered nanowires of Ni, Co and Cu

Multilayered magnetic nanowires made from CoCu/Cu have been studied in terms of the GMR effect [9, 44, 45]. A problem with using Co in the ferromagnetic layer is that it has a tendency to dissolve during the electrodeposition of the Cu spacer layer at a lower negative potential. When Ni is added to the alloy it tends to reduce this problem, hence allowing better control of the layer thickness [20]. A record value of ∼55% of room temperature GMR and ∼115% GMR at 77 K has been reported for arrays of parallel NiCoCu/Cu nanowires electrodeposited in porous alumina templates [46]. These wires were of diameters around 300 nm and up to 60 μm of length, with NiCoCu layer thickness of 5.4 nm and Cu spacer layer thickness of around 2.1 nm. The same system electrodeposited in porous PC membranes only resulted in a GMR of 22% [47], possibly due to higher interface roughness in the PC templates, and the hydrophobic nature of PC [46]. Figure 1.19a shows a transmission electron microscopy (TEM) image of a NiCoCu/Cu nanowire of 80 nm diameter. The lines perpendicular to the wire axis is the multilayers, and the nearly vertical lines are a signature of twinning in the lattice [20]. Moreover, studies on marallel NiCoCu/Cu multilayered nanowires in alumina membranes have been investigated within the framework of the VF model [10]. Series of samples with fixed NiCoCu layer and increasing Cu spacer layer, and vice versa, were investigated in order to find l_{sf}^F, l_{sf}^N, β and γ. l_{sf}^F was approximated to lie between 10 and 34 nm, l_{sf} was shown to be larger than 42 nm, and from this β was determined to be less than 0.37, and γ to be greater than 0.76.

The composition of the deposited ferromagnetic alloy is important in terms of the magnetotransport properties. As mentioned in Section 1.1.3, the magnetocrystalline anisotropy can be neglected in pure NiCo alloys with sufficiently high Ni concentration. For a certain Ni concentration the favoured crystal structure changes from hcp to fcc, which exhibits very low MC anisotropy. As was shown in Figure 1.4 this change occurs around 50% Ni.

The composition of the deposited alloy depends strongly on the deposition potential. Figure 1.20a shows the linear dependence between the Co concentration in electrodeposited continuous NiCo nanowires in alumina templates [48]. It shows that the Ni concentration in the deposited alloy increases linearly with increasing negative potential. Similarly, the growth rate also increases linearly with increasing negative potential, and a higher lattice defect concentration can be expected with increasing negative potential. Changing the metal ion concentration in the electrolyte will affect E^{eq} in Equation 1.57. Thus an increase in Ni^{2+} concentration in the electrolyte should shift the Co concentration curve in Figure 1.20a to the right.

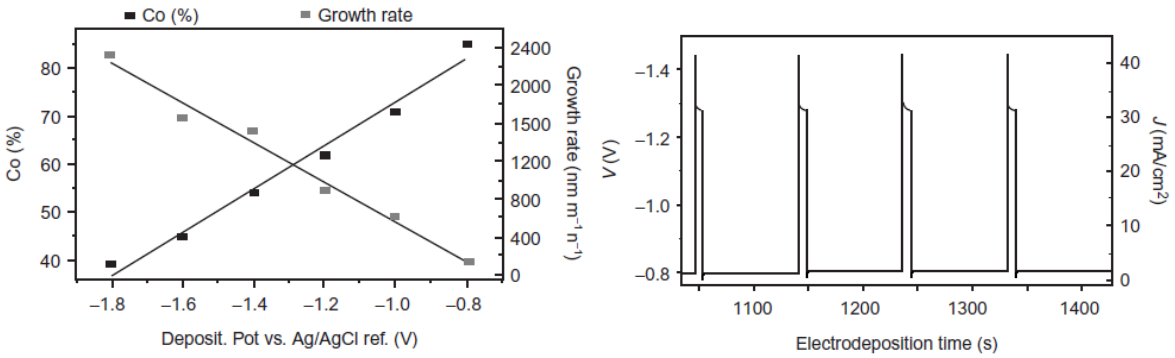

(a) (b)

Figure 1.20: (a) The Co concentration and growth rate of NiCo as a function of deposition potential. (b) Electrodeposition curve from deposition of NiCoCu/Cu ML NWs showing the potential and cathode current density as a function of time. Adapted from [14], page 87.

As mentioned earlier, the approach to deposit multilayered nanowires is to use single electrolytic baths containing all the desired metal ions. A noble metal, such as Cu, is suitable for the N layer because it deposits at a low negative potential compared to Ni and Co. However, Cu will also be deposited with the Ni and Co, to NiCoCu, during the more negative potential pulse, and this can affect the magnetic properties of the F layer. Thus, some Cu contamination in the F layer is inevitable, but can be kept at a minimum by keeping the Cu^{2+} concentration in the electrolyte at a minimum. However it has been observed that a few percent of Cu in solid solution in NiCo can push the material to favour a fcc arrangement. Recent studies have shown that NiCoCu with a relative composition of ∼55% Co and ∼45% Ni, deposits with fcc crystal structure in the (111) direction along the nanowire axis [10]. Note that Ni and Co pollution in the Cu layer can occur in the form of paramagnetic defects. This can affect the magnetotransport properties by increasing the spin-flip exchange scattering on the paramagnetic defects, as discussed in Section 1.2.2.

In terms of magnetotransport, Figure 1.19b shows how the GMR varies in samples with fixed NiCoCu layer thickness of 5.0 nm, and different Cu spacer layer thicknesses, which peaks at around 22% for t_{Cu} around 4 nm. For samples with Cu layers thicker than this, the GMR decreases, as predicted by the VF theory. For thinner Cu layers the GMR is destroyed by ferromagnetic coupling between the NiCoCu layers arising from defects [20].

The effect of crossing zones

A unique feature about the interconnected nanowire network, is the existence of crossing zones created when to nanowires grows into each other. As interconnected networks of multilayered nanowires is a novel system, the effects of the crossing zones are yet unknown. Predicting the metal growth in these crossing zones is a complicated task, and it seems unlikely that the well-defined complete layers required for GMR effect will exist there. This would require the nanowires in to meeting pores to meet simultaneously in the crossing zone, and because the pore diameters can vary, this seems very unlikely to happen. Instead it can be assumed that the structure inside the crossing zones is rather random, and that the effect on the GMR effect is none in the best scenario, but presumably a zone which contributes with spin-independent resistance that increases the total resistance, and thus indirectly reduces the observed GMR effect.

In continuous interconnected nanowire networks the crossing zones contain magnetic domains. These domains influence the magnetisation reversal properties of the nanowire network. If a

magnetic field corresponding to an energy barrier preventing the domain from moving is applied, the domain can start to propagate out of the crossing zones and into the nanowires. This effect has not been studied for interconnected multilayered nanowire networks, but it must be expected that it can occur. By reducing the number of crossing zones in the nanowire networks, this effect can be addressed. This can be done by reducing the porosity in the templates used for the synthesis of the nanowire networks.

Summary of Chapter 1

This chapter has outlined the fundamental mechanisms contributing to the magnetoresistance effect in interconnected multilayered nanowire networks. The intrinsic magnetic and magnetotransport properties of ferromagnets, combined with the extrinsic effect created using a nonmagnetic spacer layer, were the necessary tools to explain the giant magnetoresistance effect. Furthermore, the fundamental mechanisms governing CPP-GMR were outlined within the framework of the Valet-Fert model. Moreover, the basics of electrochemical deposition and its suitability for fabrication nanowires were explained. A closer look were given to the details concerning electrodeposition of Ni, Co and Cu, as these metals exhibit properties which are interesting for use in multilayered nanowires, such as high magnetic moment and high AMR. For simplicity, GMR will in most cases be used instead of MR, for the rest of this work. However, it would be more correct to refer to the MR as it contains the sum of the contributions from the AMR and the GMR. Since, the GMR is so much larger than the AMR, the author has decided to refer to GMR in the place of MR.

Chapter 2

Fabrication and characterisation of interconnected multilayered nanowire networks

The overall goal of this thesis has been optimise the the fabrication process for interconnected NiCoCu/Cu multilayered nanowire networks, to achieve as high CPP-GMR as possible. This was done by first finding the optimised deposition potentials, and the optimal deposition time for the NiCoCu and Cu layers, before making series of samples with different Cu layer deposition time, to find the optimal value for this parameter. Characterisation involved morphology and composition investigations, in addition to magnetic characterisation and magnetotransport measurements, which were performed on all samples in order to identify the GMR effect. Continuous NiCoCu samples were created and characterised for different templates and with different electrolytes for comparison.

2.1 Synthesis of interconnected multilayered nanowires

Interconnected multilayered (ML) nanowire (NW) networks were prepared using electrodeposition from an electrolyte according to a previously reported procedure [10]. The samples were prepared in track-etched polycarbonate (PC) membrane templates, with a template thickness of 22 μm. The track-etching process was carried out with ion bombardment from an angle of $25° \pm 5°$ relative to the perpendicular-to-plane direction, from four different in-plane directions: 0°, 90°, 180°, and 270°, as shown in Figure 1.16 and 2.1. Thus, after etching with NaOH the template was left with cylindrical shaped arrays of interconnected pores, with diameters corresponding to the etching conditions [40]. Templates with pore diameters of 40, 80 and 105 nm, and with various pore packing densities, were used for this thesis. At a later stage one side of the PC templates were coated with a metallic Cu/Cr film to serve as a cathode during the electrodeposition process. This metal film was deposited through electron-beam evaporation using a Pfeiffer Vacuum Classic 500 instrument. The cathode layer was deposited to cover the pores, which required a minimum cathode thickness of three times the nanowire diameter.

The nanowires were deposited electrochemically from electrolytic solutions containing different concentrations of Ni, Co and Cu, as reported in detail below. This process produces interconnected nanowire networks either with alternating layers of different metals or alloys, multilayers, or as continuous nanowires. For the multilayered case the deposition direction of the layers can be imagined as vertical, perpendicular to the pore direction, or something in between. This is illustrated in Figure 2.2. As explained in Section 1.3, these metals deposit at different negative potentials. Thus, multilayered nanowires could be grown through a sequence of potential pulses. The electric pulses were generated and monitored by a EG&G Princeton Applied Research Po-

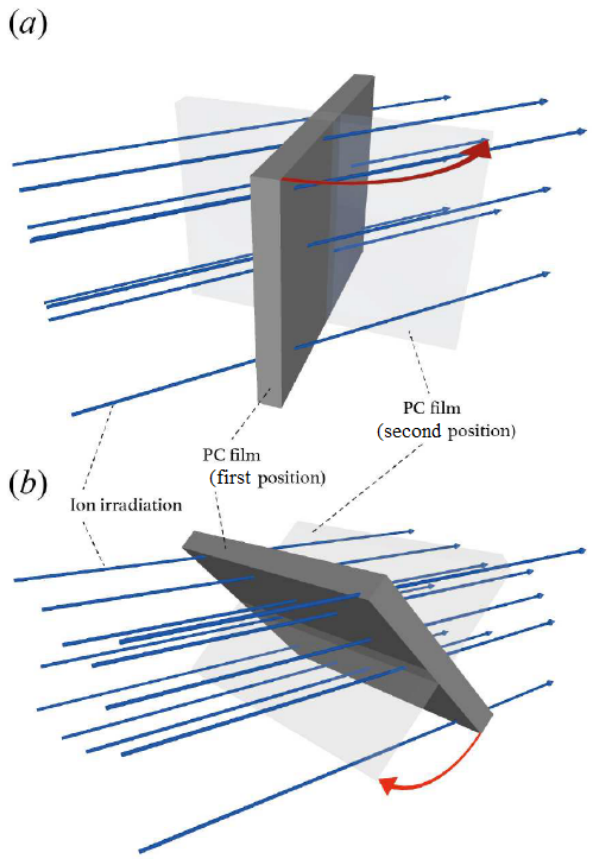

Figure 2.1: Schematical illustration of the track-etching process. (a) shows the irradiation steps of ±25° relative to the the out-of-plane direction, while (b) shows the irradiation steps of ±25° relative to the the out-of-plane direction after a 90° in-plane rotation of the PC membrane. Adapted from [3].

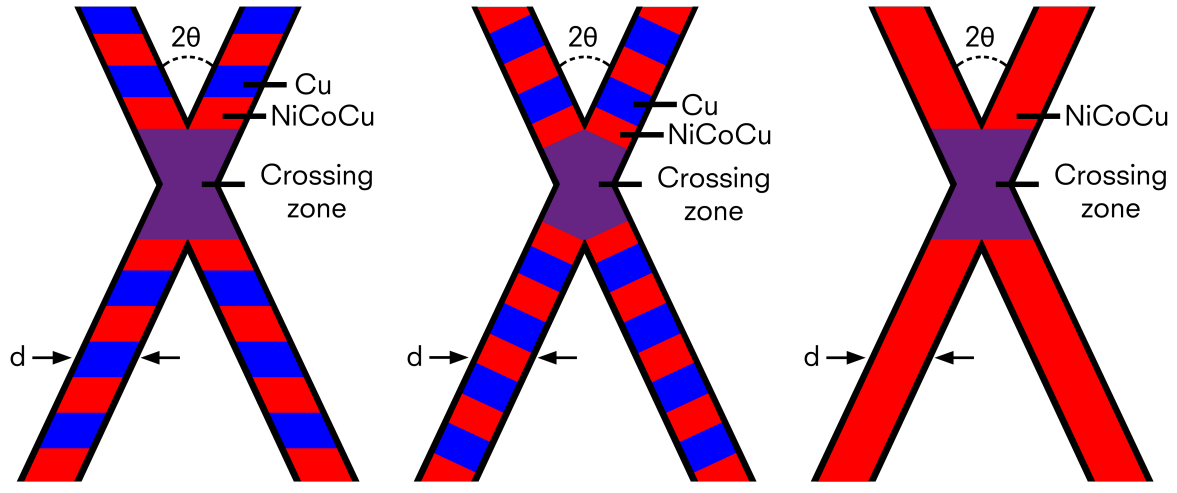

(a) (b) (c)

Figure 2.2: Schematic illustration of two nanowires with a relative angle of 2θ and diameter d which have grown together. (a) and (b) represent multilayers of NiCoCu/Cu in two possible layer growth directions. (c) depicts a continuous NiCoCu nanowire. The crossing zones of unknown magnetic properties are marked in purple.

(a) (b)

Figure 2.3: (a) Picture of both sides of the round samples, (right) showing the cathode layer facing upwards, and (right) showing the deposited nanowires as the black spot. The metallic dots are nanowires which have overfilled the template. (b) Picture of rectangle shaped samples. To the left is a template after deposition of nanowires (black area). In the middle is a template before deposition and to the right is a template with the cathode layer facing upwards.

tentiostat/Galvanostat Model 263 and accompanying software. Series of samples with deposition parameters differing in pulse time and potential, were prepared for magnetotransport measurements, in order to optimise the parameters for GMR, according to the theoretical explanation given in Section 1.2.4 and 1.3.

The electrodeposition was carried out in home-made teflon cells where the template was exposed to the electrolyte. The process was carried out in normal temperature and pressure. A Pt strip was used as counter electrode, and the potential on the working electrode on the sample was measured relative to a Ag/AgCl reference electrode of the model Hamilton MiniTrode. A similar setup is schematically illustrated in Figure 1.18.

Initially, circular shaped samples were fabricated, with a diameter of ∼6 mm, as shown in Figure 2.3a. However, it was hard to selectively remove the metallic cathode film to prepare the samples for transport measurements. To remove parts of the cathode normal scotch tape was used to stick to the metal side of the sample. When tearing off the tape, small parts of the cathode were sometimes torn off with the tape, leaving open areas in the cathode film. This only worked occasionally, and the process often destroyed the mechanically fragile samples. In an attempt to reduce the adhesion of the cathode film, a new template was metallised with Cu only, and the adhesive Cr layer was left out. This made the "scotch tape process" more reliable, but the lower adhesion between template and cathode film prevented good and homogeneous deposition. It was then decided to change the method of cathode removal to plasma etching. From this point and throughout, all the samples for this work were deposited with the shape of elongated rectangles with an area of approximately 3×24 mm, as this was suitable for plasma etching. These samples are shown in Figure 2.3b. The experimental details concerning plasma etching are reported in Section 2.4.1 below.

2.1.1 Optimisation of electrodeposition parameters

To achieve samples with optimised GMR, a systematical approach to optimise the electrodeposition parameters by changing one parameter at a time, was performed. As a starting point, the potential parameters used in a study of NiCoCu/Cu nanowires grown parallel in porous alumina templates were used [10]. These were -1.0 V for the NiCoCu layer and -0.2 V for the Cu layer, defined as V_F and V_N respectively. As mentioned in Section 1.3, V_N should be kept low to limit the defect concentration in the deposited Cu, but at the same time not too low, in order to prevent dissolution of the magnetic layer. Each deposition were performed by repeated cycles

of pulses of V_F and V_N, where each cycle deposited one bilayer consisting of a NiCoCu and a Cu layer. The individual pulse times of the NiCoCu and Cu layers were varied for the different samples in order to grow samples with different layer thicknesses.

As described, the electrodeposition was performed under time and potential control, not with control of the deposited charge, which has been done in earlier studies [1, 43, 10]. The reason for this, was a problem with the computer that calculated the deposition current. Since the order of magnitudes of the deposition currents of the NiCoCu and Cu layers were of different magnitudes, there was a problem with the scaling, resulting in untrue current values. This was evident because the current corresponding to the pulse of the NiCoCu layer could be around 4 mA while the pulse of the Cu layer had slightly negative currents, indicating dissolution of the metal. The later observed GMR effect of these samples proved that the Cu layer must have been deposited, and hence the values of the measured deposition currents could not be trusted. Additionally, the deposition current of the Cu pulse was clearly positive when the scale was changed down, but then the NiCoCu pulse current was too high to be measured. This discovery lead to a change of the optimisation strategy: instead of controlling thicknesses of the layers, from the deposited charge using Faraday's law, the pulse times and potentials where used as control parameters.

To try and determine the layer thicknesses from the time of each pulse, an attempt to find a deposition rate for each layer was done. Samples were electrodeposited with V_F and V_N, and different layer pulse times until overfilling, in templates with high pore packing density of 20% and pore diameter of 40 nm. The overfilling could be seen on the deposition curve as an increase in the deposition current. The time corresponding to the start of the current increase T_{of} was used to calculate the number of bilayers n_{bl} deposited through

$$n_{bl} = \frac{T_{of}}{T_F + T_N}, \tag{2.1}$$

where T_F and T_N are the times of the NiCoCu and Cu pulses respectively. Then the thickness of one bilayer t_{bl} could be calculated, as it was known that the total thickness of the nanowire is related the thickness of the membrane, 22 μm/ $\cos(25°) = 24.3$ μm, at the moment overfilling starts:

$$t_{bl} = \frac{24.3\mu m}{n_{bl}}. \tag{2.2}$$

When this was done for two samples with different T_F and T_N, the deposition rates $r_F = t_F/T_F$ and $r_N = t_N/T_N$, corresponding to the NiCoCu and the Cu layer respectively, could be found through a set of equations as follows:

$$r_F T_{F,1} + r_N T_{N,1} = t_{bl,1}$$

$$r_F T_{F,2} + r_N T_{N,2} = t_{bl,2}$$

which is a set of two equations with two unknowns, that can be solved. While this was possible in theory, it was hard in practice and led to inconsistent results, for two reasons: the first was the difficulty of identifying the exact time for the start of overfilling, because the membrane porosity is large and not all the pores starts to overfill at the same time. The current only increased slightly so the uncertainty in T_{of} was as large as ∼1000 seconds, for an electrodeposition of around 8000 seconds in total. Secondly, the method would only work as long as the deposition rate is constant, but this could not have been the case as the deposition current were not constant during the entire pulse. Especially for the V_F pulse this was clearly the case, as shown in Figure 2.4. The current stabilises at a constant value after some time, but the short V_F pulses are obviously too short for this to happen. The assumptions leading to the presented model are thus not good. Still, this calibration method lead to an estimation of 300 milliseconds for the NiCoCu layer pulses, and 8 second pulses for the Cu layers.

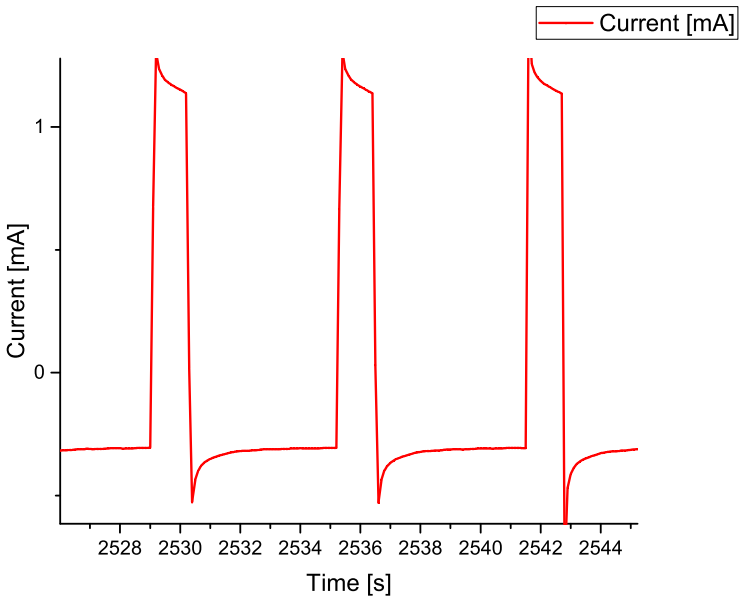

Figure 2.4: Section of the cathode current as a function of time for the deposition of a multilayered nanowire sample. The pulses with high(low) current correspond to $V_F(V_N)$.

Electrolyte composition

The electrolytes were prepared from solid metal sulfate hydroxides diluted in water to obtain a sulfate bath with the following concentrations: 2.3 M $NiSO_4{\cdot}6H_2O$, 0.4 M $CoSO_4{\cdot}7H_2O$, 25/15/5 mM $CuSO_4{\cdot}5H_2O$, and 0.49 M H_3BO_3. The three different copper sulfate concentrations corresponds to three different electrolytes with different Cu molarities. By adding concentrated H_2SO_4, the solutions were all brought to a pH between 2.0 and 2.1 to favour a fcc crystal structure of the NiCoCu layer, and to increase the solubility. The Ni concentration is larger than the Co concentration by almost a factor of six to balance out the difference in the deposition rates of the two metals. As explained in Section 1.3, Co deposits at a less negative potential than Ni. This ratio of concentrations is expected to yield a NiCoCu alloy composition with almost equal amounts of Ni and Co, and low Cu concentration [10].

Because all three metals will be deposited at -1.0 V, the Cu concentration is kept very low to reduce the Cu deposition in the NiCoCu layer, and limit the deposition rate by diffusion [1]. This way the Cu concentration in the NiCoCu layer can be limited to only a few percent of the overall layer composition. However, the low Cu concentration makes the deposition rate of Cu at V_N very low, hence very long pulses are required for this layer.

As the electrolytes were close to saturation in terms of Ni concentration, they were not completely stable. Precipitation occurred days after preparation, and stirring combined with careful heating were necessary to dissolve the precipitate. Precipitate in the electrolyte posed the danger of sticking to the template surface during electrodeposition, thus blocking pores and potentially prevent good and homogeneous deposition on the entire sample area. Precipitation also changes the relative concentrations in the electrolyte, and an electrolyte that is changing during the deposition is not good for reproducible fabrication.

Potentiostat parameters

As discussed in Section 1.1.4, the desired layer thicknesses for both the NiCoCu and Cu layers are such that the sample becomes more or less magnetically isotropic, by fulfilling the critierion illustrated in Figure 1.7. A previously reported method to control the thicknesses of the deposited layers, has been to use a computer to continuously integrate the current to obtain the charge deposited in each layer [43]. Unfortunately, this method is not possible with the setup in use, due to the software problem mentioned above.

The pulse potentials V_F and V_N where chosen based on an earlier report on NiCoCu/Cu multilayered nanowires [10]. The NiCoCu layer deposited well at -1.0 V and no optimisation of this parameter was necessary. To optimise V_N, a series of samples with 1000 bilayers was prepared. V_N was set to -0.2 V for the first sample, but this yielded only and AMR contribution to the MR. Thus V_N was changed to -0.4 V to prevent dissolution of the NiCoCu layer when depositing Cu. -0.4 V was eventually found to work well. The series of samples prepared was labeled *'V_N 25 mM'*, and the experimental parameters are collected in Table 2.1 below:

Table 2.1: Electrodeposition parameters of the *'V_N 25 mM'* series, to optimise V_N.

Series name	Diameter [nm]	Porosity [%]	Electrolyte (Ni/Co/Cu) [mol/L]	V_F	V_N	T_F	T_N
V_N 25mM	40	20	2.3/0.4/0.025	-1.0 V	-0.4 - -0.2 V	300 ms	8 s

To establish the optimal deposition time of the NiCoCu layers, samples where prepared from a NiCoCu electrolyte, with 25 mM Cu^{2+} concentration, with alternating pulses of $V_F = -1.0$ V and $V_N = -0.4$ V, where the latter pulse time was kept constant at 8 seconds, and the former pulse time was varied between 200 and 1000 milliseconds, for the different samples. It occurred problems with overfilling for this series of samples, when the deposition time of the V_F pulse was increased. Therefore, the number of bilayers was reduced from 1000 to 600. 600 bilayers were used for all remaining sampler in the thesis unless stated otherwise. This sample series was labeled *'F 25 mM'*, and the experimental parameters are summarised in Table 2.2 below. Later the GMR of the samples were identified through magnetotransport measurements, and 300 milliseconds was found to be the optimal deposition time of the V_F pulse.

Table 2.2: Electrodeposition parameters of the *'F 25 mM'* series, to optimise the deposition time of the NiCoCu layer pulse.

Series name	Diameter [nm]	Porosity [%]	Electrolyte (Ni/Co/Cu) [mol/L]	V_F	V_N	T_F	T_N
F 25mM	40	20	2.3/0.4/0.025	-1.0 V	-0.4 V	200 - 1000 ms	8 s

Once the optimal deposition time of the V_F pulse was identified, the optimal Cu deposition time was identified in a similar way. With the V_F pulse time kept constant at the optimal value of 300 milliseconds, the V_N pulse time was varied between 4 and 20 seconds. This sample series was labeled *'N 25 mM'*, and the parameters are summarised in Table 2.3 below. Subsequent investigation of the GMR value of the samples were used to identify the optimal Cu deposition time.

Table 2.3: Electrodeposition parameters of the *'N 25 mM'* series, to optimise the deposition time of the Cu layer pulse.

Series name	Diameter [nm]	Porosity [%]	Electrolyte (Ni/Co/Cu) [mol/L]	V_F	V_N	T_F	T_N
N 25mM	40	20	2.3/0.4/0.025	-1.0 V	-0.4 V	300 ms	4 - 20 s

To investigate the influence of Cu concentration, electrolytes containing less Cu, 5 and 15 mM respectively, were used to prepare two sample series. The Cu pulse time was varied between 10 and 20 seconds, in different samples, and the series were labeled *'20%600 5 mM'* and *'20%600 15 mM'*, corresponding to the different Cu concentration in the electrolytes. Table 2.4 collects the deposition parameters. Decreasing defect concentration in the Cu layer is expected with decreasing Cu concentration, but the growth rate will also decrease. The samples underwent magnetotransport measurements to identify the optimal Cu layer deposition time. Through these measurements it was discovered that a Cu concentration of 15 mM offered the best compromise between growth rate and defect concentration, so this concentration was used throughout the rest of the work.

Table 2.4: Electrodeposition parameters of the *'20%600 5 mM'* and *'20%600 15 mM'* series, prepared to investigate the influence of the Cu concentration in the electrolyte.

Series name	Diameter [nm]	Porosity [%]	Electrolyte (Ni/Co/Cu) [mol/L]	V_F	V_N	T_F	T_N
20%600 5mM	40	20	2.3/0.4/0.005	-1.0 V	-0.4 V	300 ms	10 - 20 s
20%600 15mM	40	20	2.3/0.4/0.015	-1.0 V	-0.4 V	300 ms	10 - 20 s

2.1.2 Low-porosity sample fabrication

The crossing sections of the nanowires are zones where it is hard to predict the magnetic properties, especially for multilayers. However, the crossing zones are expected to somehow contribute to lower GMR, as mentioned in Section 1.3. To minimise the effect from the crossing zones, templates with a minimum amount of crossing zones were used. The minimum amount of crossing points were calculated to ensure a self-supporting interconnected nanowire network. This also results in a minimum pore packing density.

The two templates used were similar to the previous template in the way that the relative angles with the planes were the same. This means 20-25° relative to the out-of-plane direction, from four different in-plane directions with a 90° angle between them. One template contained pores with diameters of 40 nm, resulting in a porosity of 2%. The other template had the similar minimum pore packing density, but the pore diameter was increased to 80 nm, resulting in a porosity of 8%. Note that the two templates contained almost the same density of crossing points.

Series of samples from the two low-porosity templates were prepared with the optimised deposition parameters, as reported in Table 2.5 below. These sample series were labeled *'2%600'* and *'8%600'*. The Cu layer deposition time was varied around the optimum values found from previous sample series, that is between 12 and 16 seconds. Subsequent magnetotransport measurements were carried out to obtain the GMR of the samples.

Table 2.5: Electrodeposition parameters of the 2%600 and 8%600 series, prepared to investigate the influence of the reduced amount of crossing zones.

Series name	Diameter [nm]	Porosity [%]	Electrolyte (Ni/Co/Cu) [mol/L]	V_F	V_N	T_F	T_N
2%600	40	2	2.3/0.4/0.015	-1.0 V	-0.4 V	300 ms	12 - 16 s
8%600	80	8	2.3/0.4/0.015	-1.0 V	-0.4 V	300 ms	12 - 16 s

Challenges of low-porosity sample fabrication

Several experimental challenges were connected to the preparation and subsequent measurements of the low-porosity samples. In fact, one electrodeposition led to very high GMR values, but the result was not reproducible. A lot of work was put into trying to reproduce the good sample,

which was electrodeposited in the 80 nm template with $V_F = -1.0$ V for 300 milliseconds and $V_N = -0.4$ V for 12 seconds, and labeled 8%601A and B. In other words, the sample from one electrodeposition was cut in two pieces, A and B, which were measured individually. As will be shown in Section 3.2.1, both of these samples showed very high GMR values. Around 30 samples of the *'2%600'* and *'8%600'* series were fabricated and measured in the attempts to reproduce the two good samples, without reaching GMR values of more than a few percent at best. Many of the samples showed almost no conductivity at all. These challenges were so severe that it is doubtful if these templates are suitable for magnetotransport studies. Additionally, overfilling of the samples were observed much earlier than expected for many samples; especially in the *'8%600'* series. Several adjustments to the electrodeposition process were tested out in this process.

Initially, the electrolyte was believed to be the problem. It became unstable and formed an extensive amount of precipitate a while after it was prepared. This was a problem during electrodeposition as precipitate formed inside the cell, attaching to the template and causing heterogeneous deposition. This could also be a reason for the premature overfilling. The samples prepared under these circumstances were visually clearly heterogeneous. It was assumed that the electrolytic solution was saturated with Ni and was thus unstable. In attempts to keep the electrolyte stable during the electrodeposition, it was carefully heated and stirred until all precipitate had dissolved. Then the electrodeposition could be carried out. This method worked well for a while and homogeneous samples were successfully fabricated, although overfilling still occurred. However, this improvement showed no effect at all on the transport properties.

After this it the possibilities of problems with the instruments or the software were investigated. A conducting metal plate which connected the cathode on the sample to the potentiostat during electrodeposition was replaced. This to eliminate the possibility that oxidation on this plate led to poor contact between the cathode and the plate. This could lead to heterogeneous electrodeposition, hence the possibility of areas in the sample where the nanowires were not connected. This change improved the features of the electrodeposition curve, which looked slightly cleaner, but it did not seem to influence the visual appearance of the samples, nor the transport properties.

However, some of the input parameters used in the software that controls the electrodeposition were found to be wrong. This involved the parameters that controlled the way the potentiostat controls the pulses, and not the parameters V_F, V_N and the NiCoCu and Cu pulse times. The Ag/AgCl reference electrode were also replaced with a newer model. These corrections improved both the visual appearance and the deposition curves, which looked more similar to those belonging to the good *'20%600 15 mM'* series, which was fabricated with the correct software settings. Unfortunately, there was still no improvement in the transport properties, which actually seemed completely unaffected the modifications to the fabrication process. No further ways to improve the electrodeposition process could be identified, and this indicated that a later step in the fabrication process had to be the problem. To make sure that the fabrication line still worked, another sample using the 20% 40 nm template were prepared. This yielded a sample with higher GMR that earlier. This showed that the adjustments to the deposition process might have yielded some improvements after all.

The plasma etching process might indeed have caused the problem. Apart from the samples prepared from the 20% 40 nm template, all samples requires etching time of 38 minutes, or longer, as reported in Table 2.11. The samples becomes heated by the plasma during this process. This is evident because the instrument frequently shuts down due to overheating during the longest plasma etching processes. Since the PC membrane has a very different thermal expansion coefficient than the metal nanowires, the heating might possibly tear the nanowire network apart. This can explain why many samples show resistance of the order of several hundreds of kΩ after

plasma etching.

Additionally, the samples are very sensitive to the plasma etching time. It is important to remove all the Cu/Cr, otherwise the remaining metal will create additional current channels with low resistance, which will decrease the measured MR. Unfortunately, too long exposure to the plasma can completely destroy the nanowire network, leaving the sample useless. Exposure times differing as little as one minute has resulted in one sample being unfinished, and the other one destroyed. This shows that the samples are very sensitive to the etching time. In order to not expose the samples for too long, many samples might have been etched to short, leaving residues of the Cu/Cr thin film on the sample. The presence of this will be proven in Section 3.2.

It was noted that the the samples prepared from the 20% 40 nm template were reproducible, and worked well after plasma etching. The higher porosity will indeed give the samples higher mechanical strength to resist the thermal stresses induced by the PC membrane. However, the plasma etching time is shorter for these samples because the Cu/Cr layer is thinner. This will generate less heat and thus less thermal expansion during the etching process. In the light of this two possibilities might offer a solution for the low-porosity samples: the first is to perform the plasma etching in several steps, and let the samples cool down after each exposure. This to prevent to high temperature in the samples. This involves new calibration of the exposure time because the etching rate is not linear in the beginning of the process. The second possibility is to fabricate templates with thinner Cu/Cr cathode layer. If similar thickness as in the case of the 20% 40 nm template could be successfully prepared, the exposure time would decrease and so the temperature. These two possibilities have not been investigated due to the limited time of this thesis.

2.1.3 Fabrication of samples with increased NiCoCu layer thickness

To investigate the influence of the thickness of the NiCoCu layer, t_F, a series of samples with different t_F were prepared. The previous experiments had shown that the 20% porosity templates were the most reliable, for reasons that were just explained. Thus the template with 20% porosity and 40 nm pore diameter was used to make a series of samples with the optimised deposition parameters. Only the deposition time of the NiCoCu layer pulse was different from the optimised value. Samples were prepared using NiCoCu layer deposition time ranging between 300 milliseconds and 3 seconds. The Cu layer deposition time was kept constant at the optimised value of 14 seconds. The sample series was labeled *'F 20%'* and the deposition parameters are collected in Table 2.6 below. To prevent overfilling, the number of bilayers were decreased in line with increasing NiCoCu layer deposition time, according to Table 2.7. The number of bilayers were roughly estimated in order to keep the total nanowire lengths approximately the same in all the samples.

Table 2.6: Electrodeposition parameters of the *'F 20%'* series, prepared to investigate the influence of increased NiCoCu layer thickness.

Series name	**Diameter [nm]**	**Porosity [%]**	**Electrolyte (Ni/Co/Cu) [mol/L]**	V_F	V_N	T_F	T_N
F 20%	40	20	2.3/0.4/0.015	-1.0 V	-0.4 V	300 ms - 3 s	14 s

Table 2.7: Number of bilayers in the samples of different NiCoCu layer deposition time, of the F 20% series.

T_F	300 ms	600 ms	1000 ms	2000 ms	3000 ms
# bilayers	600	400	300	150	110

2.1.4 Fabrication of systems with lower saturation fields

As will be seen in Chapter 3 the multilayers have saturation fields which is higher than what is suitable for applications. There are two main strategies for decreasing the saturation fields of multilayered nanowires: multilayers with increased nanowire diameter to alter the aspect ratio to reduce the demagnetising field in the IP direction, or trilayer systems to reduce the dipole-dipole interactions between the layers.

Multilayered nanowire network with increased nanowire diameter

To decrease the demagnetising field in the IP direction, a multilayered nanowire network sample were prepared in a template with 105 nm pore diameter and high porosity. One electrodeposition with the parameters reported in Table 2.8 yielded a sample which was cut in two samples to be measured individually.

Table 2.8: Electrodeposition parameters of the multilayered nanowire network sample with nanowire diameter of 105 nm.

Series name	**Diameter [nm]**	**Porosity [%]**	**Electrolyte (Ni/Co/Cu) [mol/L]**	V_F	V_N	T_F	T_N
105 nm	105	<20	2.3/0.4/0.015	-1.0 V	-0.4 V	300 ms	14 s

Interconnected trilayer network

To decrease the effect of the dipolar coupling between the of NiCoCu layers, a sample of trilayers was prepared. The the trilayers were prepared with cycles of four pulses with the optimised parameters. The first three pulses were similar to those used in the 20%600 15mM series, while the fourth pulse was to deposit a thick Cu layer to separate the trilayers from each other. Earlier studies have used Cu layers of around 100 nm to separate the trilayers, in order to reduce the dipole-dipole interactions between the F layers in the same nanowire [43]. Thus it seemed reasonable to use pulses of 10 times the length compared to the normal separation layers. A total of 100 trilayer cycles were deposited in the sample. The deposition parameters and the trilayer cycle is reported in Table 2.9 and 2.10.

Table 2.9: Electrodeposition parameters of the trilayers sample, where s and l in T_N represents the deposition time of the Cu layer separating the NiCoCu layers or the Cu layer separating the trilayers, respectively.

Series name	**Diameter [nm]**	**Porosity [%]**	**Electrolyte (Ni/Co/Cu) [mol/L]**	V_F	V_N	T_F	T_N**(s)**	T_N**(l)**
Trilayers	40	20	2.3/0.4/0.015	-1.0 V	-0.4 V	300 ms	14 s	140 s

Table 2.10: Deposition time of the F, N and the separating Cu layer of the trilayers sample.

Layer	F	N	F	N (separation)
Dep. time	300 ms	14 s	300 ms	140 s

2.2 Characterisation of morphology and composition

The morphology of a selection of samples were investigated with a JEOL FEG SEM 7600F field-effect scanning electron microscope (FE-SEM), with a resolution of the order of 10 nm. The FE-SEM was equipped with a JEOL JSM2300 energy-dispersive X-ray spectroscopy (EDX) analysis system, with a resolution $<$ 129 eV. The FE-SEM was used to obtain pictures of the

interconnected nanowire networks, to be able to investigate the morphology of the samples. EDX analysis were performed to investigate the elemental composition of the samples.

Inside the FE-SEM the sample becomes exposed to a focused beam of accelerated electrons. The electrons interact with the mass in the sample through different mechanisms. The electrons penetrate the surface of the sample, and some electrons are scattered inelastically within the first nanometers of depth. These are called the secondary electrons and they can be picked up by a detector to give information about the morphology of the sample, resulting in pictures of the nanowire networks with nanometer resolution. The inelastic scattering can lead to excitations of valance electrons in the atoms inside the samples. X-rays are emitted when the electrons relax back to the ground state. The X-ray energy corresponds to the energy difference in the atomic energy levels, and are characteristic to the element. EDX analysis thus requires an X-ray detector to pick up the photons emitted from the sample. The frequencies of the X-rays detected give information about the present elements, and the relative intensities of the characteristic photon spectra of the elements present, can be used to obtain the composition of the sample.

The samples were prepared for these measurement by removing the cathode layer and the PC membrane, by dry and wet etching techniques, respectively. The cathode layer was removed by plasma etching, according to the process that will be described in Section 2.4.1 below. The PC membrane was chemically etched away using concentrated dichloromethane. The interconnected nanowire network samples were self-supporting after this treatment and could be moved to an adhesive carbon fibre film on top of a Si sample holder. Removal of the dielectric PC membrane is important, because its presence in a SEM measurement can lead to a build-up of charge in the remaining PC, which can affect the measurement. The cathode layer needs to be removed because it contains Cu which also is a constituent in the sample. Thus it can lead to overestimation of the Cu concentration in the samples, if it is not removed completely.

The FE-SEM measurements were performed with electrons accelerated to 15 keV with a working distance of 7-8 mm. The EDX measurements were carried out with a chemical spectra acquisition time of 100 seconds with a probe current of 1 nA, at different spots on each sample to reveal possible heterogeneities in the elemental composition of the sample. Quantitative elemental analysis were then performed with the integrated software.

2.3 Characterisation of magnetic properties

Magnetic measurements were performed by a MicroMag 2900 alternating gradient field magnetometer (AGFM) from Princeton Measurements Corporation, to obtain the magnetisation hysteresis curves at room temperature [49]. The instrument is shown in Figure 2.5. Initially, the instrument was calibrated with a spherical ferromagnetic calibration sample with a known magnetisation of 76.20 emu, and zero hysteresis. Then a small piece of the sample were cut and placed on a glass plate support on the sample holder, before it was loaded into the instrument between two electromagnets. The electromagnet induce a uniform horisontal static magnetic field H of maximum 14 kOe, as shown in Figure 2.6a. The field magnetises the sample, which thus creates its own magnetic field. Then gradient coils generate an alternating field that interacts with the field of the sample, causing a displacement of the sample alternatively left and right, as illustrated in Figure 2.6b. The displacement is proportional to the magnetic moment of the sample. The displacement is measured by a piezoelectric sensor attached to the sample holder that converts the mechanical force into an AC voltage, as shown in Figure 2.6c. This measurement is recorded and the data can be analysed by computer software.

Before the magnetisation measurement, the sample was demagnetised a programmed procedure

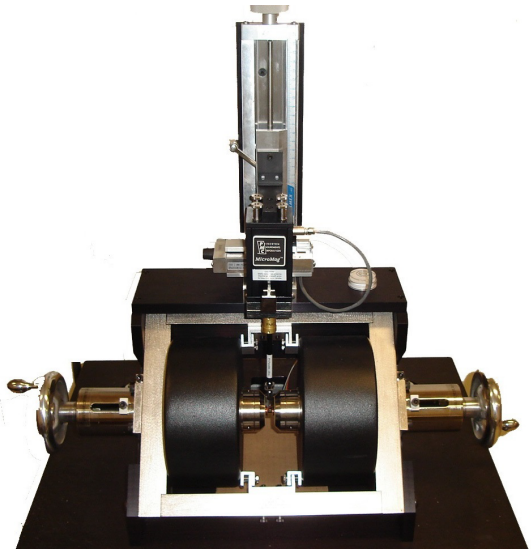

Figure 2.5: An AGFM intrument similar to the one used in this work. Copied from [50].

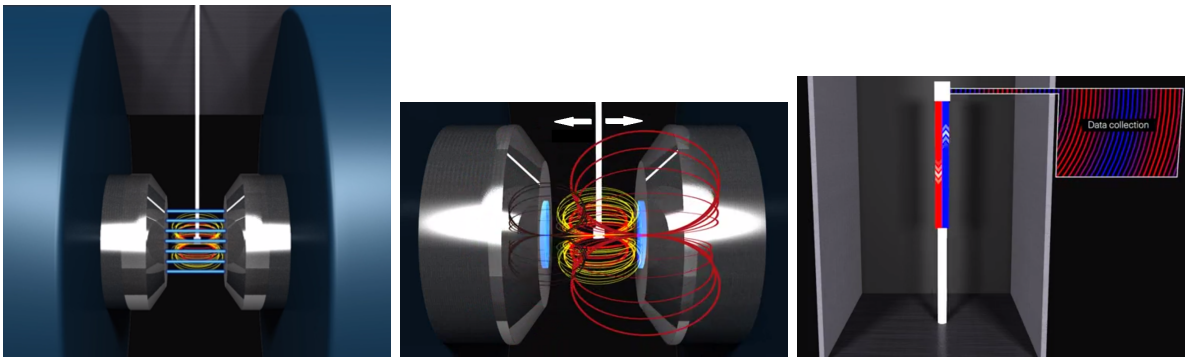

(a) (b) (c)

Figure 2.6: (a) Illustration of the uniform static magnetic field H created by the electromagnet. (b) Gradient coils (light blue) creates an alternating field which interacts with the sample. (c) The piezoelectric sensor that converts the mechanical displacement of the sample into alternating current. Adapted from [49], page 184-185.

involving alternation of H down to zero. For the magnetisation measurements the static magnetic field H was changed from zero to $+H_{max}$=+14 kOe, then to $-H_{max}$, before changed back to $+H_{max}$, and finally back to zero, with increments of 30 Oe, to obtain the magnetisation hysteresis loop of the sample. The alternating had a frequency of 632 Hz. The samples were measured in the IP and the OOP directions, so two hysteresis curves were obtained per sample. Nor the Cu/Cr cathode layer of the PC template were removed before the measurement, but the paramagnetic contribution from the metals and the diamagnetic contributions from the PC, are considered as small compared to the ferromagnetic metals. These contributions were later compensated for by a dia-/paramagnetic adjustment procedure performed by the MicroMag software.

2.4 Characterisation of magnetotransport properties

Magnetotransport measurements in the CPP geometry, were carried out in a setup with instruments from Lake Shore Inc. The system injects current to obtain the resistance of the sample. In combination with an electromagnet able to apply a uniform magnetic field up to 0.9 Tesla, the resistance of the sample as a function of the applied field was measured in room temperature, and some samples in temperatures down to 10 K.

2.4.1 Sample design for transport measurements

To prepare the samples for transport measurements, the Cr/Cu cathode layer needed to be partially removed, to leave two electrodes connected by the nanowires. Selective plasma etching was performed in a Plassys MP500S instrument with Ar plasma working on 80 W, with Ar flow of 5.0 sscm. The etching time had to be calibrated for each type of template and depended on the cathode layer thickness. The cathode layer thickness and the corresponding etching time for all used templates, are reported in Table 2.11. The samples were cut and mounted on a glass plate and covered with a home-made mask of two thin glass plates, leaving a ∼1 mm gap to be exposed to the plasma. The samples before and after plasma etching are shown in Figure 2.7.

Table 2.11: Cathode layer thickness and the corresponding etching time for all used templates.

NW Ø, Porosity	**40 nm, 20%**	**40 nm, 2%**	**80 nm, 8%**	**105 nm, 20%**
Cathode layer	10 nm Cr, 150 nm Cu.	10 nm Cr, 150 nm Cu, 10 nm Cr, 150 nm Cu.	10 nm Cr, 400 nm Cu.	10 nm Cr, 700 nm Cu, 200 nm Au.
Etching time	25 min	38 min	41 min	1 h, 25 min

(a) (b)

Figure 2.7: (a) Two samples mounted in the improvised glass sample holder before plasma etching (b) The same samples after the cathode has been etched off. The black area is the nanowire network inside the PC membrane, which can be seen as the white area on the edges.

The samples prepared from the electrodeposition were large enough to cut into three pieces. Two of the pieces were plasma etched simultaneously and later mounted on the same chip for transport measurement. The third piece was saved for later use, such as AGM and SEM measurements.

2.4.2 Room temperature magnetotransport measurements

The plasma etched samples, of around 7 mm length, were mounted in pairs on 14-node chips, as shown in Figure 2.8. As mentioned above, two samples from the same electrodeposition and

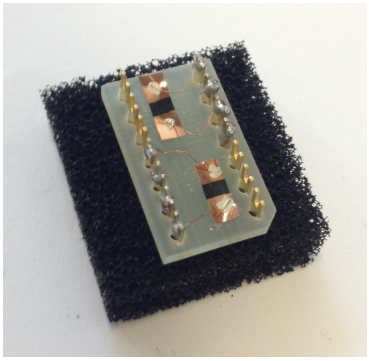

Figure 2.8: Two samples from the same electrodeposition mounted on a chip, connected in a pseudo four-point probe configuration.

plasma etching were mounted together. These were labeled A and B, or C and D etc. The contacts were made by connecting thin Cu wires soldered to the chip nodes to the electrodes of the samples with Ag paint. Each of the wires were connected to two chip nodes. This constitutes a pseudo four-point probe method setup, where the current and voltage can be measured on the individual chip nodes. This method gives correct measurements as long as the internal resistance R_{int} of the circuit is much higher than the resistance of the sample R_{sample}.

The samples were measured at room temperature and normal pressure. The setup monitored the alternating current signal to calculate the resistance of the sample as a function of an applied uniform magnetic field **H**. The circuit is schematically depicted in Figure 2.9 which is a section view of Figure 1.16. The field ranged between ±9 kOe (0.9 T) with a stepwise increments of ±50 to 100 Oe. Inside the chamber, the sample could be rotated by 90 degrees relative to the applied field, to allow measurements in the in-plane (IP) and the out-of-plane (OOP) directions. The magnetic field was created by a Model 643 electromagnet from Lake Shore. The current through the sample was controlled by a 7265 DSP Lock-in amplifier from Signal Recovery. The voltage drop across the sample V_{meas} was measured by a Keithley 2000 Multimeter. The instruments were connected to a computer that calculated R_{sample} from the measured current and voltage, and plotted the resistance as a function of the applied field. The applied field was measured by a Lake Shore Hall probe, where the magnetic field at the probe could be calculated from the measured Hall current.

2.4.3 Low temperature magnetotransport measurements

The samples showing highest GMR were also measured at temperatures down to 10 K. The sample-containing chamber was evacuated to vacuum, purged with He several times to remove air and moisture, before filled with He to reach a pressure of 0-2 psi. The chamber was cooled down to approximately 10 K by using a CTI-Cryogenics Helix Technology Corporation 8200 Compressor using liquid helium to cool down the chamber. Similar to the previously described setup, the resistance of the sample as a function of the temperature, was measured as the temperature decreased from room temperature to low temperature, and when the sample was

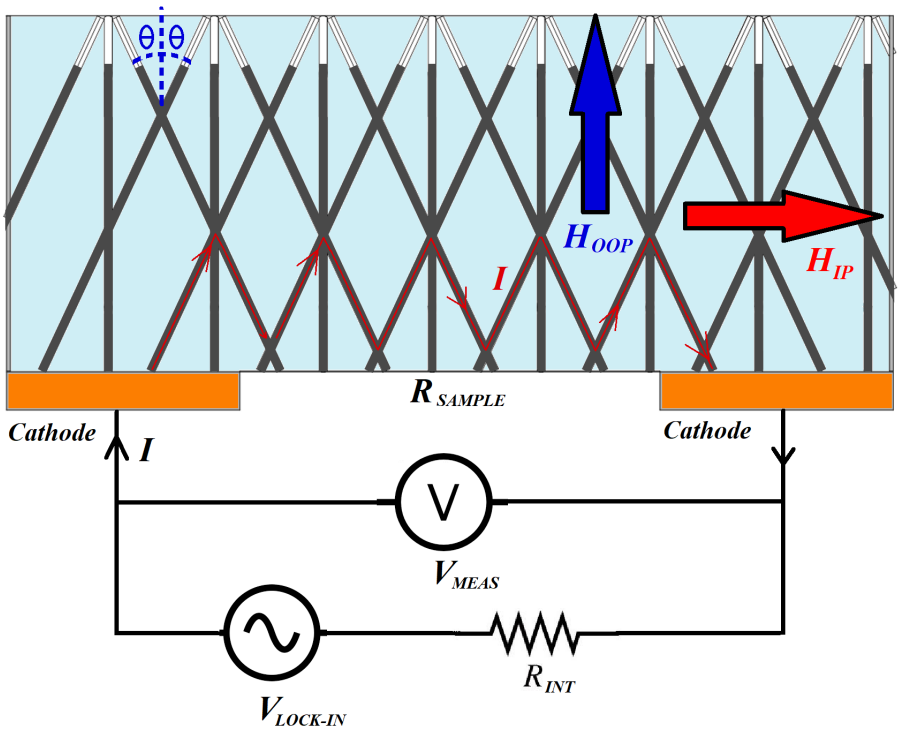

Figure 2.9: Schematic illustration of the circuit for magnetotransport measurements of the nanowire network. The applied field **H**, in the IP and OOP directions, is indicated by the arrows. Alternating current I is injected by the lock-in through the remaining cathodes, and a possible current path through the sample is indicated by red arrows. A voltmeter is connected in parallel to measure the potential drop across the sample corresponding to R_{sample}. The internal resistance is indicated by R_{int}. The angle $\theta = 25° \pm 5°$ between the nanowires is indicated in the nanowire network.

heat up to room temperature again.

Magnetotransport measurement was performed at 10 K for the most interesting samples. For selected samples, also at every 50 K up to room temperature. The temperature was measured by two thermometers; one at a finger sensor inside the chamber, and one at the sample holder. The latter measured the temperature closest to the true temperature of the sample. Controlled heating up to the intermediate temperatures were done by using a resistive heating element inside the chamber following a PID temperature control, monitored by the computer software.

Summary of Chapter 2

From the basis of a previously reported procedure [10], optimisation of electrodeposition parameters for interconnected NiCoCu/Cu multilayered nanowire networks have been systematically carried out through testing over a wide range of parameters. The optimal Cu^{2+} electrolyte concentration have been found to be 15 mM. The effects on the GMR when preparing samples in templates with a reduced number of crossing zones were investigated. Templates that have been used include pore diameters of 40, 80, and 105 nm, with various porosity and number of crossing zones. Extensive work was made in attempts to solve difficulties concerning the fabrication of samples with low porosity. Continuous NiCoCu nanowires have been prepared in all the different templates and electrolytes, for comparison with the multilayers. Additionally, to obtain samples with reduced saturation field, interconnected trilayer networks, and multilayers with 105 nm diameters, have been attempted.

All samples have been characterised by their magnetotransport properties at room temperature, and selected samples at temperatures down to 12 K. Many samples have had their magnetic properties characterised, and some samples of continuous nanowire networks were measured with SEM to investigate the morphology, and with EDX to obtain the NiCoCu alloy composition.

Chapter 3

Results and discussion

3.1 Influence of electrodeposition parameters for optimised magnetoresistance

As described in Section 2.1.1 the electrodeposition parameters were optimised to get samples with GMR ratios as high as possible. Starting from using earlier reported deposition parameters for similar studies on NiCoCu/Cu multilayered parallel nanowires in porous alumina templates with diameters of 250 nm [10], different parameters were systematically tested in series of samples to optimise each parameter individually. The potential of the NiCoCu layer pulse $V_F = -1.0$ V was adapted from [10], and worked so well that it was used for all the samples in this work. After all, a change in V_F would have changed the composition and deposition rate of the NiCoCu layer according to Figure 1.20a. A change in V_F would thus have required to do the optimisation of all the parameters over again. Below, the experimental results and discussion leading to the optimisation of the deposition parameters will be reported. This includes the potential of the Cu layer pulse V_N, the deposition time of the NiCoCu layer pulse, and the deposition time of the Cu layer pulse.

3.1.1 Optimisation of potentiostat parameters

Optimisation of deposition potentials

The following section includes the results and discussion based on the sample series *'V_N 25mM'*, deposited with parameters reported in Table 2.1. Only a few samples were required to decide the optimal V_N to be -0.4 V. During the Cu layer pulses the cathode current was close to zero for V_N of -0.2 and -0.3 V. Also, the negative current at the beginning of each Cu layer pulse was large, indicating high degree of dissolution of the previously deposited NiCoCu layer. At -0.4 V the cathode current was higher and the magnitude of the negative current at the beginning of the Cu layer pulse was acceptable.

Optimisation of NiCoCu layer deposition time

This section includes the results and discussion based on the sample series *'F 25mM'*, deposited with parameters reported in Table 2.2. The goal was to deposit well-defined NiCoCu layers as thin as possible. The presence of GMR counted as proof for well-defined layers of NiCoCu and Cu, and this feature was clear from characteristically sharp MR curves of samples deposited with $V_F = -1.0$ V for 300 milliseconds. Samples deposited with 200 milliseconds showed no GMR effect, only broad MR curves characteristic of AMR, which means that the layers were incomplete. Since 300 milliseconds appeared to be the lowest pulse time that created well-defined NiCoCu layers, this was chosen as the optimal NiCoCu deposition time. Figure 3.1 shows illustrations of what is meant by complete and incomplete layers.

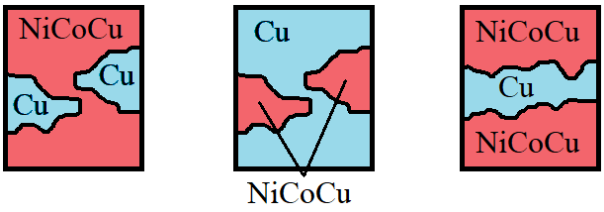

Figure 3.1: Schematical illustrations of sections of a NiCoCu/Cu ML NW showing (left,middle) two scenarios where the layers are incomplete, and preventing the GMR effect, and (right) an example of complete well-defined layers.

Optimisation of Cu layer deposition time

The following section includes the results and discussion based on the sample series *N 25mM*, deposited with parameters reported in Table 2.3. Typical plots of the deposition current as a function of time are shown in Figure 3.2 for both interconnected multilayered nanowire networks (a) and continuous ones (b).

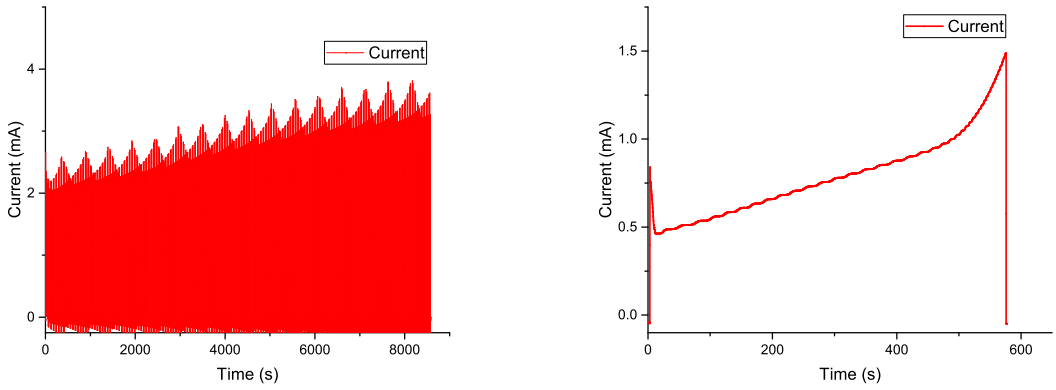

(a) (b)

Figure 3.2: Cathode current as a function of time for the electrodeposition in 20% 40 nm templates of interconnected networks of (a) multilayered NiCoCu/Cu with 600 bilayers. The 600 current peaks are too close to each other to separate them. (b) continuous NiCoCu nanowires. The sudden increase in the current after ∼500 s corresponds to the time where the template started to overfill-

The morphology of a sample of continuous nanowires deposited with the same electrolyte as the multilayers in the 20% 40 nm templates were obtained using FE-SEM, and a selected image is shown in Figure 3.3a. Evidently the network is quite dense, and the nanowires are connected to each other with repeating angles, as expected. Note that this occurs even though the protecting template is removed. The network is thus mechanically self-supporting. This was not the case for the multilayered samples, which were too fragile to prepare for SEM, and they dissolved together with the PC membrane. The reason for this is probably all the mechanically weaker interfaces between the layers, that detach during the PC dissolution.

The EDX analysis of the same sample gave information about the presence of elements and the composition, as shown in Figure 3.3b. The first two peaks characteristic to carbon and oxygen, which belongs to remains of undissolved PC. The large peak at around 0.8 keV is a combination of peaks from Ni, Co and Cu, which peaks are hard to separate. However, more separated peaks

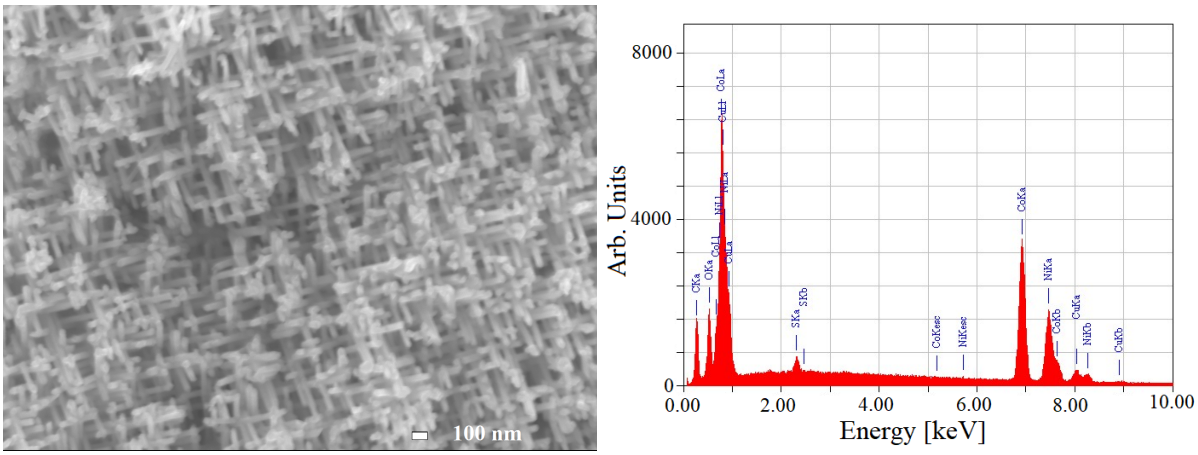

(a) (b)

Figure 3.3: (a) FE-SEM image of a sample of a continuous NiCoCu interconnected nanowire network. The indicated scaling length in 100 nm. (b) EDX analysis showing the intensity versus energy of the back-scattered electrons, giving information about the presence and amounts of the elements.

are found at energies from between 7 and 9 keV, that allows to separate them and calculate the relative proportions. The alloy composition of the sample measured was approximately $Ni_{56}Co_{36}Cu_8$, but with a relatively large uncertainty because the sample was only measured in one section. Additionally, the amount of Cu could easily be overestimated in case not all the Cu in the Cu/Cr cathode layer is removed. However, the EDX analysis did not show any signs of Cr, and hence there should be no cathode layer Cu left either.

Figure 3.4a shows the IP and OOP GMR ratio values for the samples with different Cu layer deposition time. The samples prepared with a Cu layer deposition time less than 8 seconds did not show any GMR effect, and where thus left out. Many samples were prepared for each Cu deposition time. The values shown in this figure belong to the best of the samples that was prepared with the respective Cu deposition time. The highest IP GMR value of the *N 25mM* series is 12.0% and belongs to the sample deposited with 10 seconds Cu layer deposition time. 10 seconds thus seem like the optimal time for this layer in this particular template and electrolyte.

The difference between IP and OOP GMR lies between approximately 0.5 and 1.0 percentage point for all the samples represented, and correspond approximately to the AMR. It was observed differences in the GMR of samples from the same deposition and plasma etching (labeled A and B). Figure 3.4b shows this variation as plots of the series of A and B samples. Note that whether a sample was labeled A or B was completely random. The distribution shows that the differences in IP GMR varied less than 1 percentage point between samples A and B, except for the samples with 8 seconds of Cu deposition time where the difference is around 2.5 percentage points.

Based on this it seems like the nanowires deposits quite symmetrical in the template. It cannot be concluded that the deposition is homogeneous, which anyway is unlikely due to the geometry of the deposition setup. The deposition should be disfavoured close to the edges of the sample compared to the center. Samples which overfilled during electrodeposition points towards this as the overfilling was more prominent in the center of the sample than near the edges, as shown in Figure 2.3a.

Figure 3.5 shows the magnetotransport properties of the best sample, $607A$, represented in three different ways, in addition to the magnetisation curves in the IP and OOP directions. This

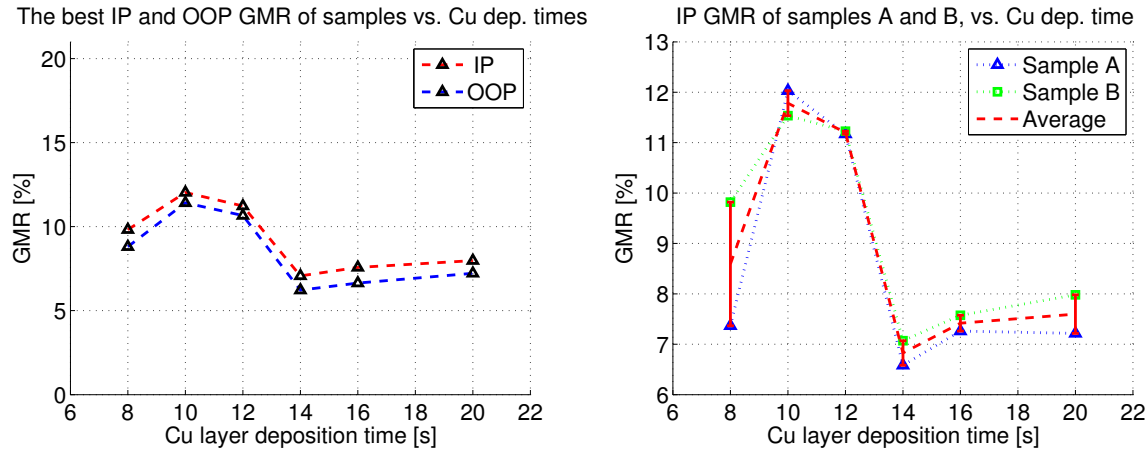

(a) (b)

Figure 3.4: (a) IP and OOP GMR ratio samples of the *N 25mM* series, deposited with Cu layer deposition times ranging from 8 to 20 s.(b) Variation in IP GMR indicated by errorbars for the samples A and B.

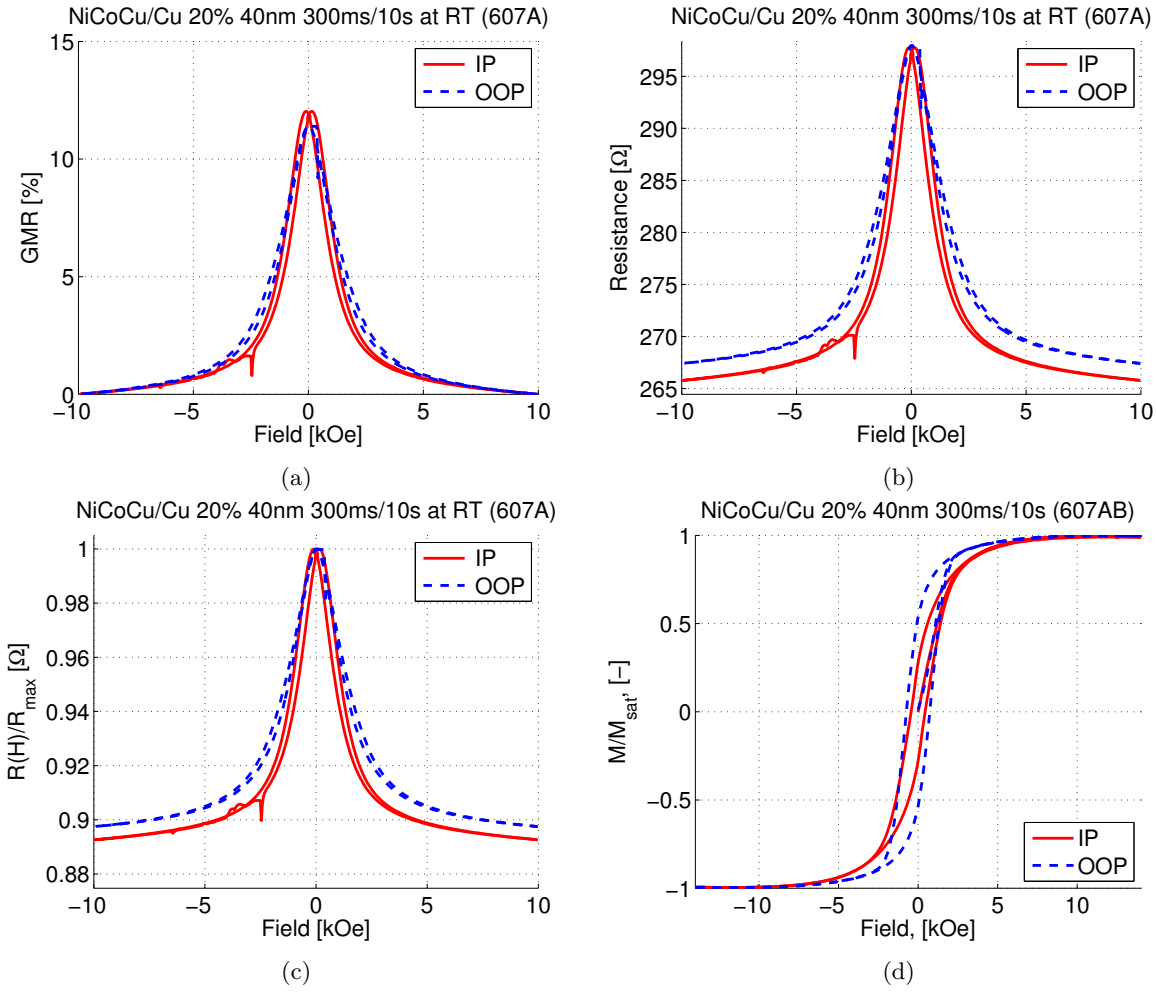

(a) (b) (c) (d)

Figure 3.5: (a) GMR curves of the best sample (607A) of the *N 25mM* series. (b) Resistance versus applied field, (c) normalised resistance versus applied field, and (d) normalised magnetisation curves of the sample 607A.

sample was deposited with Cu layer pulses of 10 seconds. The GMR curves in Figure 3.5a have almost the same shape both IP and OOP, and the sample seems to saturate at a slightly lower field than the OOP direction. This points towards an easy magnetisation axis along the IP direction, which is the expected result for multilayers when the spacer layer is thin and disk-shaped. However the magnetisation curve in Figure 3.5d shows that the OOP direction reaches saturation at lower fields than the IP direction, pointing towards an easy axis in the OOP direction, in contrast to the GMR curves. The higher saturation field in the IP direction is due to the arising demagnetising fields, and this is in agreement with earlier reports [43]. However the magnetic anisotropy is quite small in the IP and OOP directions, which is expected to be good in terms of getting high GMR effect. The OOP easy magnetisation direction and the low anisotropy indicates that the relation between the aspect ratios of the NiCoCu and Cu layers corresponds to a positive but small effective demagnetising field H_{eff}, as discussed in Section 1.1.4 and shown in Figure 1.7. Figure 3.5b shows the resistance curves directly as obtained from the measurements. It is interesting that the IP and OOP resistance curves have equal maximum values. This indicates that the nanowire network obtains the same arrangement in magnetisation of the layers close to zero field, even after being saturated in different directions.

From the normalised resistance curves in Figure 3.5c the approximate anisotropic magnetoresistance (AMR) is the difference between the IP and OOP curves at the saturation field. This is an approximation to Equation 1.31 which can be used when the AMR is small. The AMR in continuous interconnected nanowire networks of pure NiCo have been determined for various compositions [4], and the results are shown in Figure 3.6. From this figure an AMR ratio of approximately 3% can be expected for compositions of even amounts of Ni and Co, at room temperature and the effect seems to be almost doubled at 20 K. In multilayered systems the

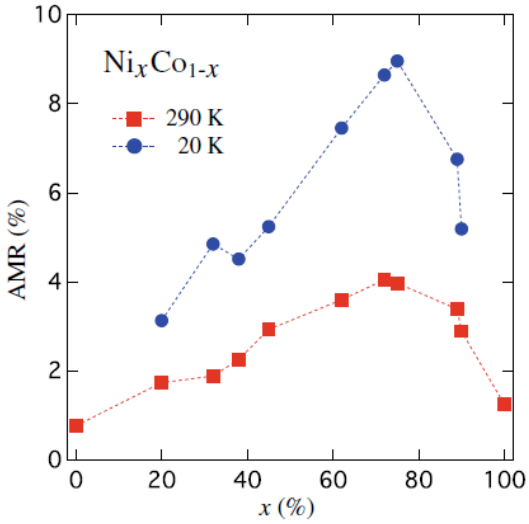

Figure 3.6: Variation of the AMR ratio versus the Ni concentration for Ni_xCo_{1-x} interconnected nanowrie networks, at 20 and 290 K. Copied from [4].

AMR can be expected to decrease from three different contributions. One is the increased resistance from the NiCoCu/Cu layer interfaces which increases the both the resistivities $\rho_{\parallel}$ and $\rho_{\perp}$, thus reducing the AMR ratio through Equation 1.31. Next is the contribution from the Cu impurities in the NiCoCu layer, which can be expected to reduce the AMR effect. The third contribution comes from the Cu layers in the nanowire. Cu does not contribute to AMR, and thus the total effect decreases compared to the continuous NiCoCu nanowire [4]. Based on this, the AMR effect in the multilayer system can be expected to be significantly reduce, possibly to a value of maximum 1-1.5%. In the measured sample ($607A$) the AMR value is approximately

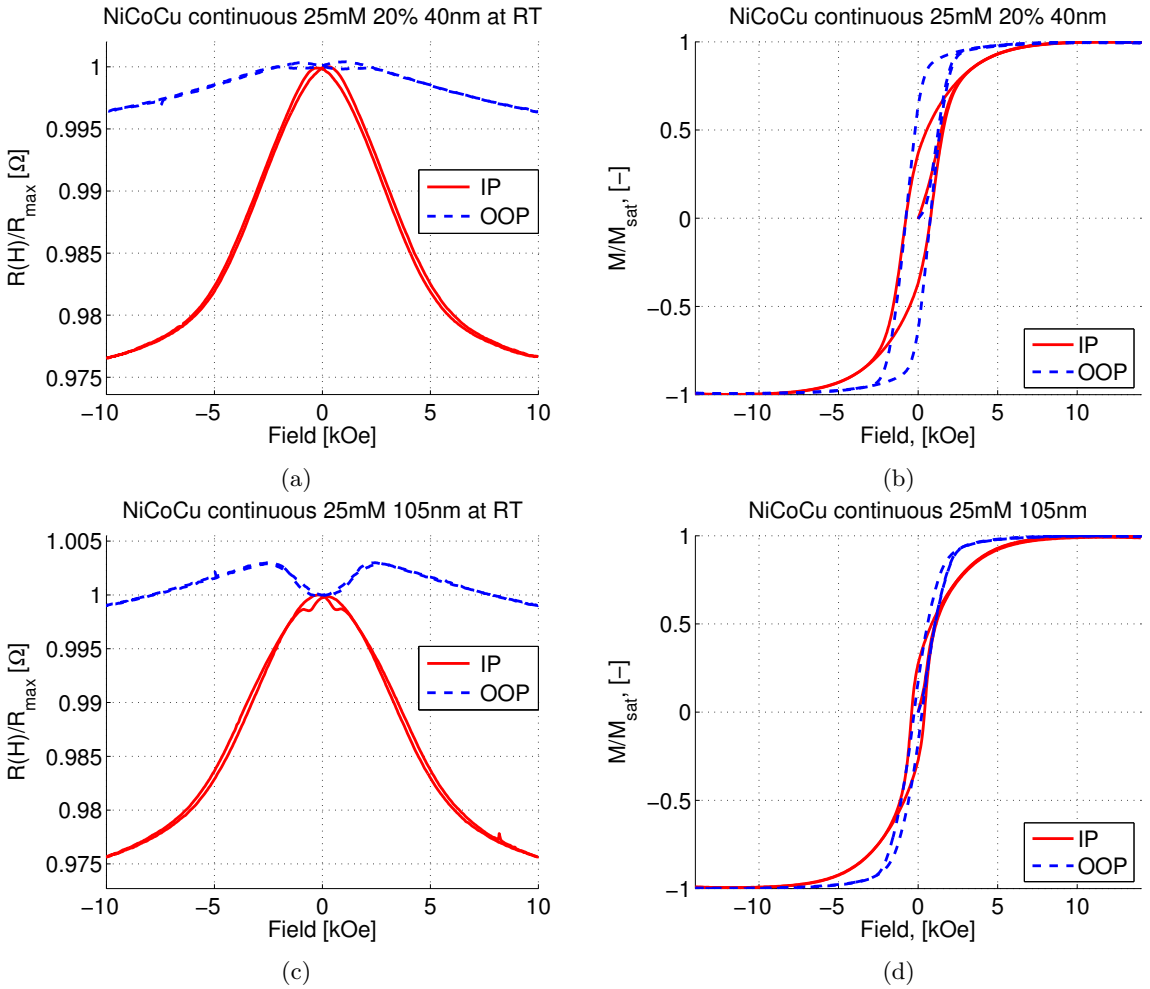

Figure 3.7: (a) Normalised resistance versus applied field for the continuous NiCoCu sample with NW diameter of 40 nm, and (b) is the normalised magnetisation curves for the same sample. (c) Normalised resistance versus applied field for the continuous NiCoCu sample with NW diameter of 105 nm, and (d) is the normalised magnetisation curves for the same sample.

0.5 percentage points, which is less than the expected optimal value, and the decrease must be attributed to the contributions just mentioned.

Furthermore, the magnetisation curve shows a remanent magnetisation of ∼28% and ∼55% of M_s in the IP and OOP direction, respectively. This means that the degree of antiparallelism in the two directions are not very high. As mentioned earlier in Section 1.2.4, a perfectly antiparallel zero-field arrangement is desired for maximum GMR. Furthermore, the coercive fields are noted as ∼0.43 and ∼0.72 kOe for the IP and OOP directions respectively. The high remanence might be a result of high magnetostatic energy contribution from the dipole-dipole interactions between the nanowires, as the network is very densely packed with nanowires.

For comparison, continuous nanowires of NiCoCu prepared under similar conditions were investigated. Figure 3.7a and 3.7c shows the normalised resistance curves for samples of 40 and 105 nm, respectively. Figure 3.7b and 3.7d shows their corresponding magnetisation curves. The AMR of both samples is approximately 2.5%. In comparison to ∼0.5% of AMR in the sample 607A.

Both magnetisation curves of the continuous samples show more prominently a favoured OOP direction of magnetisation than the multilayered sample, as is expected in terms of the shape

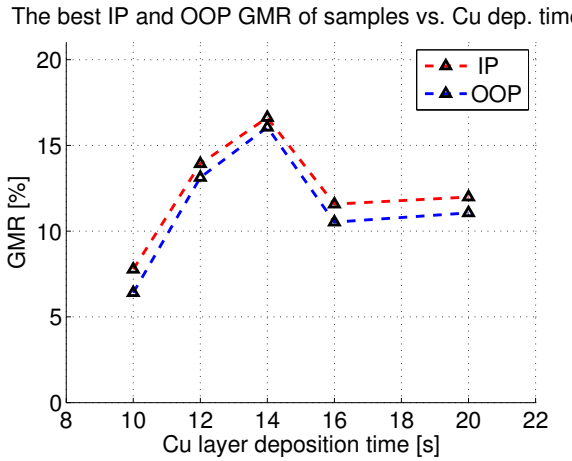

Figure 3.8: IP and OOP GMR ratios for samples of the *'20%600 15mM'* series, with Cu layer deposition time ranging between 10 and 20 s.

anisotropy. The coercive field and remanence of the continuous 40 nm sample are comparable to the multilayered sample, but for the sample with 105 nm diameter these quantities are reduced. This must be interpreted in the light of the domain formation inside the crossing zones. As explained in Section 1.3, domain wall propagation affected the magnetisation reversal properties of continuous nanowire networks, that reduce the coercive fields and remanence. As the formation of domains are favoured when the dimensions of the ferromagnet are increased, this effect should be more prominent for nanowires with large diameter, justifying the observed difference between the samples with 40 and 105 nm nanowire diameters. The former sample does not show any significant change in the coercivity and remanence compared to the multilayered sample, and this can indicate that domains are either not formed in the crossing zones, or that the domain walls cannot propagate out of them.

3.1.2 Optimisation of electrolyte Cu^{2+} concentration

The *'20%600 5mM'* and *'20%600 15mM'* series were prepared to investigate the influence of the Cu^{2+} concentration in the electrolyte. It is expected that the increased deposition rate in electrolytes with high Cu^{2+} concentration leads to higher defect concentrations in the Cu layers. This will decrease the GMR effect, as explained in Section 1.3. The deposition parameters were reported in Table 2.4.

15 mM Cu^{2+} electrolyte concentration

The *'20%600 15mM'* series contained samples with Cu layer deposition time ranging from 10 to 20 seconds. The SEM measurements of continuous nanowire samples showed similar morphology as the sample shown in Figure 3.3a. Elemental composition analysis revealed an alloy composition of Ni:Co:Cu of 52.2±0.5:42.3±0.8:5.5±0.3, which means a Cu concentration reduced by approximately 30% compared to the samples in the *'20%600 25mM'* series. According to the discussion in Section 1.1.3 this composition should favour an fcc crystal structure with negligible MC anisotropy.

Figure 3.8 shows the plot of the best IP and OOP GMR ratios for the samples in the *'20%600 15mM'* series. In general, the GMR values is higher than in the *'N 25mM'* series, meaning that an electrolyte containing 15 mM is better suited than 25 mM. The maximum GMR for the series belongs to the sample deposited with Cu layer pulse of 14 seconds. This sample has a IP GMR value of ∼16.6%, which is a ∼38% increase from the best sample of the *'N 25mM'* series. 14 seconds thus seem like the optimal Cu layer deposition time for this template and electrolyte.

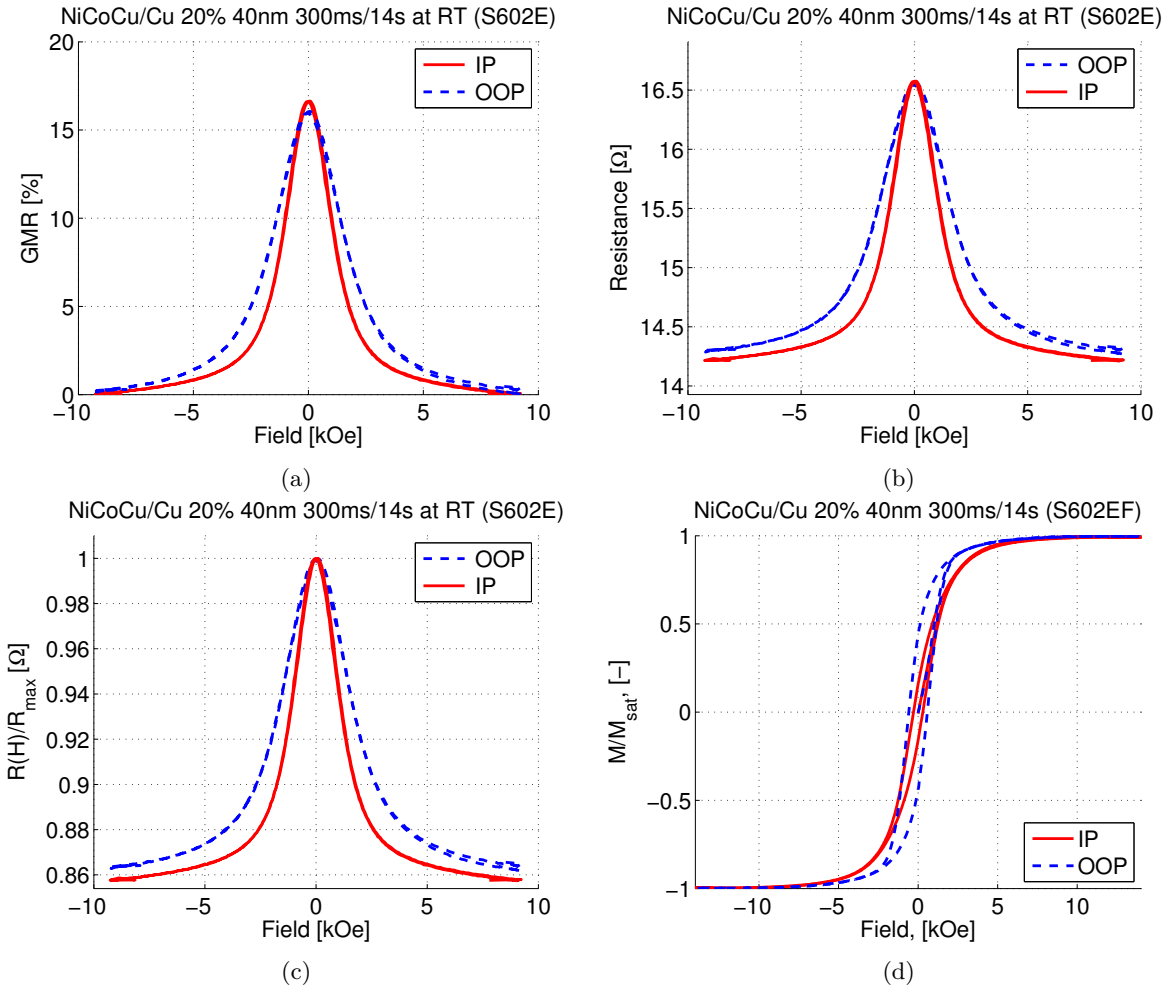

Figure 3.9: (a) GMR curves of the best sample (S602E) of the *'20%600 15mM'* series. (b) Resistance versus applied field, (c) normalised resistance versus applied field, and (d) normalised magnetisation curves of the sample S602E.

The AMR is approximately the difference between the IP and OOP GMR ratios, which is around 1 percentage point for all the samples; on average slightly larger than for the *'N 25mM'* series. This can indicate that there is more NiCo relative to the previous sample series. It is worth to notice that the shape of the curve is quite similar to the corresponding curve for the *'N 25mM'* series in Figure 3.4a, with a drop in GMR for Cu deposition time longer than the optimal value. The reason for this is not clear, as small variations in t_N is not expected to influence GMR this much. However, many samples with the same deposition parameters have been prepared, and the trend is similar and clear.

Figure 3.9 shows the magnetotransport properties of the best sample (S602E) of the *'20%600 15mM'* series in three different ways, in addition to the normalised magnetisation curves. The GMR curves in Figure 3.9a show a sharper peak for the IP field direction than the OOP field direction. All the curves in Figure 3.9 look almost similar as to the curves of the previously discussed sample ($607A$), with slightly more magnetic asymmetry in the case of $S602E$.

From the high field values of the normalised resistance curves in Figure 3.9c, the approximate AMR can be read out as ∼0.6%. This value is slightly higher than in the case of the 607A sample, but it is still below the expected optimal value. The increase in AMR is almost nothing

even though the Cu concentration in the NiCoCu layer has been reduced by 30%. Thus it can be concluded that the Cu in the NiCoCu layer does not significantly influence the AMR effect in the multilayered systems.

The normalised magnetisation curves look similar to the earlier case, with an easy magnetisation axis in the OOP applied field direction. The remanent magnetisations are 18% and 44% of M_s in the IP and OOP directions respectively. This is approximately 36% less in the IP direction and 20% less in the OOP direction compared to the previous 607A sample. Clearly the reduction in Cu concentration has lead to higher antiparallelism in the NiCoCu layers, leading to the lower zero field magnetisation. The increased antiparallelism can explain the large increase in the GMR effect.

It was mentioned earlier that the reduction in the electrolyte Cu concentrations should lead to a lower defect concentration, and thus decrease the resistance in the Cu layer. That might be the case as the resistance curves in Figure 3.5b and 3.9b show that the sample prepared from the lower Cu concentration has lower resistance. But the resistance of the different samples showed large variations in the resistance, even for samples from the same electrodeposition and plasma etching. Thus it cannot be concluded if this is the case, only based on the resistance curves of these two samples. There is a lot of factors that contribute to the resistance, such as inhomogeneous deposition and etching, contact resistance arising at the contacts between the chip and the sample, and mechanical fragility. Also, the resistance will decrease with the number of nanowires conducting in parallel. Since the number of conducting nanowires is unknown and probably different for each sample, great care should be taken before trying to conclude anything based on the resistance value of a sample.

However, the reduced Cu concentration is expected to decrease the deposition rate, which might result in more uniform growth on the surface. If this is the case, the resulting Cu spacer layers should have smoother interfaces and more uniform thicknesses. This should influence the interface scattering, although if it influences the spin-dependent interface scattering, and hence the GMR, is another question. In any case, more uniform growth can explain the increased GMR effect based on the influence of the dipolar coupling between the NiCoCu layers. As shown, the remanence was reduced by 20-36% upon reducing the Cu concentration, and the increased antiparallelism can be explained by dipolar coupling between the NiCoCu that favours an antiparallel arrangement.

The coercive fields in the IP and OOP directions are approximately 0.30 and 0.57 kOe, respectively. This corresponds to a decrease of around 30% and 21% in the IP and OOP direction respectively, compared to the 607A sample. A remark on the coercive fields is that they do not correspond to the peaks in the resistance curves. Thus, the coercive field cannot correspond to the state of maximum antiparallelism, or randomness, in the multilayers. This maximum occurs for fields much closer to zero. The fact that they do not correspond is surprising, but can be assumed to have a relationship with the fact that the multilayered nanowire network form a very complex system. They are crossed, which leads do different dipole-dipole interactions between the nanowires than in the case of parallel nanowire arrays. It thus seems like the maximum in the resistance curves is a result of competing dipolar interactions.

Continuous nanowires of NiCoCu prepared under similar conditions were investigated. Figure 3.10a and 3.10c shows the normalised resistance curves for samples of 40 and 105 nm, respectively. Figure 3.10b and 3.10d shows their corresponding magnetisation curves. The AMR of both samples is approximately 1.7-2.0%, which is one percentage point less than for the pure NiCo system. However the IP curves are obviously not saturated at this applied

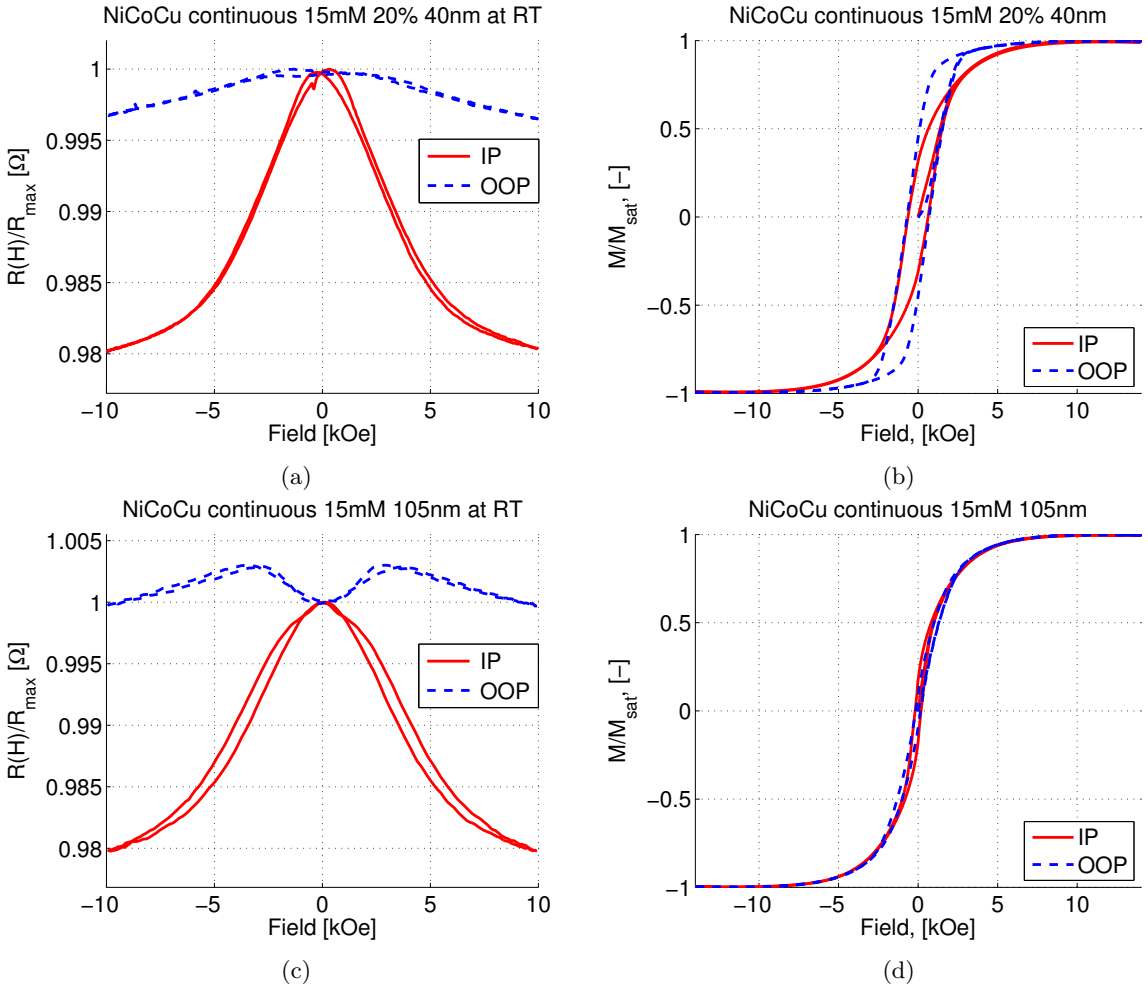

Figure 3.10: (a) Normalised resistance versus applied field for the continuous NiCoCu sample with NW diameter of 40 nm, and (b) is the normalised magnetisation curves for the same sample. (c) Normalised resistance versus applied field for the continuous NiCoCu sample with NW diameter of 105 nm, and (d) is the normalised magnetisation curves for the same sample.

field, and thus it does not make sense to make any conclusions based on the apparently reduced AMR effect. The reduced AMR effect of ∼0.6% in the sample $S602E$, indicates that the effect of the Cu layers and the interfaces between the layers have a significant AMR-reducing effect.

Both magnetisation curves of the continuous samples show more prominently a favoured OOP direction of magnetisation than the multilayered sample, as is expected in terms of the shape anisotropy. The coercive field and remanence of the continuous 40 nm sample are comparable to the multilayered sample, but for the sample with 105 nm diameter these quantities are reduced. In fact, the 105 nm sample is almost isotropic in the two field directions, with almost zero coercivity and low remanence relative to the 40 nm sample. The decrease in the coercive fields and remanence for the sample with 105 nm nanowire diameter, and the absence of change in the sample of 40 nm nanowire diameter, can be explained based on the same argumentation as in the earlier discussion on this matter. The tilt of the curves are almost the same for the continuous and the multilayered sample, indicating that the dipole-dipole interactions between the nanowires contribute to the magnetostatic energy similarly for the three samples. However the shape anisotropy is higher for the 40 nm samples, which is expected due to the higher aspect ratio.

Relationship between IP and OOP MR and AMR

In theory the difference in the IP and OOP MR should be a consequence of AMR. Equation 1.30 can be rewritten as a functions of resistances through

$$\frac{R(\varphi) - R_\perp}{R_\parallel - R_\perp} = \cos^2\varphi, \tag{3.1}$$

where $R(\varphi)$ is the resistance of the sample when the angle between the magnetisation and current is φ. If it is assumed that the magnetisation is always parallel to applied field the angle φ thus correspond to the angle between the applied field and the current. Indeed Equation 1.30 is only true when the $R_\parallel$ and $R_\perp$ correspond to the case when magnetisations are parallel or perpendicular, respectively, to the current. In the interconnected nanowire networks this will never be the case as the the nanowires have an angle relative to each other. Equation 3.1 will thus only be an approximation where $R_\parallel$ and $R_\perp$ are substituted with $R(H_{max}^{OOP})$ and $R(H_{max}^{IP})$ respectively, and φ is the angle between the applied field and the OOP direction. This results in

$$\frac{R(\varphi) - R(H_{max}^{IP})}{R(H_{max}^{OOP}) - R(H_{max}^{IP})} \approx \cos^2\varphi. \tag{3.2}$$

New magnetotransport measurements were performed on sample $S602E$. Now the sample were rotated relative to the applied field in small steps between $\varphi = 0°$ (OOP) and $\varphi = 90°$, and measured in order to obtain the resistance curves for different values of φ. The results were plotted in terms of Equation 3.2 and fitted to the curve corresponding to $\cos^2\varphi$ in Figure 3.11. The curve fits well with the expected $\cos^2\varphi$ dependency, so Equation 3.2 is obviously a good approximation to Equation 3.1. The curve deviates slightly from $\cos^2\varphi$ for angles close to 90°, which corresponds to the applied field parallel to the IP direction. This result proves that the difference between IP and OOP GMR in the interconnected nanowire networks is a result of AMR.

5 mM Cu^{2+} electrolyte concentration

The *'20%600 5mM'* series contained samples deposited with an electrolyte with Cu^{2+} concentration reduced to 5 mM. The experimental parameters are reported in Table 2.4. Figure 3.12 shows the IP and OOP GMR as a function of the Cu spacer layer deposition time, for three different samples.

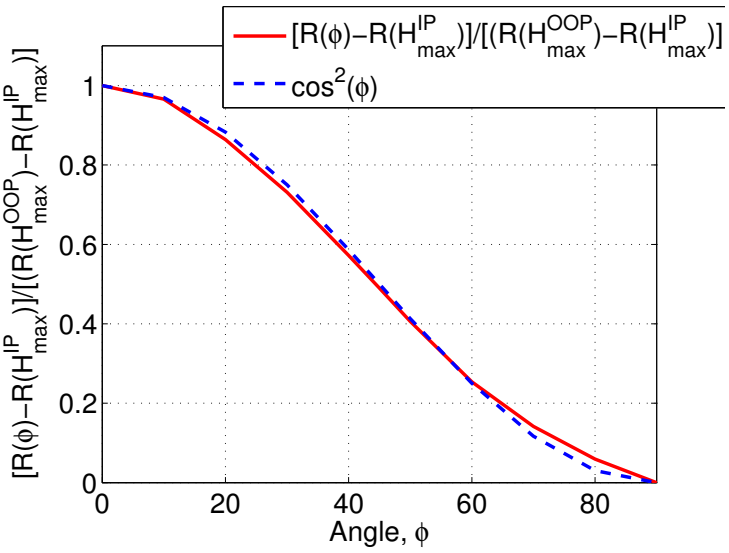

Figure 3.11: The left side of Equation 3.1 plotted versus the angle between the applied field and the OOP direction

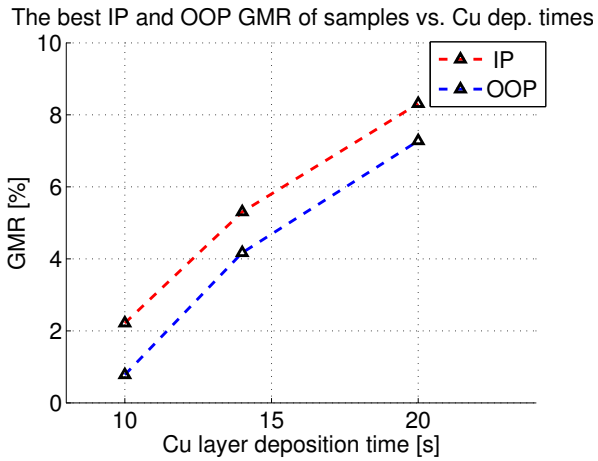

Figure 3.12: IP and OOP GMR ratios for samples of the *'20%600 5mM'* series, with Cu layer deposition time ranging between 10 and 20 s.

The sample deposited with 20 seconds of Cu deposition time shows a GMR effect of 8.3%, which is the best value of all the samples in this series. This is still lower by a factor of 2 compared to the 16.6% obtained from the electrolyte with 15 mM Cu^{2+} concentration. The reduced GMR effect may point towards thin, incomplete Cu spacer layers, as a result of the lower diffusion of Cu ions in the electrolyte. The approximate AMR obtained from the difference between the IP and OOP GMR is more than 1%, which is more than in the *'20%600 15mM'* series. Increased AMR indicates a larger amount of NiCoCu relative to Cu, which strengthens the theory of too thin Cu layers.

Indeed the GMR could be expected to increase if the Cu layer deposition time were increased further, but this would increase the total deposition time drastically to the point where it became impractical for studies. With 0.3 and 20 seconds for the NiCoCu and Cu layer deposition times, respectively, the electrodeposition process takes almost four hours. Upon increasing the bilayer deposition time to 30.3 and 40.3 seconds for instance, the electrodeposition would take five and almost seven hours, respectively. Based on these observations the process was considered too slow for further studies with 5 mM Cu^{2+} concentration.

Anyway, the best sample of this series was further characterised in the same manner as the previously reported samples, except SEM/EDX measurements. The sample was labeled $615B$, and showed 8.3% GMR at room temperature. The results of the magnetotransport and magnetic measurements are reported in Figure 3.13.

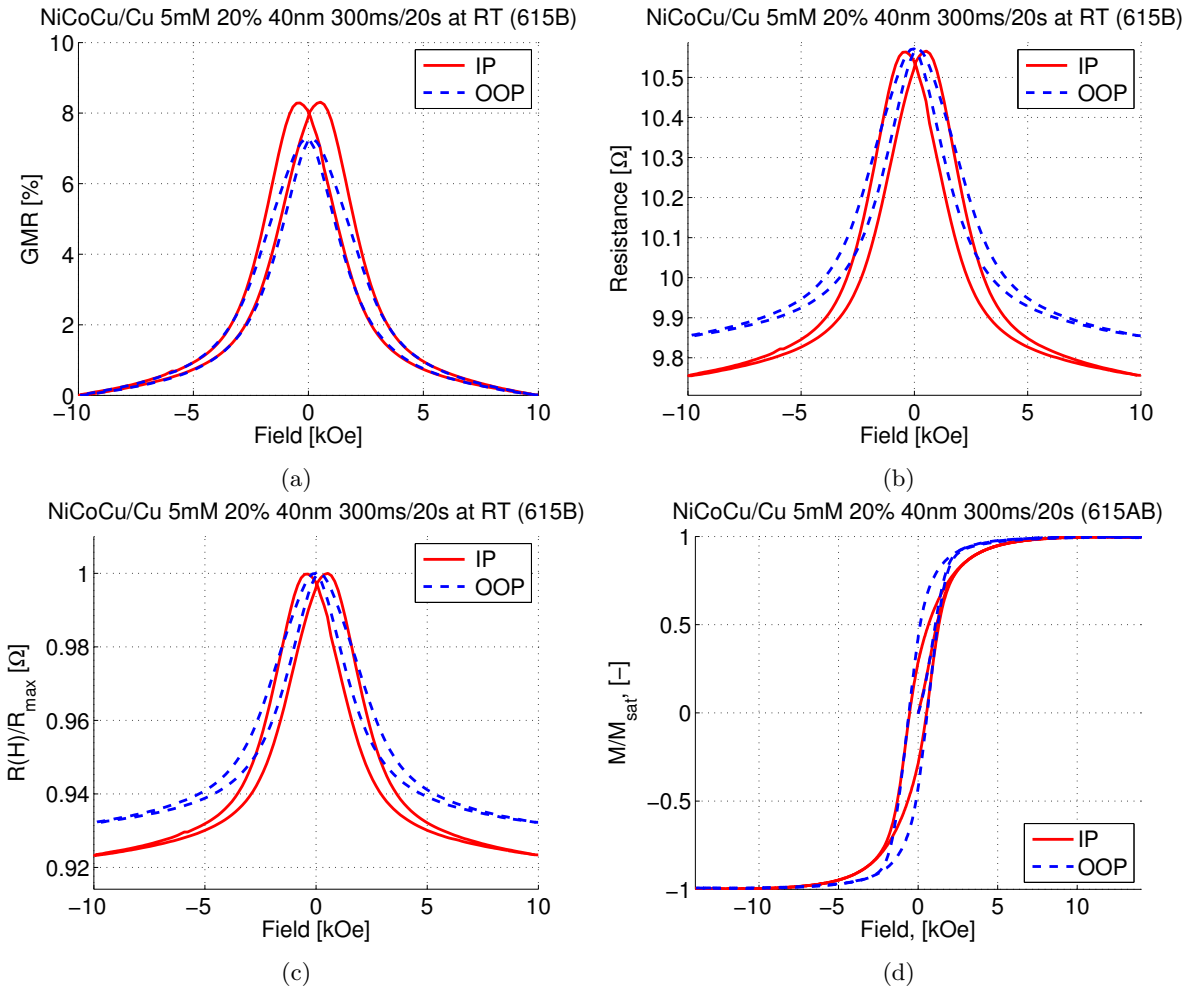

Figure 3.13: (a) GMR curves of the best sample ($615B$) of the *'20%600 5mM'* series. (b) Resistance versus applied field, (c) normalised resistance versus applied field, and (d) normalised magnetisation curves of the sample $615B$.

One very obvious difference compared to the $S602E$ sample, is the difference in the magnetisation reversal properties. This is evident from the shift of the peak in the $R(H)$ curves to higher absolute field values. In fact, the peaks occur at applied fields of ∼530 Oe, which is approximately equal to the coercive field in the IP direction. This relationship does not appear in the OOP direction. The GMR curves in the IP and OOP directions are exactly the same above field values larger than ±2-3 kOe. The normalised magnetisation curves shows that the easy magnetisation direction is OOP, and the saturation fields lies very close to the values of the $S602E$ sample. From this the effective demagnetising field H_{eff} seems to be positive, according to the theory explained in Section 1.1.4, which means that the system favours a magnetisation of the NiCoCu parallel to the longitudinal nanowire axis at zero field. The OOP remanent magnetisation is around 0.5 of M_s, which is the same as the previous sample, but the IP remanence of around $0.3M_s$ is larger than that of the previous sample, pointing towards a lower degree of antiparallel arrangement in the current sample. The tilt of the magnetisation curves are similar to the previous sample, indication that the dipolar interactions between the nanowires are of similar magnitudes.

Figure 3.14 shows the normalised $R(H)$ and magnetisation curves for continuous interconnected NiCoCu nanowire networks of two different nanowire networks: 40 and 105 nm. For the sample with 40 nm nanowire diameter, Figure 3.14a shows a difference in the IP and OOP resistance corresponding to ∼1.8% which approximately is the AMR. The AMR is larger than the AMR of the multilayer by a factor of ∼2. The AMR is approximately the same as for the samples deposited from the electrolyte containing 15 mM of Cu^{2+}, and this observations strengthens the conclusion that the Cu in NiCoCu does not significantly reduce the AMR effect. The normalised magnetisation curves in Figure 3.14b shows a favorable magnetisation direction OOP as expected, with lower saturation field OOP that IP caused by the increased shape anisotropy.

The similar curves corresponding to the sample with 105 nm nanowire diameters are shown in Figure 3.14c and 3.14d.

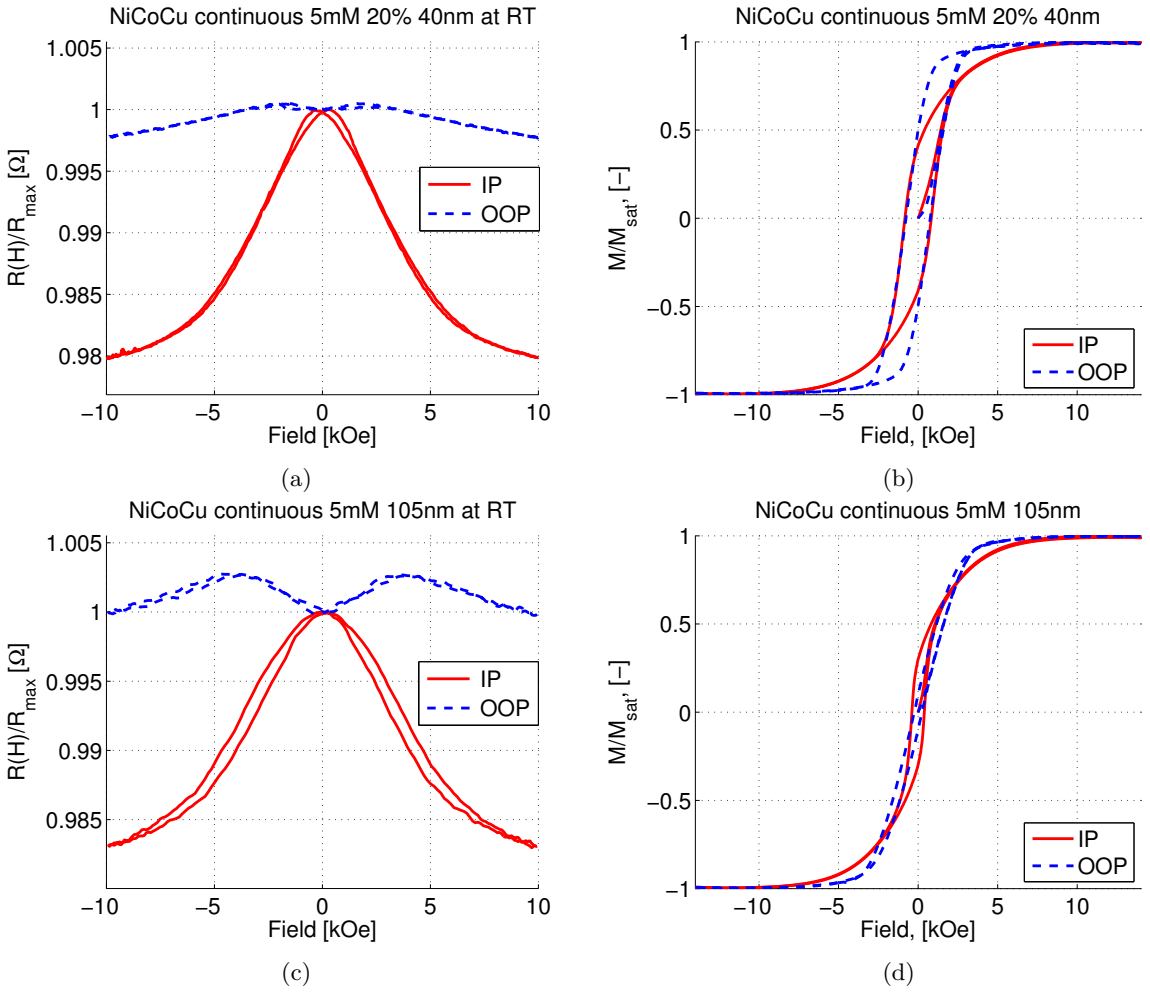

Figure 3.14: (a) Normalised resistance versus applied field for the continuous NiCoCu sample with NW diameter of 40 nm, and (b) is the normalised magnetisation curves for the same sample. (c) Normalised resistance versus applied field for the continuous NiCoCu sample with NW diameter of 105 nm, and (d) is the normalised magnetisation curves for the same sample.

For the sample with nanowire diameters of 105 nm, he approximate AMR value extracted from the normalised resistance curves, in Figure 3.14c, is ∼1.7%, which is approximately similar to the 40 nm nanowire diameter sample. The magnetisation curves show less anisotropy in the sample since the IP and OOP curves are more matching. The tilt is somewhat stronger, pointing towards stronger dipolar interactions between the nanowires. The IP remanence is almost equal

to the previous sample, but the OOP remanence is almost zero. This trend is similar to the ones discussed for the samples with higher Cu concentration, and can be attributed to the crossing zones.

Low temperature measurements

To investigate the influence of the temperature on the GMR, transport measurements were performed at ∼12 K. As described in Section 1.2.2, electron-magnon scattering leads to mixing of the spin-current channels, hence reducing the GMR effect at high temperatures. Earlier reports show an increase of the GMR effect by a factor between 2 and 3, at low temperatures [1, 43]. Figure 3.15 shows the GMR, resistance, and normalised resistance curves, as well as the GMR ratios measured at different temperatures, for the S602E sample, at 12 K. The width of the peaks are larger, meaning that the saturation field is higher at low temperatures. This is expected as there is less thermal energy available to contribute to the magnetisation reversal process. The peak is slightly wider in the OOP direction and saturates at higher fields than in the IP direction, similar to the room temperature measurement.

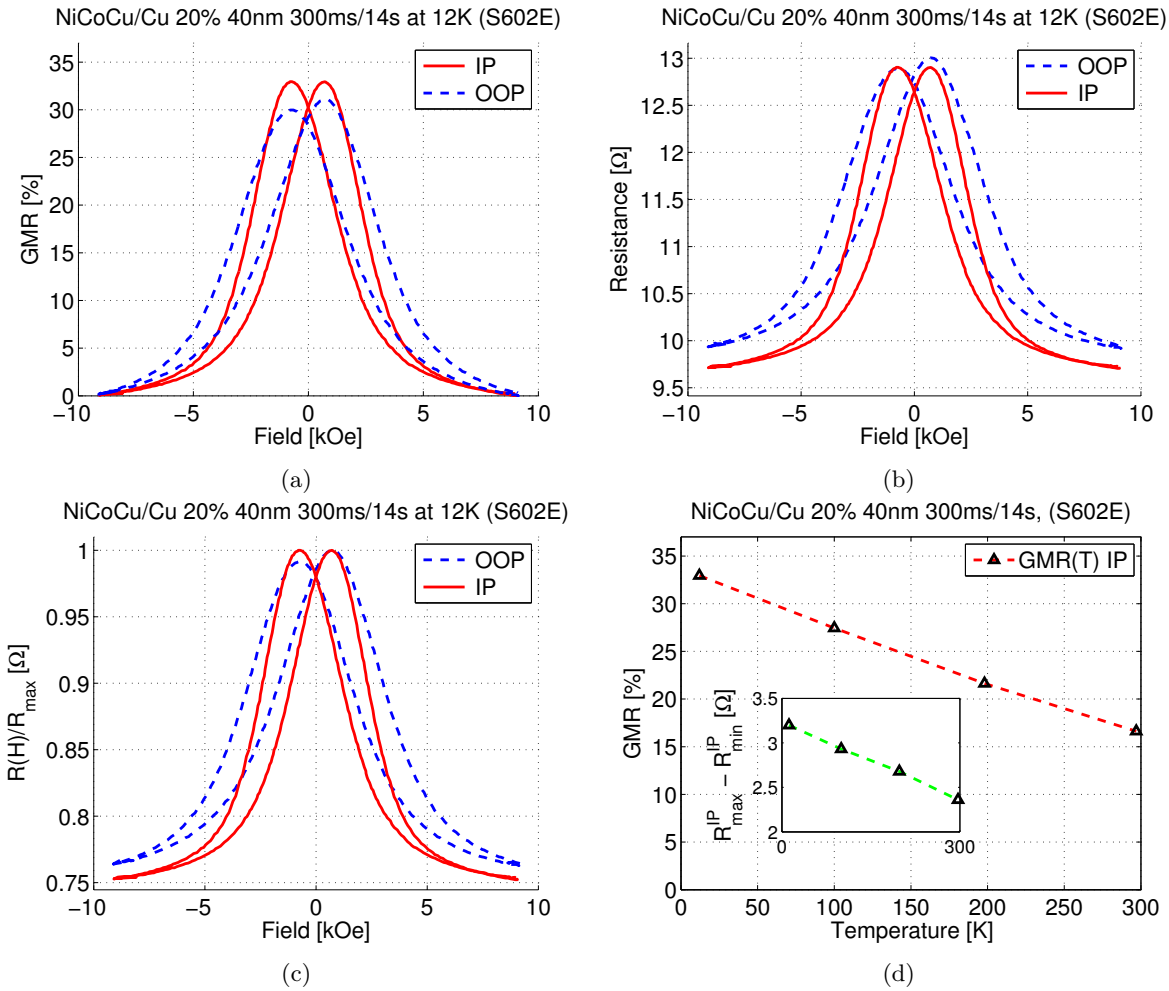

Figure 3.15: Magnetotransport measurements of sample S602E at 12K. (a) GMR curves of the best sample (S602E) of the *20%600 15mM* series. (b) Resistance versus applied field, (c) normalised resistance versus applied field, and (d) GMR ratios corresponding to different temperatures. The inset shows GMR$\times R^{IP}_{min} = R^{IP}_{max} - R^{IP}_{min}$.

Figure 3.15a shows that the IP GMR ratio has increased to almost 33%. That is an increase by

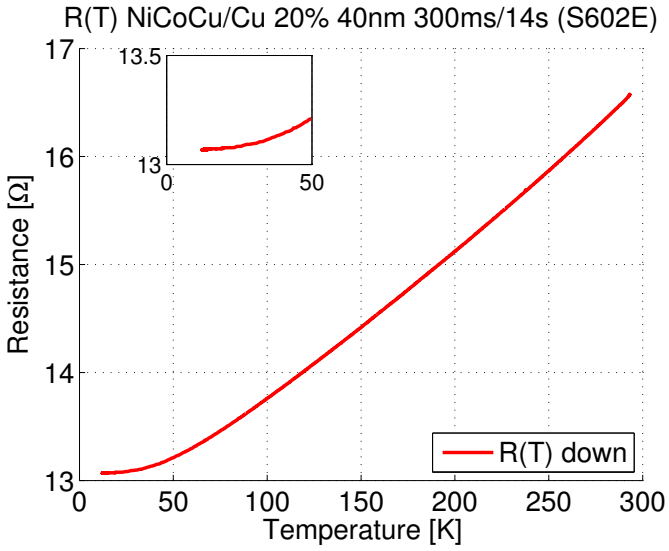

Figure 3.16: Resistance versus temperature measured on sample S602E when cooling from room temperature down to 12 K. The inset shows the same curve in the temperature range up to 50 K to clearly show the resistance plateau.

a factor of around 2 compared to the room temperature GMR. From the normalised resistance curves in Figure 3.15c the approximate AMR can be read out as ∼1.1%, which is an increase with a factor of around 2 compared to the room temperature AMR, which correspond well with the predicted increase based on Figure 3.6 [4].

Figure 3.15d shows the IP GMR values measured at different temperatures from 12 K and up to room temperature. Interestingly, the trend is linear all the way down to 12 K. Based on the discussion on electron-magnon scattering in Section 1.2.2, it seems like magnons are still excited at 12 K. If not, there should be a plateau in the GMR, caused by the residual spin-flip scattering from spin-orbit scattering or imperfections. The inset in Figure 3.15d shows $R^{IP}_{max} - R^{IP}_{min}$ as a function of temperature. This curve has the similar linear behaviour as the GMR(T) curve, proving that the absence of a GMR plateau at low temperatures, is not caused by the resistance plateau at low temperatures caused by the residual resistance. This behaviors is very different from similar investigations performed on NiFe/Cu multilayered nanowires where the GMR was almost unchanged between 77 K and 4.2 K [1].

The resistance of the sample was measured as the temperature was decreased from room temperature to 12 K. Figure 3.16 shows the temperature dependence of the resistance. The curve decreases almost linearly with temperature due to decreasing electron-phonon scattering. At around 70 K the curve starts to flatten out. At around 12 K it has reached the plateau of the residual resistance, where the electron transport is limited by static defect scattering. The residual resistance is approximately 21% less than the resistance at room temperature.

3.2 Influence of template porosity on magnetoresistance

In order to further improve the GMR, samples were grown in templates with a minimum amount of crossing points between the pores, to reduce the effect from the crossing zones. Two different templates were used, where one had pores of 40 nm and the other had pores of 80 nm. This resulted in templates with porosities of 2% and 8%, respectively. The number of crossing points between nanowires were the same in the two templates, and the number was reduced by a factor of 10 compared to the highly porous 20% 40 nm template. Two sample series were made:

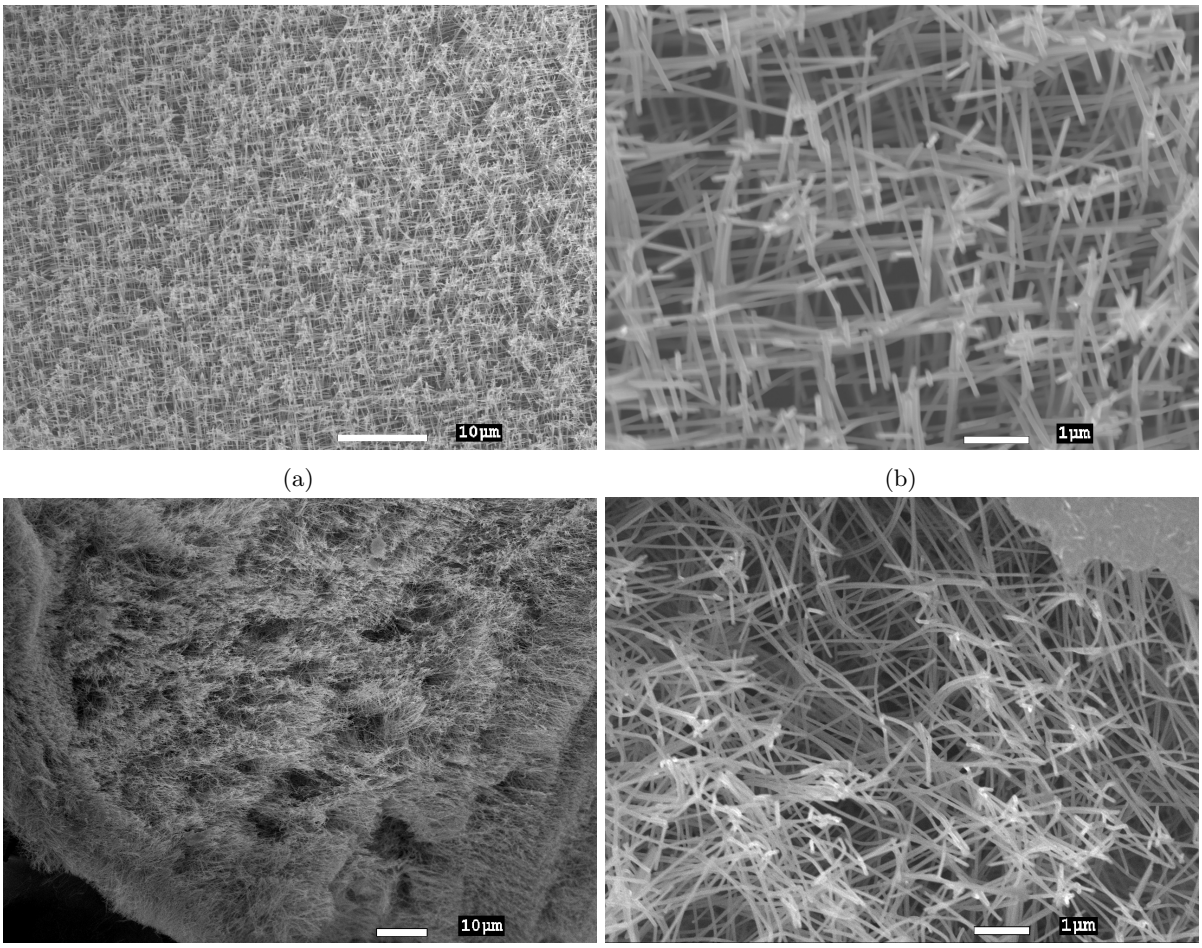

(a) (b)

(c) (d)

Figure 3.17: SEM images of interconnected continuous NiCoCu NW networks with low packing density and with (a,b) 80 nm NW diameter, and (c,d) 40 nm NW diameter.

the *2p600* series and the *8p600* series. The samples were electrodeposited with the optimised parameters and 15 mM Cu^{2+} concentration, as reported in Table 2.5.

The preparation of these sample series presented a lot of problems, both for the electrodeposition and the plasma etching. In fact, only one good sample were successfully measured. This was the sample 8p601 of the *8p600* series. However this sample showed GMR of 80% at low temperature, which might be the highest ever measured GMR ratio for interconnected nanowire networks. Unfortunately, the many attempts of reproducing this result were unsuccessful; only samples with a few percent of GMR were achieved. In the process of trying to reproduce the good results, a lot of "troubleshooting" along the entire sample preparation process were carried out, resulting in small improvements in both the electrodeposition and the plasma etching.

Morphology were investigated with FE-SEM, for continuous NiCoCu samples in the two templates. SEM images are shown in Figure 3.17. The images of the samples with nanowire diameter of 80 nm show that the networks are mechanically strong enough to maintain the features of the pores it was deposited in. many nanowires are approximately parallel, which indicates that the angles between them are kept to some extent although the packing density and number of crossing zoned are reduced to a minimum. The reduced packing density is obvious when comparing Figure 3.17b with Figure 3.3a. The images of the samples with diameters of 40 nm, however, shows that the network is not able to support itself. The samples are without a doubt interconnected, otherwise

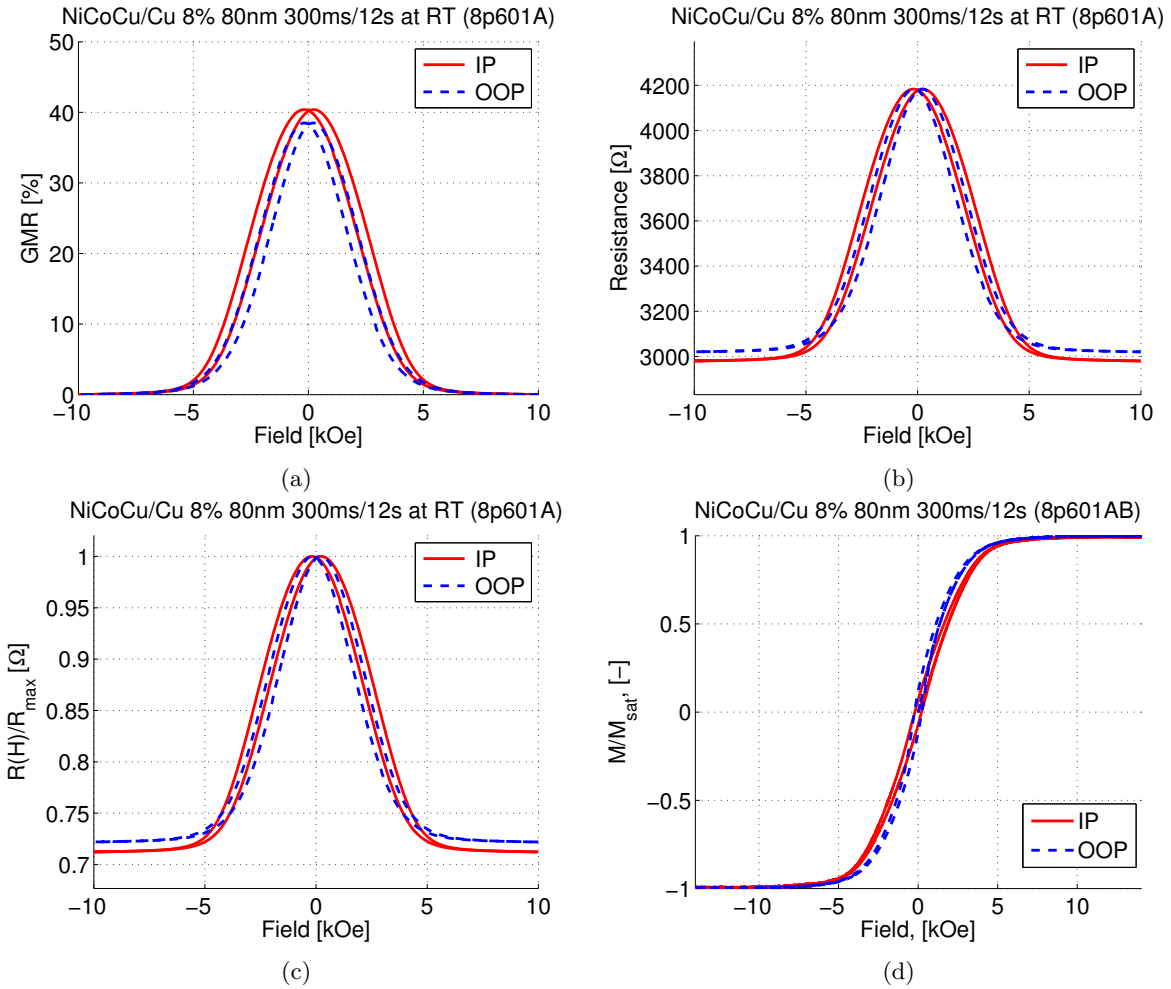

Figure 3.18: Magnetotransport and magnetisation measurements of sample 8p601A at room temperature. (a) GMR curves, (b) resistance, (c) normalised resistance versus applied field, and (d) normalised magnetisation curves.

the nanowires would not have been kept so close together. But the nanowires are obviously to thin to maintain the angles between the wires, with so few crossing points. With the high aspect ratio of the nanowires, they become very bendable and obtain a "spaghetti-like" behaviour when the PC template is removed.

3.2.1 Samples prepared from 8% 80 nm templates

As mentioned above, only one deposition was successfully performed with this template: the sample labeled 8p601. Figure 3.18 shows the room temperature magnetotransport and magnetisation measurements, in the same representation as used for the previously discussed samples. The most prominent feature from the plots is the room temperature IP GMR ratio of 40.3%, which is more than the double compared to the S602E sample discussed above. This sample was prepared with a Cu layer deposition time of 12 seconds. A very important feature about these plots is that the IP and OOP curves are almost overlapping, and saturates at approximately the same fields. Their shapes are almost identical in all the plots, which points towards a system with almost no magnetic anisotropy.

The difference between IP and OOP GMR is around 2 percentage points. This is approximately the same compared to the previous sample series, when taking into the account that the

GMR has more than doubled. The resistance of the sample is much higher than the samples previously discussed. Figure 3.18b shows a zero field resistance of around 4.2 kΩ. This points towards that the number of current channels is less in this sample than in the previous sample series, which seems reasonable due to the decreased porosity. However, the explanation for the high resistance is more complicated, because the sample had lower resistance when it was measured four weeks earlier. At that time, right after preparation, the resistance was around 2.5 kΩ, and the GMR was measured to ∼30%. During this time, the sample had been kept safely on its chip inside a protective box, and the chip had only been moved a few times to be measured. Further discussion on this matter will be addressed later in this section.

From the normalised resistance curves in Figure 3.18c the AMR can be read out as approximately 1%. The normalised hysteresis curves in Figure 3.18d are almost equal for the IP and the OOP field directions, pointing towards very low magnetic anisotropy in the sample. The coercive fields are very small and almost similar in the IP and OOP directions: 0.21 and 0.22 kOe, respectively. The remanence is very low, only ∼7% and ∼11% of M_s, for the IP and OOP field directions respectively. Relative to the S602E sample from the *20%600 15mM* series, these values represent a 61% decrease of remanence in the IP direction and a 75% decrease in the OOP direction. This points towards a high degree of antiparallelism of the F layers. Unfortunately, the samples are not directly comparable as the nanowire packing densities and diameters are different in the two. The comparison between samples of similar nanowire diameters will be carried out later in this section.

Low temperature transport measurements

The low temperature measurements were performed down to 20 K, and reported in Figure 3.19. The reason why it could not be measured at 12 K was because it was measured at another setup, where 20 K was the lowest possible temperature. Figure 3.19a shows an IP GMR of 80.0% which is an increase from the room temperature IP GMR by a factor of 2. The OOP GMR is 75%, meaning a difference in IP and OOP GMR of 5 percentage points. The approximate AMR obtained from the normalised resistance curves in Figure 3.19c is ∼1.6%. The IP and OOP curves are almost overlapping, like they also did at room temperature, meaning that the low degree of magnetic anisotropy is maintained at low temperature.

Figure 3.19d shows the IP and OOP GMR for different temperatures. The red and the blue lines belong to the first measurements performed on the sample, when the IP GMR at 12 K was around 60%. The black line correspond to the measurements done four weeks later, when the GMR had increased. The first measurements were done for seven different temperatures from 12 K up to room temperature, to investigate the temperature dependence of the GMR effect. The plot shows an approximately linear temperature dependence for the GMR. Evidently, magnons are still excited at 12 K, hence electron-magnon scattering occurs even at this low temperature. Thus, is should be expected even higher GMR ratio for lower temperatures. However, the GMR curve seems to start flattening out at 12 K, which possibly indicate the beginning of the GMR plateau, corresponding to the residual spin-flip scattering caused by spin-orbit interactions and imperfections [1, 43].

Figure 3.20a shows resistance curves of the first measurements of sample 8p601A, that is while the GMR was 30%. The different curves correspond to the different temperatures in Figure 3.19d. The most obvious change, is that the zero field resistance decreases by around 100 Ω for every 50 K decrease, which fits well with the approximately linear behaviour of $R(T)$ shown in Figure 3.20b at above ∼100 K. However the zero field resistance of the $R(H)$ curve at 12 K are only slightly less than the one at 50 K. From the $R(T)$ curve it can be seen in the inset that the resistance reaches a plateau around 25 K, before it begins to increase again for even

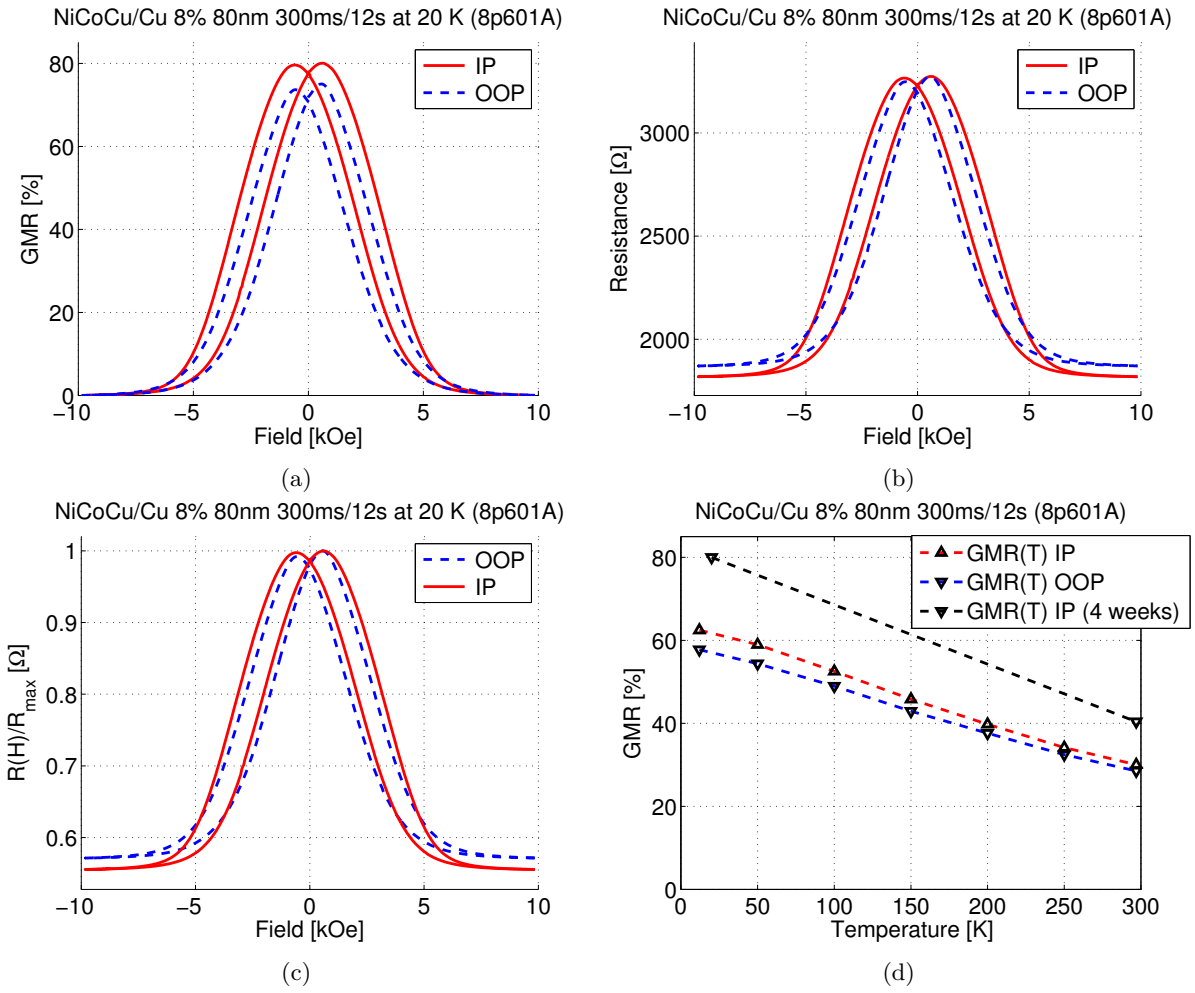

Figure 3.19: Low temperature magnetotransport measurements of sample 8p601A. (a) GMR curves, (b) resistance, (c) normalised resistance versus applied field, and (d) GMR versus temperature.

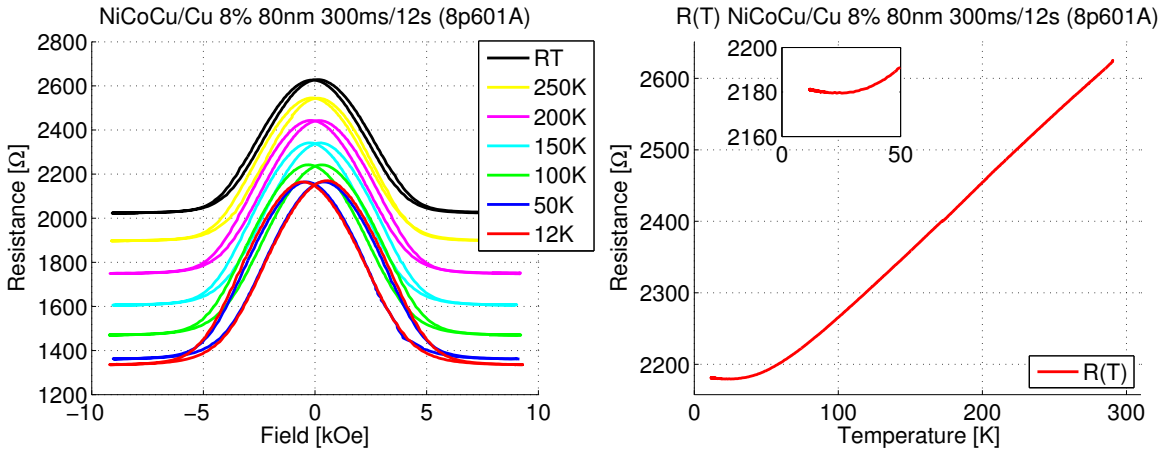

(a) (b)

Figure 3.20: (a) Resistance versus applied field for different temperatures between 12 K and room temperature for the sample 8p601A. (b) Resistance versus temperature from room temperature down to 12 K. The inset shows the same curve in the temperature range up to 50 K to clearly show the resistance plateau. The resistances in (a) and (b) both correspond to the first measurements of the sample.

lower temperatures. This behaviour is typical for weak localisation of conduction electrons in nonmagnetic thin films with thickness below a certain value [51]. This effect is a consequence of electron-electron interactions that can occur at sufficiently low temperatures. The resistance increase below ∼20 K can explain why the zero field resistances at 12 and 50 K are so similar.

The evidence of the weak localisation phenomena, points towards existence of thin film current channels in the sample. The most probable reason for this is related to the plasma etching process, where incomplete etching of the cathode thin film, could leave remains of the film of the sample. If it was a continuous film, the resistance of the sample should be very low, so this scenario seems unlikely. However, islands of remaining Cr or Cu film on small parts of the sample, seems like a more viable explanation. These islands constitutes additional current channels that can short-circuit parts of the nanowire array. If the length of these current channels are of the order of the SDL in the thin film metal, or larger, they will lead to mixing of the spin channels, thereby decreasing the GMR. Note, that the $R(T)$ curve of sample S602E in Figure 3.16 has no increase of R at low temperatures, the sample thus seems to be free of remaining thin film.

A less obvious feature about the resistance curves in Figure 3.20a is that the resistance peaks occurs at higher fields with decreasing temperature. At room temperature the resistance reaches the maximum value around ± ∼0.12 kOe, while at 12 K the peaks have been shifted to ± ∼0.55 kOe. This can be attributed to the reduced thermal energy available to contribute to flip magnetic moments.

Problems with samples from the 8% 80 nm template

As mentioned above, it was experienced a lot of problems when trying to reproduce the good results of the 8p601 sample. Apart from this single deposition, no sample showed a GMR higher than ∼1.8% at room temperature. In fact, most of the prepared samples showed no sign of spin asymmetry effects at all, and many acted almost like open circuits with resistance of several tens of kΩ. The several adjustments to the electrodeposition process were reported in Section 3.2.1. The initial attempt of trying to investigate the effects of reduced amount of crossing zones was therefore discarded, and replaced with the investigation of why the samples worked so badly.

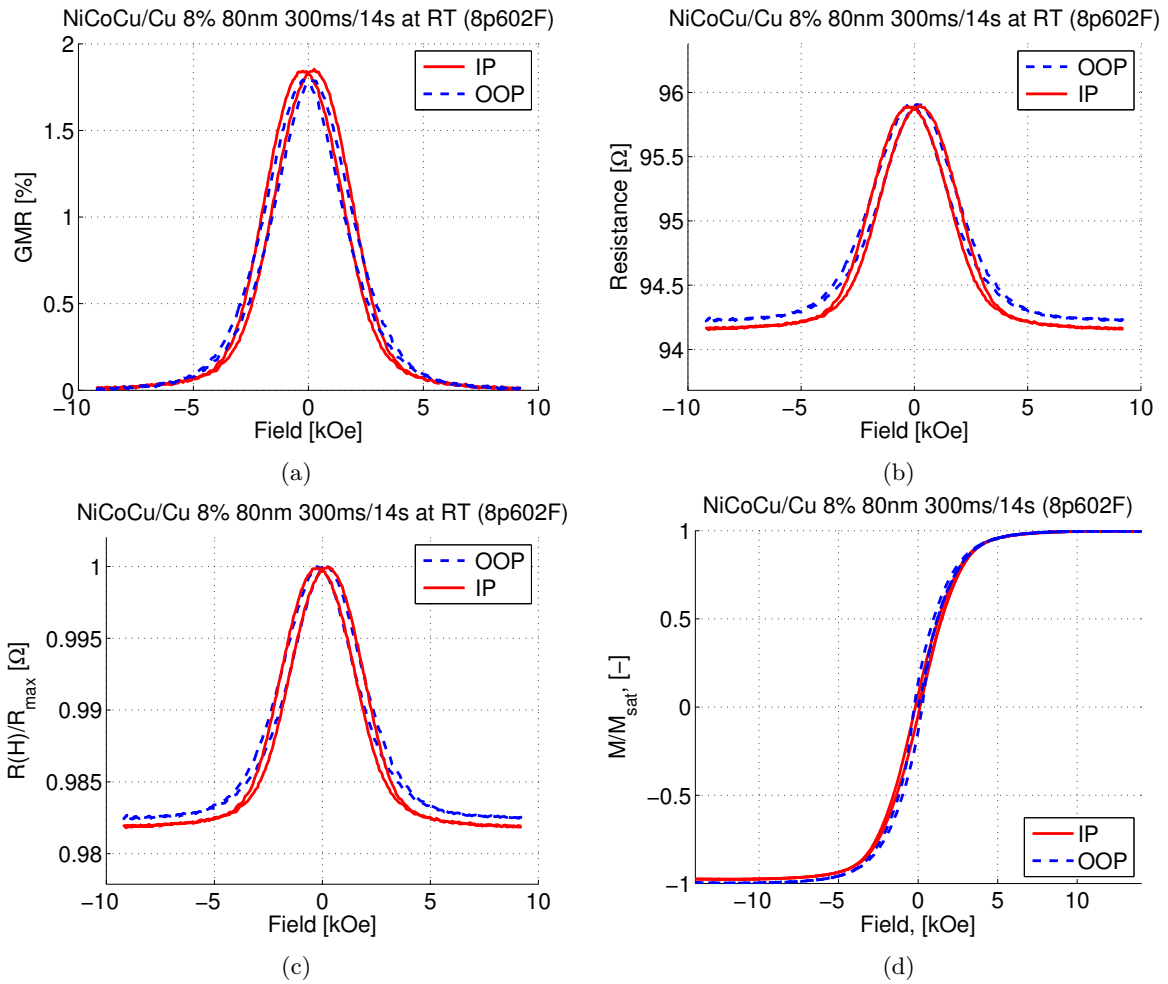

Figure 3.21: Room temperature magnetotransport measurements of sample 8p602E. (a) GMR, (b) resistance, (c) normalised resistance versus applied field, and (d) normalised magnetisation curves.

A few samples showed GMR effect to some extent. The best of these was the sample 8p602F, which had a GMR measured to ∼1.8%, plotted in Figure 3.21a. This sample was prepared with a Cu layer deposition time of 14 seconds, thus differing from the best sample (8p601A) where this parameter was 12 seconds. Another difference is the much lower resistance of the current sample; ∼96 Ω at zero field, as shown in Figure 3.21b. Additionally, The approximate AMR effect is very low; ∼0.1%, extracted from Figure 3.21c. From the normalised magnetisation curves in Figure 3.21d, the remanence is around 7% and 15% of M_s in the IP and OOP field direction, respectively. The coercive fields are 0.12 and 0.25 kOe in the IP and OOP directions, respectively. The magnetic anisotropy is very low, as the two magnetisation curves saturates at almost exactly equal fields. This is also expressed by the almost similar shapes of the IP and OOP curves of all the other plots in Figure 3.21.

The values are very similar to the good 8p601A sample. This is good news and can mean that there is no problem with the electrodeposition. After all GMR effect is observed, and this is a sign of good quality of the deposited layers. Further, the very low remanence points towards a high degree of antiparallelism between the F layers, very similar to the sample showing 40% GMR at room temperature.

The low temperature transport measurements of sample 8p602E are shown in Figure 3.22. The shapes of the curves corresponding to the IP and OOP field directions are still very similar. The IP GMR is 2.9% which means that it has only increased by a factor of 1.6, which is less that expected in the low temperature limit. The approximate AMR found from the normalised resistance curves in Figure 3.22c is ∼0.2% which is the double of the room temperature value. Although the AMR is very low, the behaviour is similar to the good samples. The resistance versus temperature behaviour plotted in Figure 3.22d shows that the temperature dependence of the resistance of the sample is approximately linear above ∼100 K, similar as for the previously discussed samples. The resistance reaches a minimum of 84.7 Ω at around 45 K, which may be the residual resistance of the sample. This is around 12% less than the room temperature resistance.

However, at even lower temperatures the resistance starts to increase again. As discussed in the previous section, this is a sign of the weak localisation effect, which can occur in thin films at low temperatures. This discovery is very important, because it can explain the low GMR and AMR effects in the samples. Remains of the cathode thin film layer creates additional current channels. These conduct in parallel to the multilayered nanowires, and alters the total resistance of the sample. Consequently this decreases the GMR effect, as there is an amount of the current which is unaffected by the magnetic field (at least when neglecting the negative MR of nonmagnetic metals with a H^2 dependence, because it is so small). With this in mind, it is not possible to say anything about the actual quality of the sample. The sample may be perfect, but with the apparent remaining metal thin film, the GMR effect will always be suppressed.

These results lead to a discussion about the plasma etching method for removing parts of the Cu/Cr cathode thin film. The plasma etching technique seems to be very brutal on the sample. In the process of finding the optimal plasma etching time for the different templates as reported in Table 2.11, it was discovered that the samples quickly became destroyed if the etching was kept going longer than the optimal time. If the plasma etching process was stopped before the optimal time, it was clearly visible remains of the cathode thin film on the sample, and the resistance was very low. Thus the samples are very sensitive to the etching time, and this has caused a lot of problems. For the discussion of the *8p600* series it seems likely that many of the samples showing low GMR effect still have remaining parts of the thin film left on them.

3.2.2 Samples prepared from 2% 40 nm templates

The sample series *2p600*, where prepared with the parameters reported in Table 2.5. In contrast to the 8% 80 nm template, no good samples were successfully prepared and measured with the 2% 40 nm template. The problems experienced with this template was similar to those of the 8% 80 nm template; low or no GMR effect, and some samples with resistance up to several hundred kΩ. Like for the bad 8% 80 nm sample, a sample from the 2% 40 nm template with very low GMR ratio was investigated to find out why they worked so badly.

Problems with the *2p600* series

The magnetotransport properties of one sample named 2p601F was performed in room temperature and the resulting plots are shown in Figure 3.23. The IP GMR is less than 1%, and the AMR is less than 0.1%. It is interesting that the GMR curve corresponding to the OOP direction shows saturation at lower fields than in the IP direction. This has not been the case in any of the previously discussed samples. Indeed this is expected, as the demagnetising field in the IP direction of the NiCoCu layer, should be higher for a diameter of 40 nm than of 80 nm. This is also shown at the normalised magnetisation curves in Figure 3.23d, where the OOP curve reaches saturation at lower fields than the IP curve. However this is the first measurement discussed

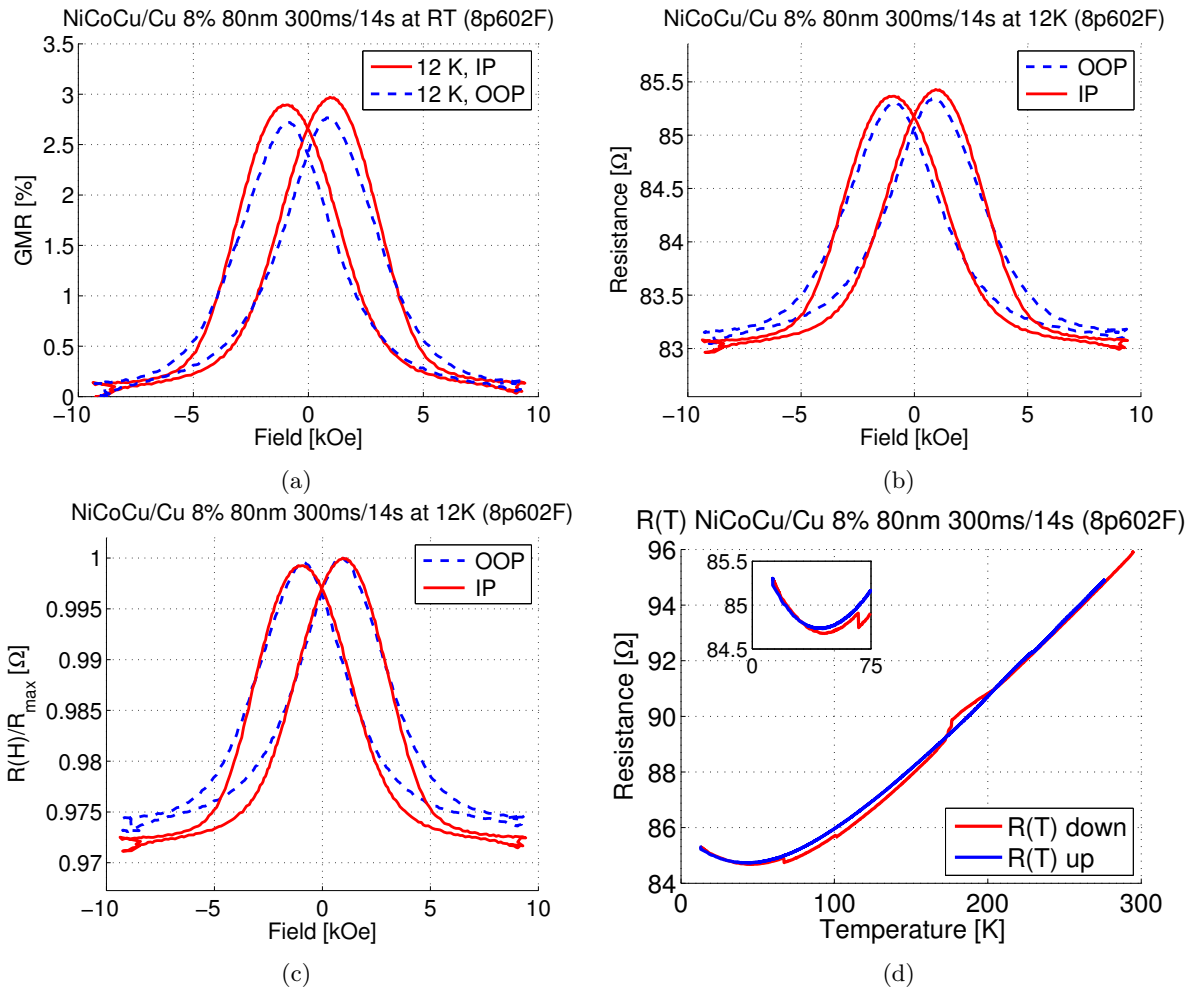

Figure 3.22: Low temperature magnetotransport measurements of sample 8p602F. (a) GMR, (b) resistance, (c) normalised resistance curves versus applied field, and (d) resistance versus temperature at zero field measured upon cooling from room temperature down to 12 K, and upon heating back to room temperature. The inset shows the same curves in the temperature range of 0 to 75 K.

where this behaviour is shown in both the magnetisation plots and in the magnetotransport plots. For the samples with higher nanowire packing density, the IP and OOP curves were inverted in the magnetotransport plots. The dipolar interactions between the nanowires in the 2% 40 nm sample should be lower than in the other samples. This may indicate that it is the dipolar interactions between the nanowires that causes the contradicting behaviour in the samples with higher nanowire packing densities.

The remanent magnetisations are very low: 5% and 13% of M_s in the IP and OOP directions respectively. This is similar to the samples discussed in the previous section about the *8p600* samples. This points towards a high degree of antiparallelism at zero field also in this sample. However the magnetic anisotropy is slightly higher than some of the previous samples, as the samples as higher saturation field in the IP direction than in the OOP direction. However the anisotropy is still very low. The coercive fields are approximately 0.13 and 0.21 kOe for the IP and OOP directions respectively.

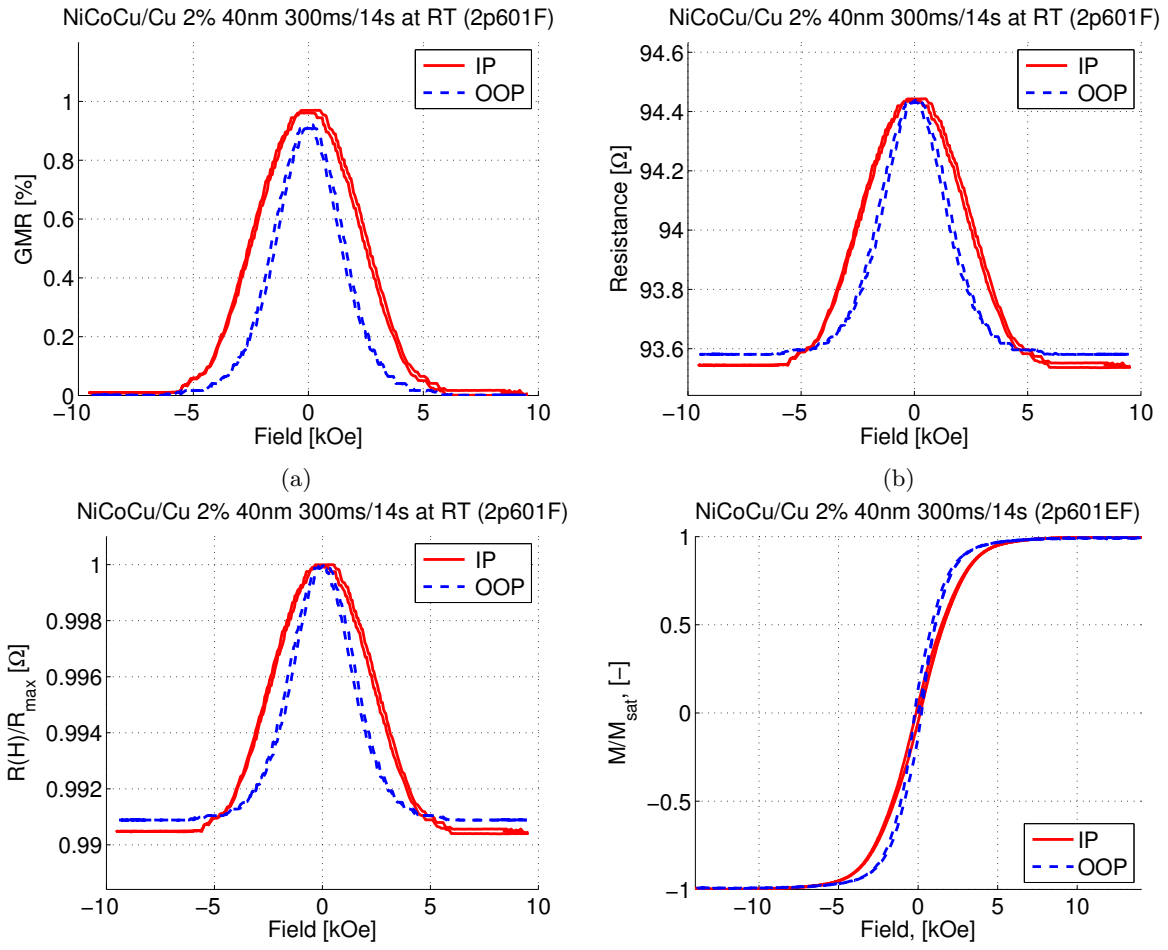

Figure 3.23: Room temperature magnetotransport measurements of sample 2p601F. (a) GMR, (b) resistance, (c) normalised resistance versus applied field, and (d) normalised magnetisation curves.

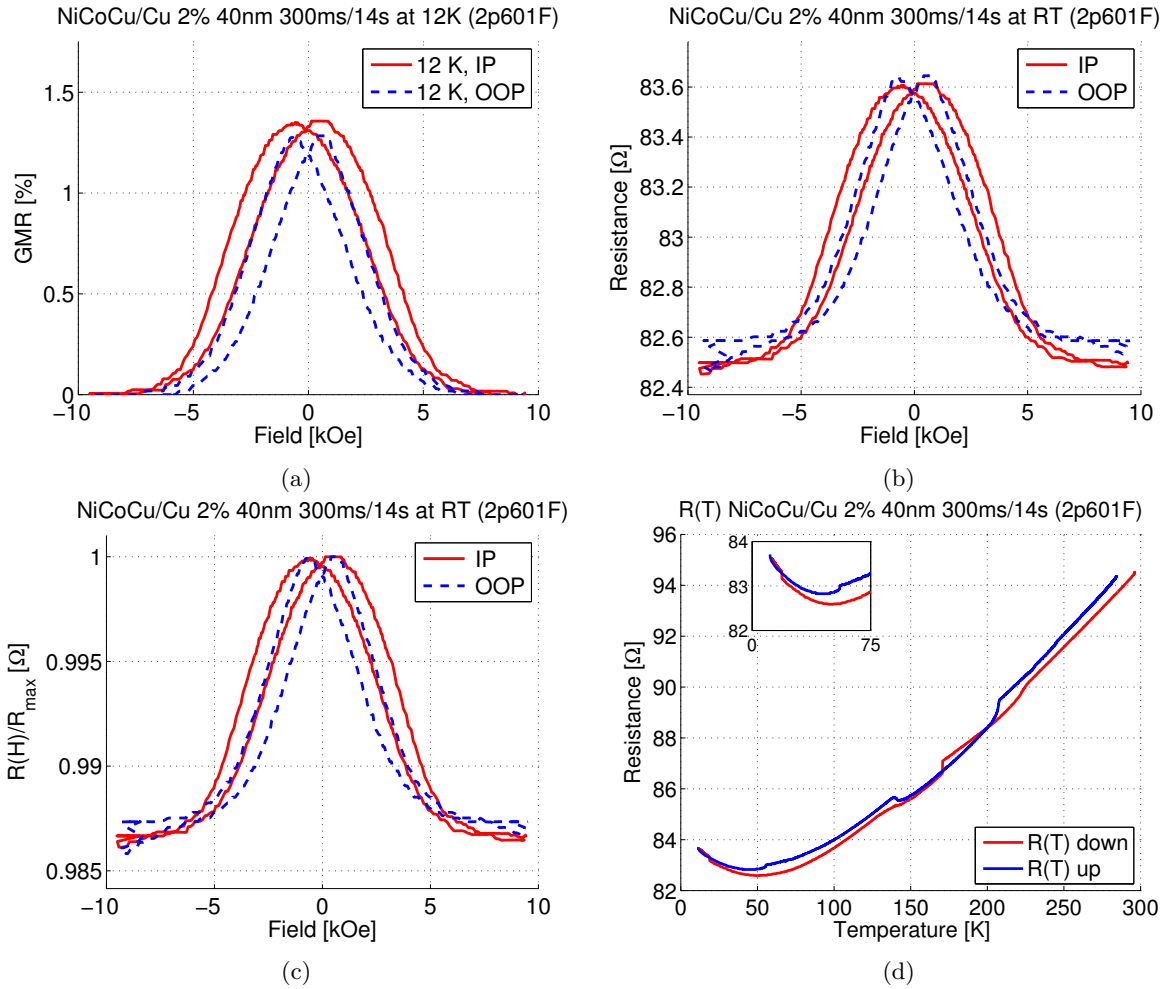

Figure 3.24: Low temperature magnetotransport measurements of sample 2p601F. (a) GMR, (b) resistance, (c) normalised resistance curves versus applied field, and (d) resistance versus temperature at zero field measured upon cooling from room temperature down to 12 K, and upon heating back to room temperature. The inset shows the same curves in the temperature range of 0 to 75 K.

Low temperature transport measurements

Low temperature measurements were performed on the same sample and the results are plotted in Figure 3.24. The IP GMR at 12 K shown in Figure 3.24a is only ∼1.3%. This increase correspond to a factor of 1.3 compared with the room temperature IP GMR. From Figure 3.24c, the AMR is approximately 0.1%; slightly larger than the room temperature value.

Figure 3.24d shows the resistance versus temperature both upon cooling down from room temperature, and upon heating up to room temperature. The curve is approximately linear above ∼150 K, but contains many steps. This steps may indicate changes in the samples as a result of thermal contraction (expansion) during the cooling (heating) process. A possibility is that the nanowires may have broken and been torn apart inside the template at an earlier step in the process. And when the sample then contracts (expands) with the temperature, these nanowires may connect (detach) again, causing sudden steps in the $R(T)$ curve. If this is the case, the samples prepared from the low porosity templates, may be more fragile than initially assumed. This can also explain all the samples with very high resistances. Below ∼150 K the curve starts to flatten out as the resistance approaches the residual resistance of the sample.

The resistance reaches a minimum of 82.6 Ω at around 50 K, which is ∼13% less than the room temperature resistance. At even lower temperature the resistance starts increasing again and reaches 83.7 Ω at 12 K. As discussed for the previous sample, this resistance increase at low temperature is typical for the phenomenon of weak localisation in conducting thin films. This points towards remaining thin film left on the sample after the plasma etching process, making additional current channels that results in a decreased GMR effect.

The evidence of thin film weak localisation phenomenon is sufficient to explain why the samples show so small GMR effect. Also, the effect increases so little at 12 K relative to room temperature. This can be explained by additional current channels provided by the remaining thin films, because they do not contribute to any spin-asymmetry. Furthermore, the sudden steps in the $R(T)$ curve imply that some of the nanowires may be broken and that the thermal expansion or contraction may affect the number of nanowires in contact. After all the resistance of the sample is expected to change with changing number of current channels. The fact that the steps does not occur at the temperatures during the cooling and the heating processes, strengthens this explanation, as the thermal expansion of polymers is not necessarily completely reversible and very different from that of metals.

3.3 Influence of NiCoCu layer thickness on magnetoresistance

According to [1], the GMR effect varies with $1/t_F$ where t_F is the thickness of the NiCoCu layer, in the limit where $t_F \gg l_{sf}^F$. The SDL of the NiCoCu layer is unknown, and the process is controlled by the deposition time for each layer, rather than the thickness. However, it can be expected that the deposition rate is rather linear with respect to the deposition time, at least when the pulse is sufficiently long [43]. Thus it is a fair assumption that the deposition time of the NiCoCu layer is approximately proportional to t_F. The GMR effect in samples with increasing NiCoCu layer deposition time, should therefore follow a dependency corresponding to $1/t_F$.

To investigate if this was the case, the *'F 20%'* series was prepared, according to Table 2.6. Figure 3.25 collects the results of the magnetotransport measurements. The IP GMR curves and the OOP GMR curves for the different samples are separated in Figure 3.25a and 3.25b to help distinguish the different curves. Evidently both the IP and OOP GMR decrease with increasing NiCoCu layer deposition time. The maxima of the curves shifts to higher field values as the NiCoCu layer deposition time increases, both in IP and OOP. This points towards that the increased t_F influences the dipolar interactions in such a way that the magnetic layers reaches the highest degree of antiparallelism for higher fields that earlier. It is also worth mentioning that the difference between the IP and OOP GMR increases with increasing NiCoCu layer deposition time. In the sample with 300 milliseconds of NiCoCu layer deposition time this difference is around 1 percentage point, while for the 3 second sample the difference is more than 2 percentage points. This increase is related to the AMR, and it makes sense that the AMR increases as the amount of the NiCoCu material increases relative to the amount of Cu.

The IP and OOP GMR for the *'F 20%'* series are plotted in Figure 3.25c. Evidently, the IP and OOP GMR decrease with increasing NiCoCu layer deposition time, and the evolution of the AMR, shown in the inset, is almost linear from this representation. The AMR actually increases to around 2% which is above the value of 1.7% for the corresponding continuous sample. Note that the number of bilayers, and thus the number of NiCoCu/Cu interfaces, is different for the different samples. Due to the close to linear increase of the AMR with increasing NiCoCu layer thickness, the number of interfaces does not seem to significantly contribute to the AMR effect. Thus, it can be pointed out that the AMR effect is dominated by the amount of NiCoCu

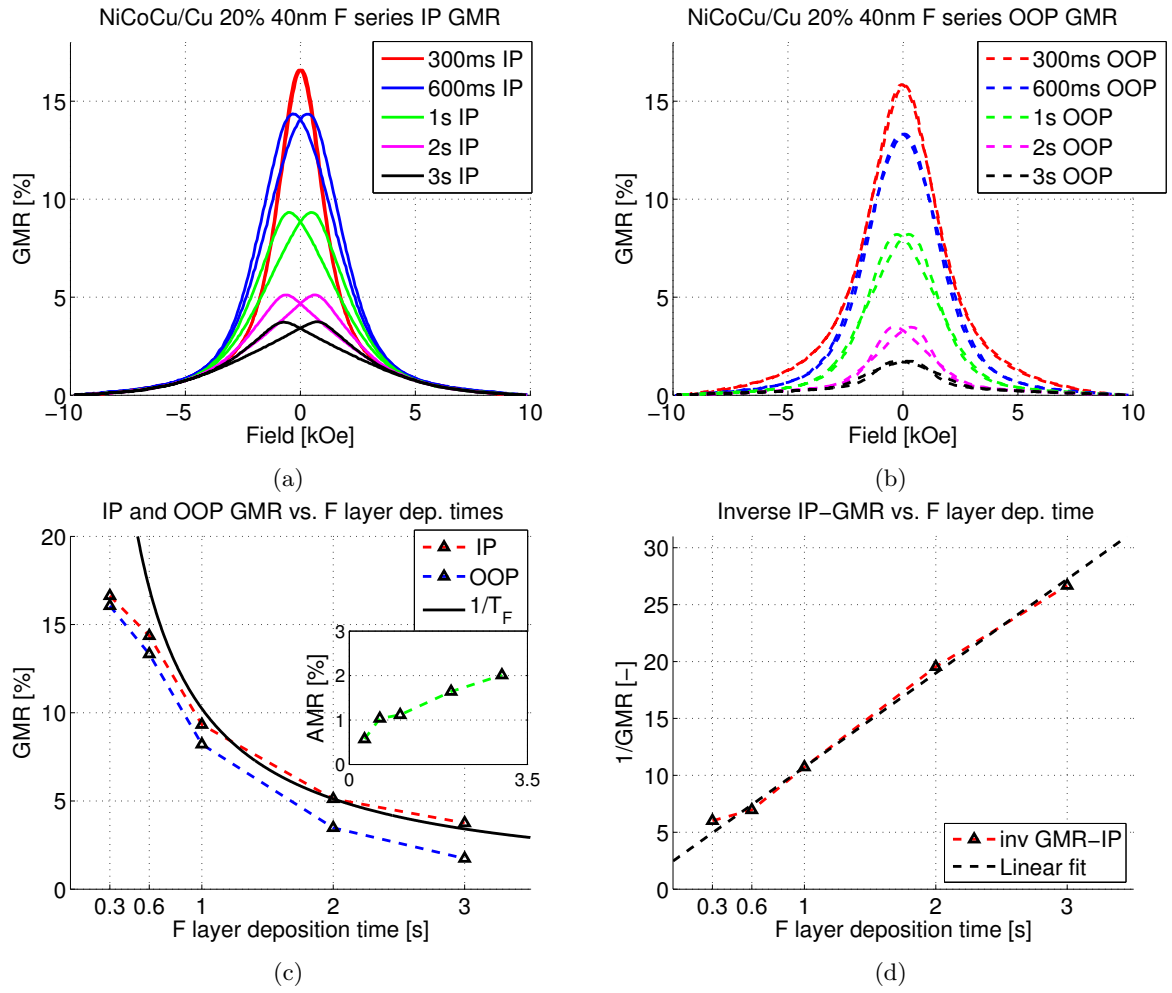

Figure 3.25: Room temperature magnetotransport measurements of the *'F 20%'* series. (a) IP GMR curves, (b) OOP GMR curves, (c) IP and OOP GMR as a function of the F layer deposition time, for all the samples in the series. The solid black line, represents a $1/T_F$ fit of the IP GMR data, where T_F is the F layer deposition time. The inset shows the AMR$\approx$GMR$_{IP}-$GMR$_{OOP}$. (d) Inverse IP-GMR based on the same values as in (c), with a dashed black line corresponding to the linear fit of the data corresponding to 1, 2 and 3 seconds of F layer deposition time.

in the multilayers.

The IP curve has been fitted with a $1/T_F$ curve in black, where T_F is the NiCoCu layer deposition time. The curve matches the IP GMR of the samples with NiCoCu layer deposition time of one second or longer. This fits nicely with the predictions from the VF model in the limit where $t_F \gg l_{sf}^F$ and $t_N \ll l_{sf}^N$, where the GMR is supposed to be inversely proportional to t_F, as shown in Equation 1.55. The fit leaves the IP GMR curve somewhere in between 0.6 and 1 second, which possibly represents the transition between the limits where $t_F \ll l_{sf}$ and $t_F \gg l_{sf}$.

However, Equation 1.55 also includes p, which corresponds to the degree of antiparallelism. This value may indeed also change for different t_F, and influence the trend. Based on the remanence of the samples as a function of the NiCoCu deposition time, shown in Figure 3.26 and 3.27, it seems as the degree of antiparallelism decrease as a function of the NiCoCu layer deposition time, because the remanence increases. This trend is clear for the samples up to 1 second of NiCoCu layer deposition time, but the remanence then seems to stay more or less constant. Hence, p decreases with the first samples up to 1 second, and then stay approximately constant.

This is further confirmed by Figure 3.25d where $1/GMR$ is plotted versus the NiCoCu layer deposition time. Here the data corresponding to 1 - 3 seconds of NiCoCu deposition time is fitted linearly. The deviation from the linear fit is not so clear for the samples with shorter NiCoCu layer deposition times. In fact, the sample deposited with 0.6 seconds is almost on the linear curve. However, there is a deviation from the linear trend for the sample with NiCoCu layers deposited with 0.3 second pulses, but the deviation is rather small. Possibly, the l_{sf}^F is a little shorter than estimated from Figure 3.25c, and closer to the length corresponding to the thickness of the NiCoCu layer deposited in 0.6 seconds. Additionally, it was shown in Figure 2.4 that the deposition current peaked every time the -1.0 V pulse started, before reaching a constant plateau after some milliseconds. If the increased initial current is due to increased deposition of NiCoCu or to parasitic electrochemical reactions is unknown, but if the former is the case, it can mean that t_F is underestimated for short pulses. For this discussion it means that the value corresponding to the 0.3 second NiCoCu deposition time should be shifted slightly to the right and thus closer to the linear fit. If this is the case it point towards that t_F is larger than l_{sf} even for a NiCoCu deposition time of 0.3 seconds. In similar studies, such as [10], the deviation from the linear trend is very clear at sufficiently short t_F, and it was estimated that $10 < l_{sf}^F < 34$ nm. Indeed, this may point towards that the NiCoCu layers in this work is thicker than 34 nm.

If it turns out that even the thinnest NiCoCu layers in this work are thicker than l_{sf}^F, it means that it should be possible to enhance the GMR a lot by decreasing the layer thickness. Furthermore, samples with shorter NiCoCu layer deposition time were indeed thoroughly tested in this work, without success. Maybe there is a problem with with the electrodeposition process in the PC templates with pores of this low diameters. Another study on NiCoCu/Cu multilayered nanowires have reported problems with PC membranes with pore diameter of 30 nm [46]. The samples showed much lower GMR effect than samples deposited in alumina membranes under the same deposition parameters. The study explained that this could possibly be a consequence of the hydrophobic nature of the PC membrane. The template had been treated with a wetting agent by the manufacturer, but it was considered that the reactant had problems with diffusing through the narrow pores, resulting in poor quality of deposition. High GMR effect requires complete layers which are as smooth as possible, and low reactant diffusion could certainly pose a threat to achieve this. If this is the case, a solution for future studies could be to use templates with larger pore diameter and reduced porosity. However, this may influence the magnetic properties due to formation of grains and/or magnetic domains when the aspect ratio decrease.

In this work, the thickness of the layers are, as mentioned earlier, unknown at this stage, but investigation with transmission electron microscopy (TEM) should make it possible to see and measure the thickness of the individual layers [1, 43]. If it turns out that t_F and t_N are uniform throughout the entire length of the nanowire, the deposition rate in layer thickness per second could easily be found. When t_F and t_N are known, l_{sf}^F and l_{sf}^N can be determined from Equation 1.53, and furthermore the β and γ spin asymmetry coefficients through Equation 1.55.

Figure 3.26 and 3.27 shows the normalised resistance curves and the normalised magnetisation curves for all the samples in the *'F 20%'* series. The plots corresponding to the same sample are put besides each other to facilitate easy comparison. The plots are sorted from low to high NiCoCu layer deposition time. The normalised resistance curves show that the absolute value of the applied field corresponding to the maximum resistance, tends to shift towards higher values for the samples with thicker NiCoCu layer. In other words, the highest degree of antiparallelism, or randomness, in the magnetisations of the NiCoCu layers requires higher fields for samples with thicker NiCoCu layers. However, this field is always closer to zero field than the coercive field. This applies for both IP and OOP field directions. Hence, the magnetisation corresponding to the maximum resistance will be somewhere between the remanent magnetisation and zero.

Furthermore, the normalised resistance plots directly give the approximate AMR of the samples. Clearly, the AMR increases with increasing t_F; from less than 1% in the sample lowest t_F, to almost 2% in the sample with highest t_F. This trend is expected as the amount of ferromagnetic NiCo increases relative to nonmagnetic Cu in the samples with increasing t_F.

The normalised magnetisation hysteresis curves in the same figure, shows that the saturation fields in the IP and OOP field directions, changes with t_F. The IP saturation field shifts to higher values, while the OOP saturation shifts to lower values. Hence, the OOP direction is increasingly favoured as an easy magnetisation axis for increasing t_F. Oppositely, the IP directing becomes more and more the hard axis for increasing t_F. This can be explained by the shape anisotropy that favours the magnetisation along the wire axis when the t_F becomes sufficiently large, and the and the increased dipolar interactions between the NiCoCu layers, according to Figure 1.7. Hence, the demagnetising factors moves closer to the limiting case of the single domain long needle from Table 1.2, which means higher demagnetising fields when the F layer is magnetised in the IP direction than in the OOP direction. These results are interesting, because all the samples in this work have had lower saturation field in the OOP direction. As discussed in Section 1.1.2, the initial assumption was to expect samples with IP easy magnetisation axis. This assumption was based on another assumption that the c/a ratio of the cylindrical F layer was much less than one. Hence, resulting demagnetising factors favouring magnetisation in the IP direction. These results contradicts the hypothesis, as the samples are about magnetically isotropic, or favour magnetisation in the OOP direction. Maybe the F layers are thicker than expected. After all, there have been several instances were the template has overfilled unexpectedly during electrodeposition. A higher deposition rate than presumed resulting in thicker F layers, could explain the overfilling and the easy OOP magnetisation axis. However, there is not just the demagnetising field of the F layers that influences the samples. The interconnected array of multilayers makes up a very complicated system, with complicated magnetostatic interactions between the nanowires and the crossing zone effects need to be taken into account.

Furthermore, The coercive fields increase with increasing t_F, in both IP and OOP direction; from approximately 0.5 to 0.8 kOe, and 0.6 to 0.8 kOe, in the IP and OOP field directions respectively. The remanent magnetisations in the IP and OOP directions increase from around

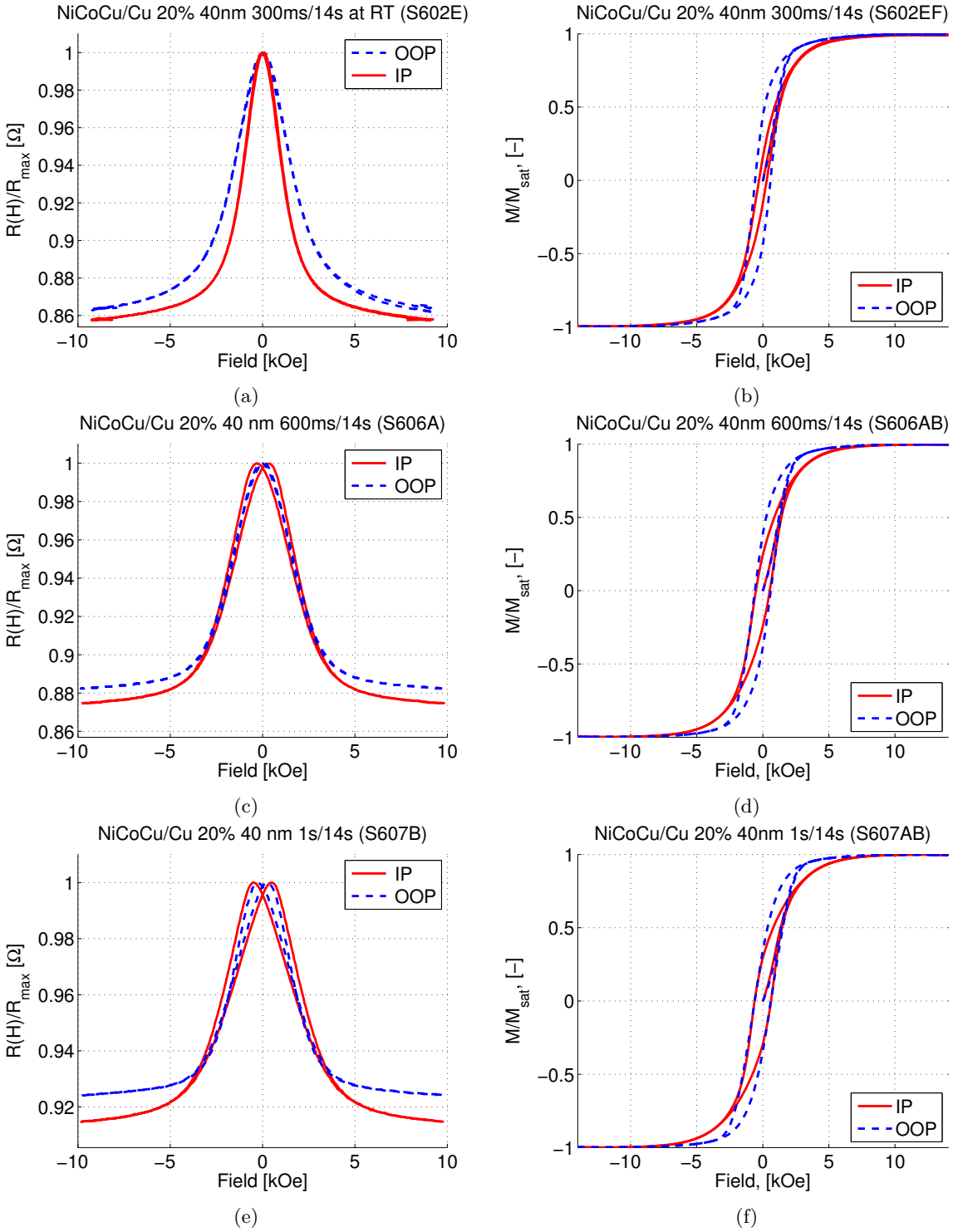

Figure 3.26: Normalised resistance versus applied field (left) and normalised magnetisation curves (right) for the samples in the *'F 20%'* series with (a,b) 300 ms, (c,d) 600 ms, (e,f) 1 s F layer deposition time. Measured at room temperature.

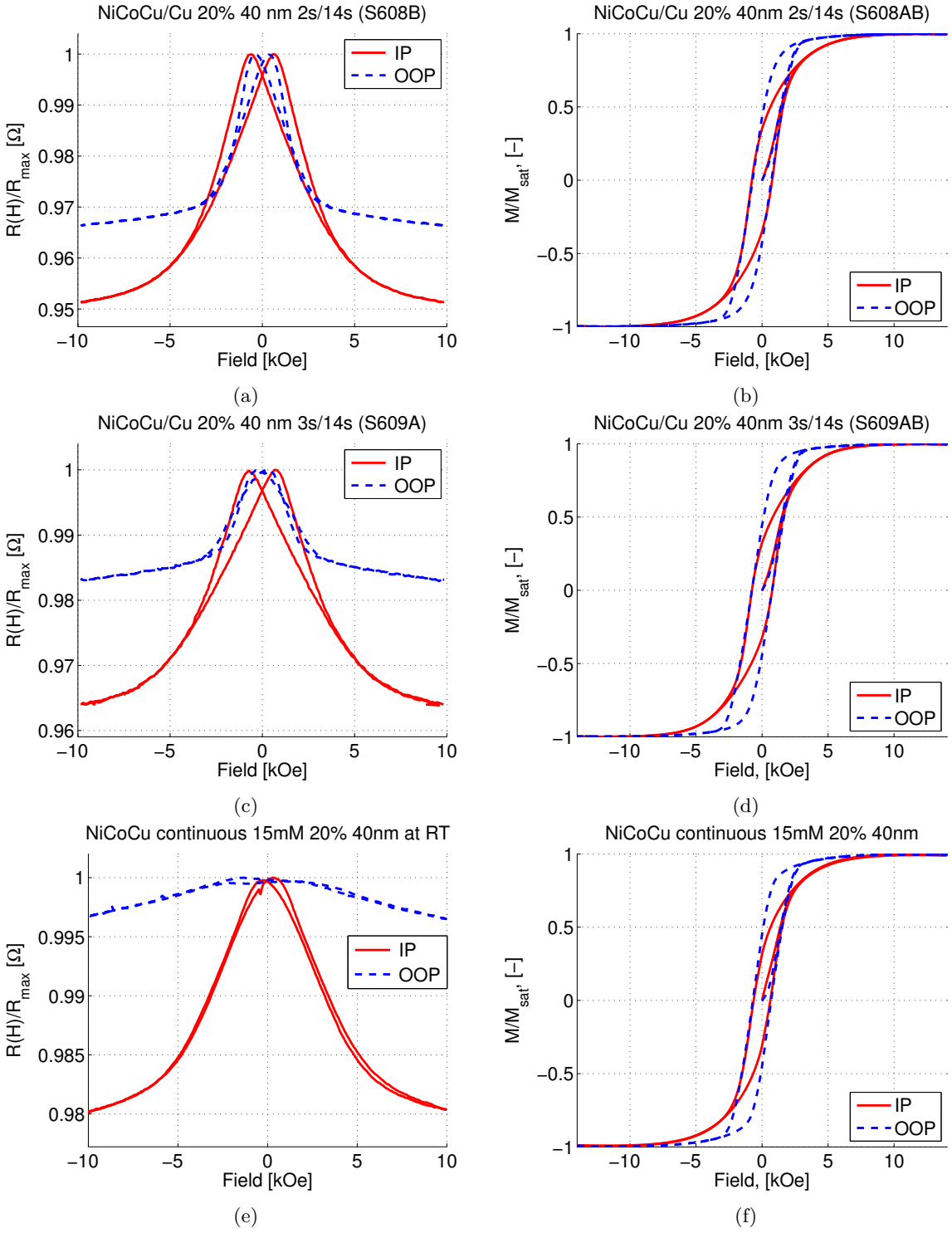

Figure 3.27: Normalised resistance versus applied field (left) and normalised magnetisation curves (right) for the samples in the *'F 20%'* series with (a,b) 2 s, (c,d) 3 s F layer deposition time. (e,f) shows similar plots for the sample of continuous NiCoCu nanowires. Measured at room temperature.

24% to 35%, and 39% to 44% of M_s, respectively. Another feature of the magnetisation curves is that the tilt of the curves increases slightly with increasing t_F. This can be explained by increasing magnetostatic interactions between different nanowires in the array, due to increased relative amount of ferromagnetic Ni-Co in the sample [14].

The normalised resistance curves of the continuous samples shown in Figure 3.27e, shows that the approximate AMR is around 1.7% which is actually less than shown for the multilayered sample with the longest NiCoCu layer deposition time. However, the curves in Figure 3.27e are not really saturated at the maximum applied field, and thus the AMR is underestimated. The normalised magnetisation curves in Figure 3.27f cannot be separated from the one in Figure 3.27d for the multilayered sample with the longest NiCoCu layer deposition time. It thus seems like the magnetic properties of this multilayered sample is similar to the ones of the continuous wires, and is not influenced by the relatively thin Cu layers.

3.4 Influence of systems with lower saturation fields on the magnetoresistance

To attempt and reduce the saturation fields of the system, and thereby obtain sharper GMR curves, samples with increased nanowire diameter, and trilayer systems were prepared.

Multilayered nanowire network with increased nanowire diameter

Templates with pores of 105 nm and a porosity of 20% were used to prepare multilayered nanowire samples. Since the porosity is equal to that of the 20% 40 nm template and the diameter is larger, the pore packing density is lower in the 105 nm template. This results in fewer crossing points between the nanowires. Thus it is expected that the crossing zone effect on the GMR will be less for these samples than for those of the 20% 40 nm. Consequently the GMR effect should be higher. Furthermore, as the nanowire diameter is increased, the ferromagnetic layers will be closer to the limiting case of ferromagnetic thin films. Then it follows that the demagnetising field in the IP direction will be less and higher in the OOP direction, as explained in Section 1.1.2. Thus the saturation field should decrease in the IP direction and increase in the OOP direction, leading to a sharper $R^{IP}(H)$ curve and a wider $R^{OOP}(H)$ curve.

Figure 3.28b shows a high GMR effect of $\sim$17% IP, and surprisingly almost the same in the OOP direction. Thus the AMR is low in this sample, which also can be seen in the very small difference, $< 0.1\%$ in the resistance curves in Figure 3.28b and 3.28c. However, the the normalised hysteresis curves in Figure 3.28d are almost equal, hence the magnetic anisotropy of the sample must be almost zero. The saturation fields are approximately equal, not lower for the IP direction as expected. According to the model discussed in Section 1.1.4 this points towards a relative aspect ratios of the NiCoCu and Cu layers corresponding to an effective demagnetising field $H_{eff} = 0$, which is postulated to be optimal for GMR. Similar to the other samples with 105 nm nanowire diameter, the coercive fields are almost zero in both IP and OOP directions. The remanence is around $0.17M_s$ in the IP direction and $0.24M_s$ in the OOP direction, which means that the degree of antiparallel alignment between the NiCoCu layers is not as high as the highest reported in this work. Neither has the same procedure to optimise samples from this template been carried out. This template thus seems promising for further studies on interconnected multilayered nanowire networks.

Interconnected trilayer network

Due to the limited time for this thesis work, not much investigation into the trilayer system has been carried out. However, preliminary results of one sample of interconnected trilayers

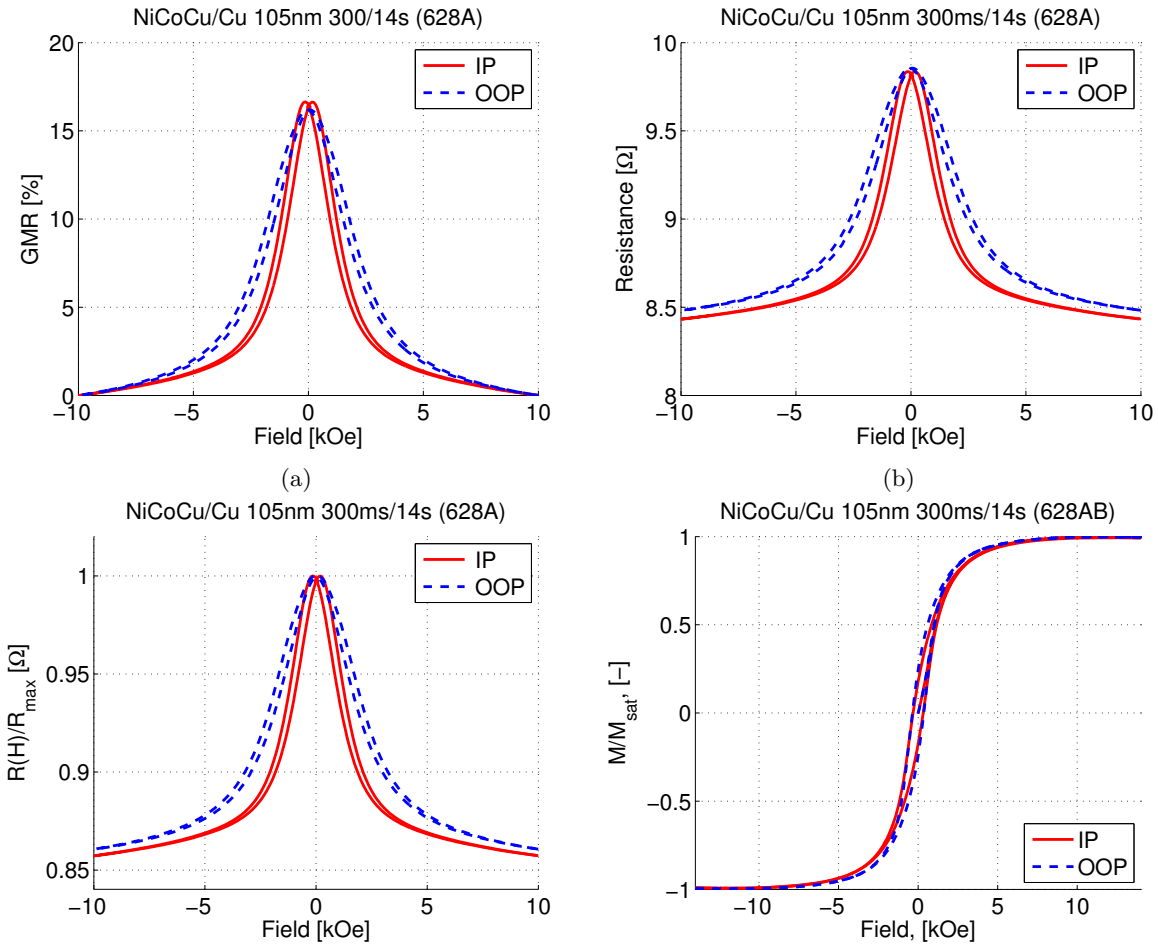

Figure 3.28: Room temperature magnetotransport measurements of sample 628A. (a) GMR, (b) resistance, (c) normalised resistance versus applied field, and (d) normalised magnetisation curves.

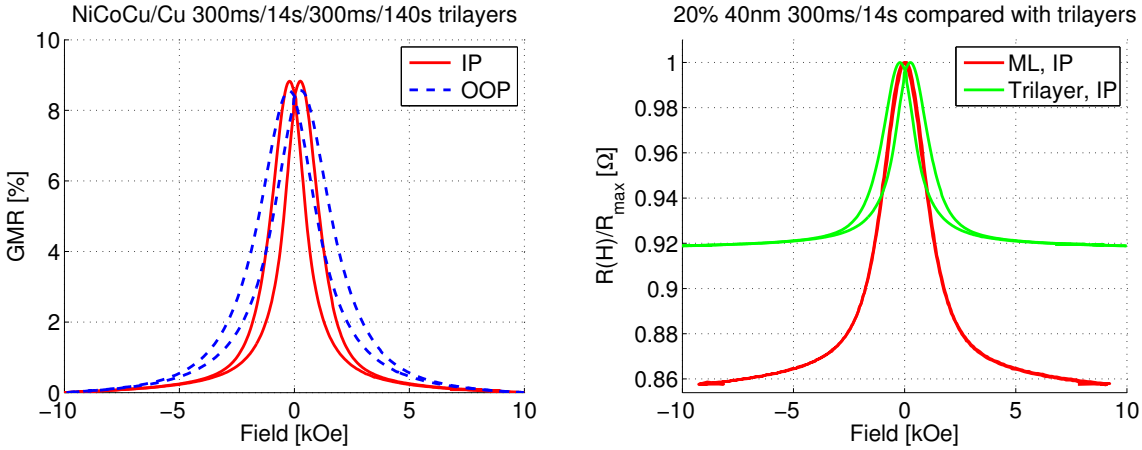

(a) (b)

Figure 3.29: (a) IP and OOP GMR curves for the interconnected trilayer sample. (b) Comparison of the normalised IP resistance versus applied field for a ML and a trilayer sample with corresponding deposition parameters.

were successfully prepared and performed magnetotransport measurements on.As shown in Figure 3.29a, an IP GMR of 8.8% was obtained for the trilayer system. The OOP GMR was almost similar to the IP GMR due to the low AMR effect. This was expected as most of the nanowire network should consist of Cu. The IP GMR curve is sharper than the OOP curve, but not as much as expected. When compared to the corresponding multilayer sample ($S602E$), meaning the sample prepared from the same electrolyte in the same template, the normalised resistance curves do not show much difference. This is shown in Figure 3.29b. The saturation field of the trilayer sample is only slightly less, and in fact the curves matches each other in the range close to zero field. The peaks in the trilayer resistance curves are further shifted apart than in the case of the multilayer sample. It was expected a more prominent difference in the sharpness of the GMR curves than observed. Possibly the the absence of this difference could be a consequence of the suspicion which have already been discussed, that the NiCoCu layers are much thicker than anticipated. In earlier studies, such as that of [43], t_F was much less than the nanowire diameter. In this study the GMR effect in the trilayers decreased by a factor of 4 compared to the multilayers, but the saturation field decreased from approximately 3 kOe to 1 kOe, resulting in a sharp GMR curve.

Summary of Chapter 3

In this chapter it has been shown that interconnected multilayered nanowire networks of NiCoCu/Cu electrodeposited in PC templates from a single electrolyte, is suitable for studying the CPP-GMR effect. The synthesis process has been optimised from the basis of earlier studies on NiCoCu/Cu multilayered nanowire arrays [10]. The GMR effect was observed to vary with the Cu^{2+} concentration in the electrolyte, and 15 mM Cu^{2+} was decided as a compromise between the deposition rate of the Cu layer and the Cu impurity concentration in the NiCoCu layer. Furthermore, the investigation of samples prepared in templates with reduced porosity led to the discovery of IP GMR of 80% at 20 K, which may be a record value for multilayered nanowires deposited in PC templates. This strongly indicates that reduced amount of crossing zones have an impact on the GMR. However, due to several experimental challenges with the low nanowire packing density samples, the many attempts of reproducing the good results were unsuccessful. Interestingly, the samples with the lowest nanowire packing density showed that the contradicting results regarding the easy magnetisation directions, could possibly be attributed to the dipolar interactions between the nanowires in the network.

Furthermore, the AMR effect in the multilayers shows indications of being dominated by the amount of NiCoCu in the nanowire, and not significantly affected by the number of NiCoCu/Cu interfaces or the Cu concentration in the NiCoCu layer. The investigations in the framework of the Valet-Fert model of samples with fixed Cu layers and increased NiCoCu layer, indicated that the even the thinnest NiCoCu layers prepared in this work may be longer than the SDL. Finally, investigations of interconnected multilayered nanowire systems to decrease the IP saturation field, including multilayered nanowires of 105 nm in diameter and trilayer systems prepared in the 20% 40 nm templates have been carried out. However, the effect on the saturation fields were surprisingly low.

Chapter 4

Conclusions and perspectives

This Master's thesis has included extensive experimental studies on interconnected NiCoCu/Cu multilayered nanowire networks. The multilayers were synthesised by electrodeposition into novel track-etched PC templates with crossed pore networks, to create samples of interconnected nanowire networks. The main focus has been to investigate the CPP-GMR effect in such networks, and study how parameters such as electrolyte concentration, nanowire diameter, and nanowire packing density, influences the magnetotransport and magnetic properties of such networks.

Initially, synthesis parameters related to the electrolyte composition and electrodeposition potentials were found from earlier studies of NiCoCu/Co multilayered nanowire arrays [10]. Calibration of the remaining synthesis parameters were then performed, and the optimal parameters for pulse potentials, and the NiCoCu deposition time were obtained for the electrodeposition process. A series of samples was fabricated in templates of high porosity and 40 nm pore diameter, to identify the value of the Cu layer deposition time that resulted in the highest GMR ratio, which was 12%.

In the same templates the optimised synthesis parameters were used to investigate the effect of reduced Cu^{2+} electrolyte concentration. The concentration of 25 mM from the first sample series, were compared to similarly fabricated sample series from 15 and 5 mM concentrations. 15 mM Cu^{2+} concentration was concluded to yield the best compromise between deposition rate, deposition time, and Cu concentration in the NiCoCu alloy, and this concentration was used for all remaining samples. The GMR effect was higher in these samples. At room temperature an IP GMR ratio of 16.6%, and the value had increased with a factor of 2, to 33% when measured at 12 K. The evolution of the GMR with temperature showed that electron-magnon interactions occurred even av 12 K. The electrolyte containing only 5 mM was considered impractical due to the very long electrodeposition time associated with it.

To investigate the influence of the crossing zones on the GMR effect, series of samples were fabricated in low-porosity templates with pore packing densities reduced to a minimum. A sample prepared in the template with 8% porosity and pore diameters of 80 nm, turned out to exhibit 40% GMR at room temperature and 80% at 20 K. This may be a record value for GMR in PC templates. However several problems related to the synthesis and measurement design of these samples, lead to a profound investigation of every fabrication step to try and identify why the samples did not work. It was concluded that the the plasma etching process was the most probable cause of the problems. The samples having low nanowire packing density lead to reduced mechanical strength. The significant amount of heat generated in the samples during the plasma etching was assumed to lead to thermal expansion of the PC membrane, that could break the fragile nanowire networks. Another reason was identified by the appearance of weak localisation effect at low temperature transport measurements. This could be attributed to

remains of the Cu/Cr thin film after the plasma etching. The additional low-resistivity current channels these would contribute, explained why the GMR effect was apparent, but very low.

Although, the low-porosity templates proved unreliable, the one sample showing very high GMR effect stimulates to further research. It is no doubt that the reduction in crossing zones had a strong positive influence on the GMR. Investigation of the magnetotransport properties of a sample from the lowest porosity template lead to the an interesting discovery. This sample showed the expected relation between the saturation fields of the magnetotransport and magnetisation curves, and not the contradictory relation exhibited by the samples from higher porosity templates. The reason for this can probably be attributed to the dipolar interactions between the nanowires in the network, which is significantly reduced in the samples from low-porosity templates. Further investigation using ferromagnetic resonance spectroscopy is encouraged to identify the magnitude of the different contributions of dipolar interactions.

After the extensive troubleshooting of the fabrication process, it seemed very probable that the plasma etching method is causing the problems. Stepwise etching to reduce the heat development, or metallisation of thinner cathode layers on the templates to reduce the etching time, may be strategies worth investigating in the future.

In the more reliable high-porosity template with 40 nm pore diameter, sampler with increased NiCoCu layers were fabricated and studied within the framework of the Valet-Fert model. This investigation, combined with earlier reports on the NiCoCu/Cu multilayer system, lead to the indication that the layers in all the samples produced for this thesis were thicker than expected. This indeed explained why the easy magnetisation direction were in the OOP direction in all the samples, and not in the IP direction as expected. Even the samples with the thinnest NiCoCu layers might have layer thickness close to or larger than the SDL. If this observation is correct, it leads to at least two conclusions. The first is that higher GMR effect can be achieved if the NiCoCu layers can be reduced below the SDL. The second conclusion is that the PC template with small pore diameters may prevent electrodeposition of well-defined layers with small thickness. Maybe this could be improved in the future by treating the template with a wetting agent, but that is beyond the scope of this work.

Morphology measurements were unfortunately not successful for the multilayers due to the reduced mechanical strength of the nanowires full of interfaces. Thus, morphology and elemental composition studies were only carried out for continuous nanowire networks. The results showed that interconnected nanowire networks were created in all the different templates, but the low-porosity templates yielded networks which did not look self-supporting like the ones from high-porosity templates do. For magnetotransport measurements, or possible future applications, the networks should be kept in their low-porosity templates for support, to maintain the angles between them. Morphology measurements of the fragile multilayer networks would be very interesting, and should be addressed in the future. Especially TEM measurements should be prioritised in order to obtain the exact layer thicknesses. To get these would possibly clarify a lot and answer many unanswered questions that have appeared during this work. Moreover, the layer thicknesses would allow further interpretation of the results within the Valet-Fert model framework to determine the spin diffusion lengths l_{sf}^{F} and l_{sf}^{N}, and the spin asymmetry coefficients β and γ.

Elemental analysis revealed an alloy composition of the NiCoCu layer of approximately even amounts of Ni and Co, similar to what was expected. Based on recent studies of AMR in pure NiCo in equivalent templates, the composition helped in the interpretation of the AMR effect in the different samples. By comparing the AMR in samples with different Cu concentration in the

NiCoCu layers, it was discovered that this did not influence the AMR significantly. Later it was discovered from the AMR in the samples with different NiCoCu layer thicknesses and different number of interfaces, that the interfaces between the layers neither seemed to significantly influence the AMR. The AMR effect thus seemed to be dominated by the amount of NiCoCu in the nanowire.

Samples of continuous interconnected nanowire networks have been prepared for all the different electrolytes and in all templates, to compare with the multilayers. These samples were especially useful for the discussion about the AMR effect, studies of morphology and elemental composition, and interpretation of the magnetic properties through their magnetisation hysteresis curves. Moreover, they proved useful in the discussion around how domain wall propagation from the crossing zones affects the magnetisation reversal properties, and how it can influence the magnetic properties of the multilayered nanowire networks. Moreover, interconnected multilayered nanowire networks with with increased nanowire diameter, and interconnected trilayer samples, have been briefly investigated. It was expected that these systems would exhibit an easy direction of magnetisation with significantly reduced saturation field, due to the reduced IP demagnetising fields or reduced dipolar coupling between the trilayers, respectively. However this expectation was not met for neither system which did not show any significant improvement of performance. Lower saturation fields are prerequisites for spintronic applications, and this should be investigated further.

Furthermore, it could be interesting to investigate the GMR in samples with higher Ni concentration. This could be achieved by reducing the Co^{2+} concentration the the electrolyte, or by increasing the deposition potential. This would indeed alter the deposition rate too, and a calibration process similar to the one that was carried out in this work, would have been necessary.

As networks of interconnected magnetic nanowires is a novel system, there is not much theory developed yet to explain the experimental observations. Based on the results of this thesis and other related experimental studies with promising results, can hopefully inspire theoreticians to develop good models to compare with experimental data.

As a final remark, it has been shown that interconnected multilayered nanowire networks of the NiCoCu/Cu system is well suited for studying the CPP-GMR effect. The fabrication process as reported in this thesis, is reliable and ensures reproducible and stable samples for many of the templates, which are relatively easy to handle and measure. Samples with low nanowire packing density showed possibly record high GMR values, but were less reliable and lacked reproducibility. The good result, should however justify and encourage to further studies of these kind of samples.

Bibliography

[1] A. Fert and L. Piraux, "Magnetic nanowires," *Journal of Magnetism and Magnetic Materials*, vol. 200, no. 1, pp. 338–358, 1999.

[2] E. Araujo, A. Encinas, Y. Velázquez-Galván, J. M. Martínez-Huerta, G. Hamoir, E. Ferain, and L. Piraux, "Artificially modified magnetic anisotropy in interconnected nanowire networks," *Nanoscale*, vol. 7, no. 4, pp. 1485–1490, 2015.

[3] T. da Câmara Santa Clara Gomes, J. De La Torre Medina, Y. G. Velázquez-Galván, J. M. Martínez-Huerta, A. Encinas, and L. Piraux, "Interplay between the magnetic and magnetotransport properties of 3d interconnected nanowire networks," *Journal of Applied Physics*, vol. 120, no. 4, p. 043904, 2016.

[4] T. d. C. S. C. Gomes, J. D. L. T. Medina, M. Lemaitre, and L. Piraux, "Magnetic and magnetoresistive properties of 3d interconnected nico nanowire networks," *Nanoscale Research Letters*, vol. 11, no. 1, p. 466, 2016.

[5] M. N. Baibich, J. M. Broto, A. Fert, F. N. Van Dau, F. Petroff, P. Etienne, G. Creuzet, A. Friederich, and J. Chazelas, "Giant magnetoresistance of (001) fe/(001) cr magnetic superlattices," *Physical review letters*, vol. 61, no. 21, p. 2472, 1988.

[6] G. Binasch, P. Grünberg, F. Saurenbach, and W. Zinn, "Enhanced magnetoresistance in layered magnetic structures with antiferromagnetic interlayer exchange," *Physical review B*, vol. 39, no. 7, p. 4828, 1989.

[7] D. A. Thompson and J. S. Best, "The future of magnetic data storage techology," *IBM Journal of Research and Development*, vol. 44, no. 3, pp. 311–322, 2000.

[8] W. Pratt Jr, S.-F. Lee, J. Slaughter, R. Loloee, P. Schroeder, and J. Bass, "Perpendicular giant magnetoresistances of ag/co multilayers," *Physical Review Letters*, vol. 66, no. 23, p. 3060, 1991.

[9] L. Piraux, J. George, J. Despres, C. Leroy, E. Ferain, R. Legras, K. Ounadjela, and A. Fert, "Giant magnetoresistance in magnetic multilayered nanowires," *Applied Physics Letters*, vol. 65, no. 19, pp. 2484–2486, 1994.

[10] X.-T. Tang, G.-C. Wang, and M. Shima, "Layer thickness dependence of cpp giant magnetoresistance in individual co ni/ cu multilayer nanowires grown by electrodeposition," *Physical Review B*, vol. 75, no. 13, p. 134404, 2007.

[11] J. M. Coey, *Magnetism and magnetic materials*. Cambridge University Press, 2010.

[12] W. F. Brown Jr, "Single-domain particles: new uses of old theorems," *American Journal of Physics*, vol. 28, no. 6, pp. 542–551, 1960.

[13] H. Zijlstra, *Experimental methods in magnetism*, vol. 2. North-Holland Amsterdam, 1967.

[14] M. Vázquez, *Magnetic nano-and microwires: design, synthesis, properties and applications*. Woodhead Publishing, 2015.

[15] L. Vila, M. Darques, A. Encinas, U. Ebels, J.-M. George, G. Faini, A. Thiaville, and L. Piraux, "Magnetic vortices in nanowires with transverse easy axis," *Physical Review B*, vol. 79, no. 17, p. 172410, 2009.

[16] K. Pirota, F. Béron, D. Zanchet, T. Rocha, D. Navas, J. Torrejón, M. Vazquez, and M. Knobel, "Magnetic and structural properties of fcc/hcp bi-crystalline multilayer co nanowire arrays prepared by controlled electroplating," *Journal of Applied Physics*, vol. 109, no. 8, p. 083919, 2011.

[17] J. D. L. T. Medina, M. Darques, T. Blon, L. Piraux, and A. Encinas, "Effects of layering on the magnetostatic interactions in microstructures of co x cu 1- x/ cu nanowires," *Physical Review B*, vol. 77, no. 1, p. 014417, 2008.

[18] Y. Shimada, E. Sugawara, and H. Fujimori, "Initial permeability of composite-anisotropy multilayer films," *Journal of applied physics*, vol. 76, no. 4, pp. 2395–2398, 1994.

[19] L. Landau and E. Lifshitz, "On the theory of the dispersion of magnetic permeability in ferromagnetic bodies," *Phys. Z. Sowjetunion*, vol. 8, no. 153, pp. 101–114, 1935.

[20] W. Schwarzacher, K. Attenborough, A. Michel, G. Nabiyouni, and J. Meier, "Electrodeposited nanostructures," *Journal of magnetism and magnetic materials*, vol. 165, no. 1-3, pp. 23–29, 1997.

[21] A. Encinas-Oropesa, M. Demand, L. Piraux, I. Huynen, and U. Ebels, "Dipolar interactions in arrays of nickel nanowires studied by ferromagnetic resonance," *Physical Review B*, vol. 63, no. 10, p. 104415, 2001.

[22] T. Valet and A. Fert, "Theory of the perpendicular magnetoresistance in magnetic multilayers," *Physical Review B*, vol. 48, no. 10, p. 7099, 1993.

[23] P. Hofmann, *Solid state physics: an introduction*. John Wiley & Sons, 2015.

[24] N. F. Mott, "The electrical conductivity of transition metals," in *Proceedings of the Royal Society of London A: Mathematical, Physical and Engineering Sciences*, vol. 153, pp. 699–717, The Royal Society, 1936.

[25] Y. Yafet, "Conduction-electron spin relaxation by transition-element impurities in copper," *Journal of Applied Physics*, vol. 39, no. 2, pp. 853–854, 1968.

[26] T. McGuire and R. Potter, "Anisotropic magnetoresistance in ferromagnetic 3d alloys," *IEEE Transactions on Magnetics*, vol. 11, no. 4, pp. 1018–1038, 1975.

[27] H. Van Elst, "The anisotropy in the magneto-resistance of some nickel alloys," *Physica*, vol. 25, no. 1-6, pp. 708–720, 1959.

[28] S. S. Parkin, "Systematic variation of the strength and oscillation period of indirect magnetic exchange coupling through the 3d, 4d, and 5d transition metals," *Physical Review Letters*, vol. 67, no. 25, p. 3598, 1991.

[29] M. Johnson and R. Silsbee, "Thermodynamic analysis of interfacial transport and of the thermomagnetoelectric system," *Physical Review B*, vol. 35, no. 10, p. 4959, 1987.

[30] M. Johnson and R. Silsbee, "Ferromagnet-nonferromagnet interface resistance," *Physical review letters*, vol. 60, no. 4, p. 377, 1988.

[31] P. Van Son, H. Van Kempen, and P. Wyder, "Boundary resistance of the ferromagnetic-nonferromagnetic metal interface," *Physical Review Letters*, vol. 58, no. 21, p. 2271, 1987.

[32] M. Johnson, "Analysis of anomalous multilayer magnetoresistance within the thermomagnetoelectric system," *Physical Review Letters*, vol. 67, p. 3594, 1991.

[33] P. Drude, "Zur elektronentheorie der metalle," *Annalen der Physik*, vol. 306, no. 3, pp. 566–613, 1900.

[34] S. Zhang and P. M. Levy, "Conductivity perpendicular to the plane of multilayered structures," *Journal of Applied Physics*, vol. 69, no. 8, pp. 4786–4788, 1991.

[35] L. Piraux, S. Dubois, C. Marchal, J. Beuken, L. Filipozzi, J. Despres, K. Ounadjela, and A. Fert, "Perpendicular magnetoresistance in co/cu multilayered nanowires," *Journal of magnetism and magnetic materials*, vol. 156, no. 1-3, pp. 317–320, 1996.

[36] L. Piraux, S. Dubois, and A. Fert, "Perpendicular giant magnetoresistance in magnetic multilayered nanowires," *Journal of magnetism and magnetic materials*, vol. 159, no. 3, pp. L287–L292, 1996.

[37] G. A. Ozin, "Nanochemistry: synthesis in diminishing dimensions," *Advanced materials*, vol. 4, no. 10, pp. 612–649, 1992.

[38] C. R. Martin, "Membrane-based synthesis of nanomaterials," *Chemistry of Materials*, vol. 8, no. 8, pp. 1739–1746, 1996.

[39] F. Nasirpouri, "New developments in electrodeposition and pitting research," *India: Research Signpost Publication*, pp. 55–92, 2007.

[40] E. Ferain and R. Legras, "Track-etch templates designed for micro-and nanofabrication," *Nuclear Instruments and Methods in Physics Research Section B: Beam Interactions with Materials and Atoms*, vol. 208, pp. 115–122, 2003.

[41] A. Vlad, V.-A. Antohe, J. M. Martinez-Huerta, E. Ferain, J.-F. Gohy, and L. Piraux, "Three-dimensional interconnected ni core–nio shell nanowire networks for lithium microbattery architectures," *Journal of Materials Chemistry A*, vol. 4, no. 5, pp. 1603–1607, 2016.

[42] M. Paunovic and M. Schlesinger, *Fundamentals of electrochemical deposition*, vol. 45. john wiley & sons, 2006.

[43] L. Piraux, S. Dubois, J. Duvail, K. Ounadjela, and A. Fert, "Arrays of nanowires of magnetic metals and multilayers: Perpendicular gmr and magnetic properties," *Journal of Magnetism and Magnetic Materials*, vol. 175, no. 1-2, pp. 127–136, 1997.

[44] A. Blondel, J. P. Meier, B. Doudin, and J.-P. Ansermet, "Giant magnetoresistance of nanowires of multilayers," *Applied Physics Letters*, vol. 65, no. 23, pp. 3019–3021, 1994.

[45] K. Liu, K. Nagodawithana, P. Searson, and C. Chien, "Perpendicular giant magnetoresistance of multilayered co/cu nanowires," *Physical Review B*, vol. 51, no. 11, p. 7381, 1995.

[46] P. Evans, G. Yi, and W. Schwarzacher, "Current perpendicular to plane giant magnetoresistance of multilayered nanowires electrodeposited in anodic aluminum oxide membranes," *Applied Physics Letters*, vol. 76, no. 4, pp. 481–483, 2000.

[47] K. Attenborough, R. Hart, W. Schwarzacher, J.-P. Ansermet, A. Blondel, B. Doudin, and J. Meier, "Superlattice nanowires," in *MRS Proceedings*, vol. 384, p. 3, Cambridge Univ Press, 1995.

[48] V. M. Prida, J. García, L. Iglesias, V. Vega, D. Görlitz, K. Nielsch, E. D. Barriga-Castro, R. Mendoza-Reséndez, A. Ponce, and C. Luna, "Electroplating and magnetostructural characterization of multisegmented co 54 ni 46/co 85 ni 15 nanowires from single electrochemical bath in anodic alumina templates," *Nanoscale research letters*, vol. 8, no. 1, p. 263, 2013.

[49] I. Lake Shore Cryotronics, "http://www.lakeshore.com/products/vibrating-sample-magnetometer/pmc-micromag-2900-series-agm/pages/overview.aspx," jun 2017.

[50] C. Graham, "High-sensitivity magnetization measurements," *Journal of Materials Science & Technology*, vol. 16, no. 2, pp. 97–101, 2000.

[51] C. Barone, F. Romeo, S. Pagano, C. Attanasio, G. Carapella, C. Cirillo, A. Galdi, G. Grimaldi, A. Guarino, A. Leo, *et al.*, "Nonequilibrium fluctuations as a distinctive feature of weak localization," *Scientific reports*, vol. 5, 2015.

Rue Archimède, 1 bte L6.11.01, 1348 Louvain-la-Neuve **www.uclouvain.be/epl**